CogSust

Cognitive Sustainability

Sept 2025 Vol. 4. No. 3

ISSN 2939 - 5240

Cognitive Sustainability

Cognitive Sustainability (CogSust) is a double-blind peer-reviewed scientific journal published by CogSust Ltd. (H1116 Budapest Putnok u 9.)

The person responsible for publishing: Mária Szalmáné Csete editor@cogsust.com

The person responsible for editing: Ádám Török info@cogsust.com

CogSust is an online quarterly journal, publication frequency: quarterly, by

March, June, September, December.

ISSN 2939-5240

The journal is indexed by:

Library of Hungarian Scientific Works

Repository of the Library of Hungarian Academy of Science

Google Scholar

Sherpa Romeo

RePEc (Research Papers in Economics)

Directory of Open Access Journals

Crossref

Semantic Scholar

ERIH PLUS

Index Copernicus International

Dimensions

Scilit

Lens

https://doi.org/10.55343/CogSust.20522

Mathematical model for evaluating the stress-strain state of transport structures made of prefabricated corrugated metal constructions depending on the modulus of elasticity of the foundation soil

Vitalii KOVALCHUK
https://orcid.org/0000-0003-4350-1756
Department «Railway Transport», Lviv Polytechnic National University
Lviv, Ukraine
vitalii.v.kovalchuk@lpnu.ua

Ihor KARNAKOV
https://orcid.org/0000-0002-8751-9934
Department «Bridges and Tunnels» National Transport University
Kyiv, Ukraine
i.karnakov@ntu.edu.ua

Artur ONYSHCHENKO
https://orcid.org/0000-0002-1040-4530
Department «Bridges and Tunnels» National Transport University
Kyiv, Ukraine
a.onyshchenko@ntu.edu.ua

Mykola SYSYN
https://orcid.org/0000-0001-6893-0018
Technische Universität Dresden
Dresden, Germany
mykola.sysyn@tu-dresden.de

Olena BAL
https://orcid.org/ 0000-0003-2188-4098
Department «Railway Transport», Lviv Polytechnic National University
Lviv, Ukraine
olena.m.bal@lpnu.ua

Serhii HREVTSOV
https://orcid.org/0000-0003-2925-4293
Department «Transport Technologies» Lviv Polytechnic National University
Lviv, Ukraine
serhii.v.hrevtsov@lpnu.ua

Mykola BABYAK
https://orcid.org/0000-0001-5125-9133
Department «Railway Transport», Lviv Polytechnic National University
Lviv, Ukraine
mykola.o.babiak@lpnu.ua

https://doi.org/10.55343/CogSust.20522

Abstract

Modern transport structures require effective and reliable solutions to ensure durability under various foundation conditions, which is especially relevant in the context of increasing loads and the need for adaptive infrastructure. This study aims to assess the influence of soil foundation stiffness on the stress–strain state of prefabricated corrugated metal structures of transport facilities, considering the principles of cognitive sustainability and supporting decision-making in design. To achieve this aim, a method was proposed for replacing the corrugated shell profile with a smooth orthotropic shell by recalculating the equivalent physical and mechanical parameters, and finite element modelling was performed using the Plaxis software package. The results showed that as the soil foundation's elastic modulus increases, the vertical deformations of the metal shell decrease, while axial forces and horizontal deformations increase but remain within safe limits; when the modulus exceeds 90 MPa, horizontal deformations stabilise. The results make it possible to develop adaptive engineering solutions and can be integrated into decision support systems to enhance resilience and optimise infrastructure systems at the scale of the entire transport network. The proposed numerical modelling of prefabricated corrugated metal transport structures aligns with modern principles of cognitive sustainability, which involve shifting from local assessment of individual elements to a systemic approach in infrastructure management.

Keywords

transport structure, prefabricated corrugated metal constructions, deformations, stress, modulus of elasticity of the foundation

1. Introduction

Prefabricated corrugated metal constructions are promising structures in transport infrastructure development. These constructions are used in the construction of new transport facilities on highways and railways, in the reinforcement of reinforced concrete pipes and small bridges with reduced strength characteristics, as well as in the restoration of the load-bearing capacity of damaged engineering structures (Kovalchuk et al., 2017). However, based on operational experience, it is known that such structures are prone to the development of various defects and damages, which necessitate further research into the risks associated with their construction (Mistewicz, 2019).

An analysis of previous studies (Kunecki and Korusiewicz, 2013) has shown that, during the initial period of operation, transport structures made of prefabricated corrugated metal constructions experienced deformation of their cross-sectional shape. These deformations were of a residual accumulation nature, posing the risk of the metal transitioning into a plastic state. Moreover, defects and damage to the metal elements of the structures lead to a decrease in the load-carrying and traffic capacities of roads. This calls for additional strengthening measures (Kovalchuk et al., 2016), such as double corrugation methods and additional stiffening ribs.

One of the main contributing factors is the influence of weak foundation soils on the stress-strain state of prefabricated corrugated metal structures, due to the reduction in their strength characteristics. However, this issue requires comprehensive research to identify the patterns of how the modulus of elasticity of the structure's foundation influences the stress-strain behaviour of the metal corrugated constructions.

At the same time, studies of this type have an important cognitive component, as they aim to create adaptive infrastructure capable of flexibly responding to changes in operating conditions and loads. The obtained numerical modelling results can be integrated into decision support systems, enabling system-level optimisation of the transport network and contributing to the enhancement of human-centred resilience of engineering structures throughout their entire life cycle.

Cognitive thinking in transportation is critically important because it enables systematic analysis of complex transport processes, supports optimal decision-making, and allows infrastructure to adapt to changing operating conditions. Cognitive approaches make it possible to anticipate potential risks, assess the consequences of various load scenarios, integrate data from sensors and monitoring systems, and enhance both safety and reliability of traffic operations (Fischer et al., 2025; Krizsik et al., 2025).

When designing transport structures made of prefabricated corrugated metal constructions with a cross-section greater than 6.0 meters, it is recommended to use the finite element modelling method (El-Sawy, 2003; Bayoglu Flener, 2009; Esmaeili et al., 2013; Maleska and Beben, 2019). The regulatory document VBN V.2.3-218-198 applies only to engineering calculations of such structures with diameters up to 6.0 meters. Furthermore, the research in (Wysokowski and Howis, 2011)

https://doi.org/10.55343/CogSust.20522

established that reliable calculations of the stress-strain state of transport structures made of prefabricated corrugated metal constructions can be obtained using the finite element analysis method.

Numerical analysis of prefabricated corrugated metal structures of transport facilities involves two specific approaches. The first is modelling the corrugated metal construction, and the second is modelling the compacted soil backfill (Bayoglu Flener, 2009; Kovalchuk et al., 2018). The soil backfill is typically modelled as an elastoplastic, nonlinearly deformable medium. Each plane of the elemental volume of the soil backfill is subjected to normal stress (σ) and shear stress (τ). For this purpose, the Mohr–Coulomb model is used (Luchko, 2013). This model includes the soil's physical and mechanical parameters: unit weight, deformation modulus, Poisson's ratio, cohesion coefficient, internal friction angle, and dilatancy angle. These parameters are considered input data and significantly impact the stress-strain state of the prefabricated corrugated metal structures of the transport facility.

In studies (Korusiewicz and Kunecki, 2011; Mak et al., 2009;), based on experimental research and theoretical assessment of the stress-strain state of structures made from corrugated metal constructions, it was established that these structures can withstand overloads up to 2.5 times their design capacity, reaching only 16% of the yield strength of the steel used in the metal construction (Maleska and Beben, 2018).

In a study (Beben, 2018), during experimental investigations of corrugated metal structures under seismic loads, the maximum stress reached 92.3% of the yield strength of the construction steel. Under dynamic loads caused by moving railway rolling stock (Nabochenko et al., 2019), the maximum vertical deflection of the metal structure's diameter was recorded at 1.63 mm during the passage of a freight train, and 1.11 mm during the passage of a passenger train.

Much of the research is also devoted to studying the impact of temperature variations on the stress-strain state of transport structures made of corrugated metal constructions (Gera and Kovalchuk, 2019; 2022). Uneven temperature distribution on the surface of corrugated structures leads to the development of thermal stress states. When corrugated metal constructions are used to repair defective reinforced concrete pipes, stress concentration occurs at the material boundaries in the reinforced concrete pipe–filler–metal structure. The differences in the physical and mechanical properties of the construction materials cause this.

Studies (Beben, 2009; 2012; Elshimi, 2011; Kovalchuk et al., 2016; Machelski, 2013; Pettersson and Sundquist, 2012) have established that the load-bearing capacity of transport structures made of prefabricated corrugated metal constructions depends on the degree of compaction of the soil backfill. Insufficient compaction leads to a decrease in the load-bearing capacity of the structures. Moreover, works (Babyak and Neduzha, 2022; Yagoda et al., 2024) note that the condition of the infrastructure affects the dynamic interaction between the track and rolling stock.

From the analysis of the scientific literature, it has been determined that most studies present results evaluating the stress-strain state of corrugated metal structures subjected to variable loads from vehicles and environmental temperature effects. A significant portion of the research is also devoted to assessing the influence of the physical and mechanical properties of soil backfill on the strength characteristics of the structures. However, the issue of evaluating the stress-strain state of corrugated metal constructions with consideration of the modulus of elasticity of the foundation soil remains unresolved.

This study aims to model the stress-strain state of transport structures made of prefabricated corrugated metal constructions, considering the foundation soil's modulus of elasticity. To achieve this aim, this study investigates the distribution of stresses and deformations in the compacted soil backfill of the transport structure composed of corrugated metal constructions. Then, the patterns of deformation and stress variation in the metal structures of the transport facility, depending on the modulus of elasticity of the foundation, are established.

2. Data and methods

The theory of orthotropic shells is applied to recalculate the equivalent thickness of the corrugated metal sheet used in the structure (El-Sawy, 2003). This theory involves determining the equivalent thickness of the shell, which corresponds to the thickness of the corrugation. As a result, it allows for the determination of the actual value of the transport structure's axial stiffness EI (beam stiffness). The diagram illustrating the substitution of the corrugated isotropic shell of the transport structure with a flat orthotropic shell is shown in Fig. 1.

https://doi.org/10.55343/CogSust.20522

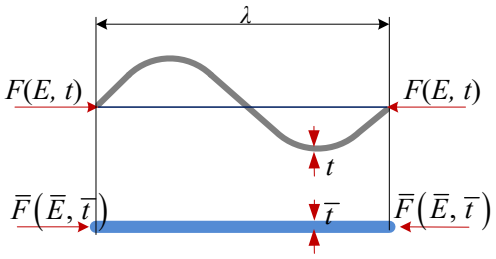

Figure 1. Diagram of replacing the corrugated metal profile of a transport structure with a smooth orthotropic shell (El-Sawy, 2003)

In Figure 1 and the formulas below, the following notations are used: E – Young's modulus; $\bar{E}$ – equivalent Young's modulus; t – thickness of the corrugated profile of the structure; $\bar{t}$ – equivalent thickness of the smooth profile; λ – length of the corrugation of the structural profile.

The formula for determining the equivalent thickness of the orthotropic shell of the transport structure is (1).

$$\bar{t} = \sqrt{12\frac{I}{A}}\,. \tag{1}$$

In this case, the equivalent Young's modulus of the steel used in the metal structure of the transport facility is calculated using (2).

$$\bar{E} = \frac{12I}{\bar{t}^3} \tag{2}$$

In formulas (1) and (2), the values I and A A represent the moment of inertia and the cross-sectional area per unit length of the corrugated shell of the transport structure, respectively.

Knowing the equivalent thickness and equivalent Young's modulus of the orthotropic shell, the axial moment of inertia of the cross-section of the smooth orthotropic shell can be determined using (3).

$$\bar{I} = \frac{\lambda\bar{t}^3}{12}\,. \tag{3}$$

In this case, the cross-sectional area of the orthotropic shell of the structural sheet is determined by (4)-

$$\bar{A} = \lambda\bar{t}\,, \tag{4}$$

Finally, the section modulus of the cross-section of the orthotropic shell of the structural sheet is determined using (5).

$$\bar{W} = \frac{\lambda\bar{t}^2}{6}\,. \tag{5}$$

These formulas calculate the equivalent geometric parameters of the orthotropic shell of corrugated metal structures in transport facilities. The presented approach can be adapted for other corrugation geometries or composite soil–structure systems with a layered foundation.

Since the methodology is based on the principle of replacing the corrugated shell with an equivalent smooth orthotropic shell by recalculating its physical and mechanical properties, changing the corrugation geometry would only require adjusting the design parameters (elastic moduli, moments of inertia, stiffness coefficients) according to the new shape.

In the case of a layered foundation, the approach can be extended by considering a multilayer soil model in the numerical simulation, where each layer is described by its own physical and mechanical parameters. This allows the stress–strain state of the structure to be assessed, accounting for the heterogeneity of the foundation and the interaction between layers, making the methodology applicable to a broader class of soil–structure systems.

The stress calculation in prefabricated corrugated metal constructions of transport structures is performed using the formula (6).

$$\sigma = \frac{N}{A} + \frac{M}{W} < f_{yd}\,, \tag{6}$$

https://doi.org/10.55343/CogSust.20522

where: N, M – axial force and bending moment, respectively; A, W – cross-sectional area and section modulus per unit length of the metal structure; f_{yd} – yield strength.

The stress-strain state of prefabricated corrugated metal constructions is determined using the finite element analysis software Plaxis. The research can be conducted in both two-dimensional and three-dimensional problem settings. In the case of a 2D problem setup (Luchko, 2013), the stress components σ_n, τ_n on an arbitrary plane are determined based on the stresses σ_x, σ_y, τ_{xz}. The formulas are as follows:

$$\begin{aligned} \sigma_n &= \sigma_x \cos^2\alpha + \sigma_z \sin^2\alpha + \tau_{xz} \sin 2\alpha; \\ \tau_n &= (\sigma_x - \sigma_z)\sin\alpha\cos\alpha - \tau_{xz}\,\mathrm{s}\cos 2\alpha. \end{aligned} \tag{7}$$

The principal stresses, maximum σ_1 and minimum σ_2, which are related to the conditions of equilibrium, are determined using the following formulas:

$$\sigma_{1,2} = \frac{\sigma_x + \sigma_z}{2} \pm \sqrt{\left(\frac{\sigma_x - \sigma_z}{2}\right)^2 + \tau^2_{xz}}\ . \tag{8}$$

In the case of perpendicularity of the two principal planes, formula (7) can be written in the following form:

$$\begin{aligned} \sigma_n &= \sigma_1 \cos^2\alpha_1 + \sigma_2 \sin^2\alpha_1; \\ \tau_n &= (\sigma_1 - \sigma_2)\sin\alpha_1\cos\alpha_1. \end{aligned} \tag{9}$$

The strength condition of the soil at a point, according to the Mohr-Coulomb law, is expressed by the following formula:

$$\frac{\sigma_1 - \sigma_2}{2} + \frac{\sigma_1 + \sigma_2}{2}\sin\varphi - c\cos\varphi = 0\ . \tag{10}$$

To investigate the influence of the modulus of elasticity of the foundation soils on the stress-strain state of corrugated metal constructions, a pipe with a diameter of 7.0 meters is considered. The geometric diagram of the pipe is shown in Fig. 2.

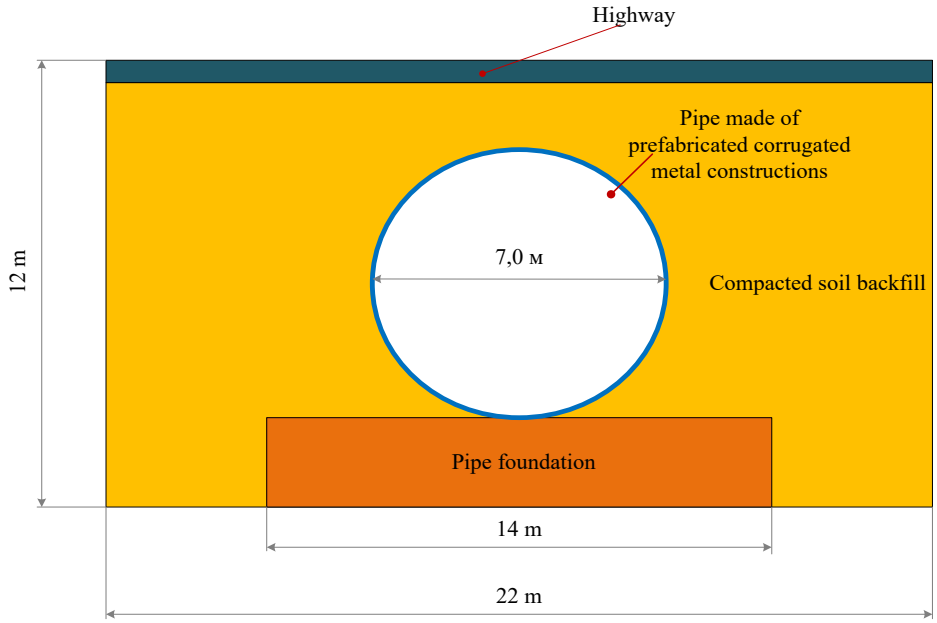

Figure 2.Geometric diagram of the pipe made of prefabricated corrugated metal constructions

A road passes above the pipe—the corrugated metal constructions of the pipe rest on a crushed stone foundation. Around the corrugated pipe, a compacted crushed stone-sand backfill is applied with the following soil properties: unit weight γ = 23.5 kN/m³; Poisson's ratio ν = 0.28; cohesion c = 10.2 kPa; internal friction angle φ = 34°; dilatancy angle ψ = 1.0°, and deformation modulus of the soil backfill E = 30 MPa.

To account for the influence of the physical and mechanical properties of the pipe's foundation soil on the stress-strain

https://doi.org/10.55343/CogSust.20522

state of the corrugated metal constructions, the deformation modulus of the crushed stone foundation soil was varied from $E = 30$ MPa to $E = 150$ MPa, with a calculation step of 10 MPa. The soil parameters of the pipe's metal structure foundation are presented in Table 1.

Table 1. Soil Parameters of the foundation for corrugated metal pipe structures

Physical and mechanical characteristics	Crushed stone materials
Unit weight of the foundation soil of the metal structure, γ, kN/m³	12.1
Poisson's ratio of the foundation soil, v	0.28
Cohesion of the foundation soil, c, kPa	0.03
Internal friction angle of the foundation soil, φ, °	41.9
Dilatancy angle, ψ, °	0
Variable value of the modulus of elasticity (deformation) of the pipe foundation soil, E, MPa	30–150

The load on the pipe made of prefabricated corrugated metal constructions is applied from a dump truck weighing 37 tons. In addition, the corrugated metal constructions of the pipe are subjected to additional loads from the pavement structure and their own self-weight.

The structure uses prefabricated corrugated metal constructions of the MultiPlate MP150×50 type. The corrugation wave parameters of the structure are shown in Fig. 3.

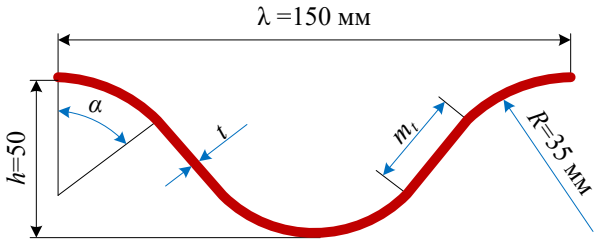

Figure 3. Geometric parameters of the corrugated profile of metal structures of the MultiPlate MP150×50 type

The main geometric parameters of the MultiPlate MP150×50 type structures, with a corrugation metal thickness of 7.0 mm, are presented in Table 2.

Table 2. Geometric parameters of the profile of MultiPlate MP150×50 type structures

t	A, mm²/mm	I, mm⁴/mm	W, mm³/mm	Z, mm³/mm
7	8,85	2801	98,3	141,9

The Young's modulus of the steel used in the corrugated metal structures of the facility is taken as $E = 2.1 \cdot 10^5$ MPa, and the Poisson's ratio is $v = 0.3$.

The stress-strain analysis of the pipe made of prefabricated corrugated metal constructions uses the Plaxis software. The computational model of the pipe with the applied load and boundary conditions is shown in Fig. 4.

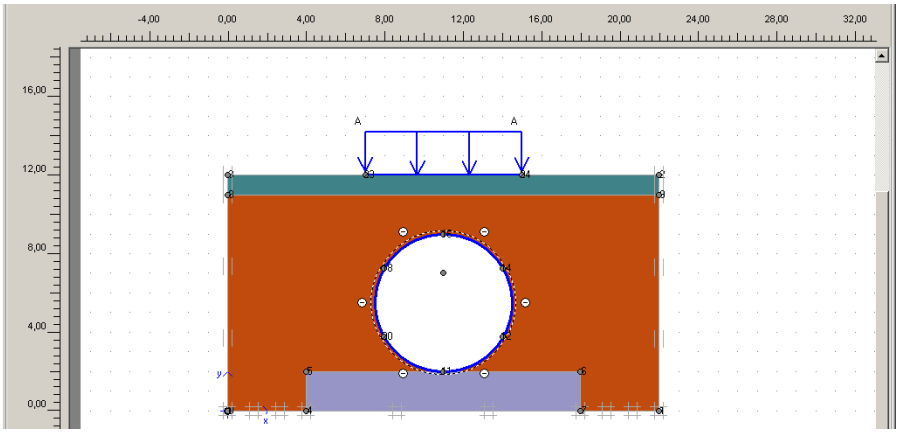

Figure 4. Computational model of the pipe

https://doi.org/10.55343/CogSust.20522

Vertical and horizontal displacements are restricted at the bottom of the pipe's soil envelope, while vertical displacements are allowed on the lateral sides. Fifteen-node finite elements are used to build the finite element model (Santos et al., 2020). The mesh size of the finite elements in the soil backfill and foundation is larger in the areas distant from the metal structures, compared to the mesh near the pipe's metal structures. The mesh is refined in the contact zones between the metal structures and the compacted soil backfill or foundation.

The stress and deformation analysis of the compacted soil backfill and pipe foundation is carried out in a nonlinear problem setting using the Mohr–Coulomb elastoplastic model.

3. Results and discussion

3.1. Results of the stress-strain analysis of the pipe's compacted soil backfill

The results of the calculation of vertical deformations in the compacted soil backfill for a foundation modulus of 150 MPa are shown in Fig. 5, while the horizontal deformations are presented in Fig. 6.

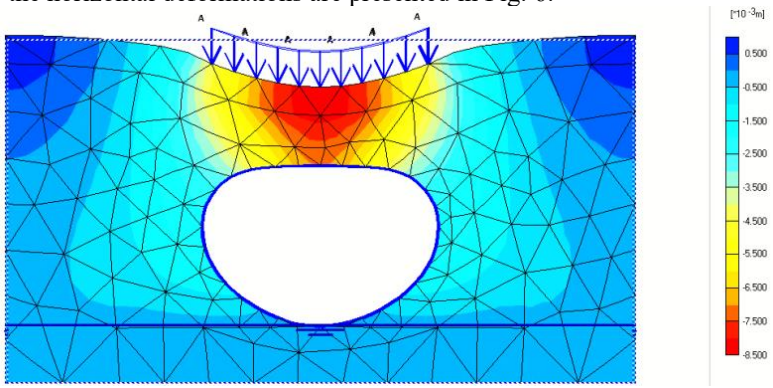

Figure 5. Vertical deformations of the compacted soil backfill of the pipe made of prefabricated corrugated metal constructions at a foundation modulus of 150 MPa

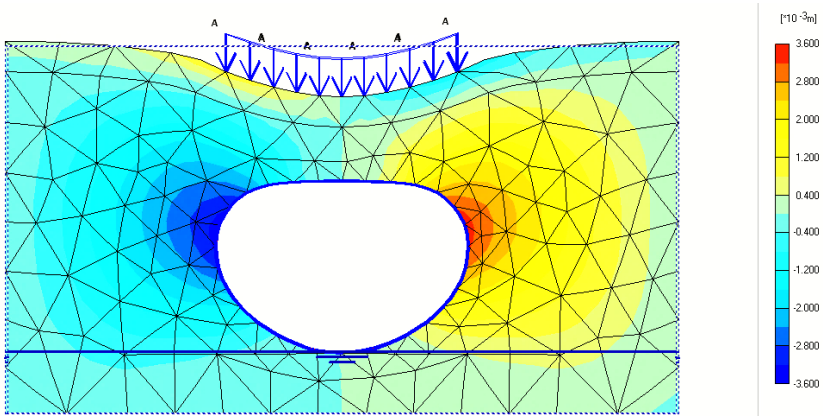

Figure 6. Horizontal deformations of the compacted soil backfill of the pipe made of prefabricated corrugated metal constructions at a foundation modulus of 150 MPa

The deformation calculation results showed that with a foundation modulus of 150 MPa for the pipe made of prefabricated corrugated metal constructions, the maximum vertical deformations reached 8.36 mm. At the same time, the horizontal deformations that occurred along the horizontal diameter of the pipe amounted to 3.41 mm.

The stress analysis results for the compacted soil backfill of the pipe made of corrugated metal constructions are shown in Fig. 7.

https://doi.org/10.55343/CogSust.20522

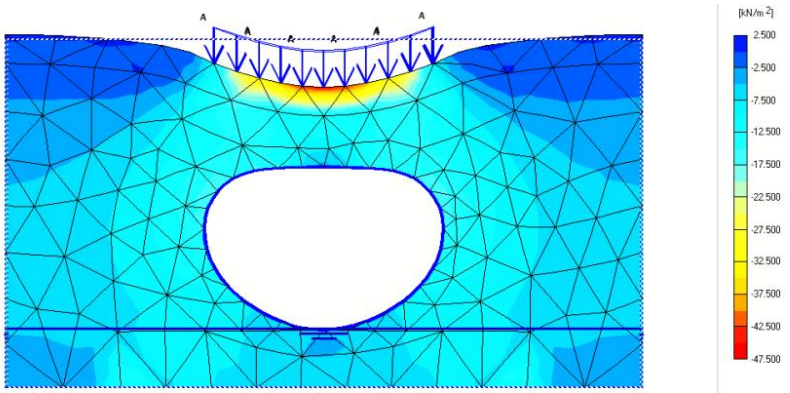

Figure 7. Stress distribution in the compacted soil backfill of the pipe made of corrugated metal constructions at a foundation soil modulus of 150 MPa

The maximum stresses occur at the crown of the pipe, with a magnitude of 46.07 kPa. At the same time, zones of plastic deformation accumulate in the pipe's arch and base areas of the soil backfill (Fig. 8).

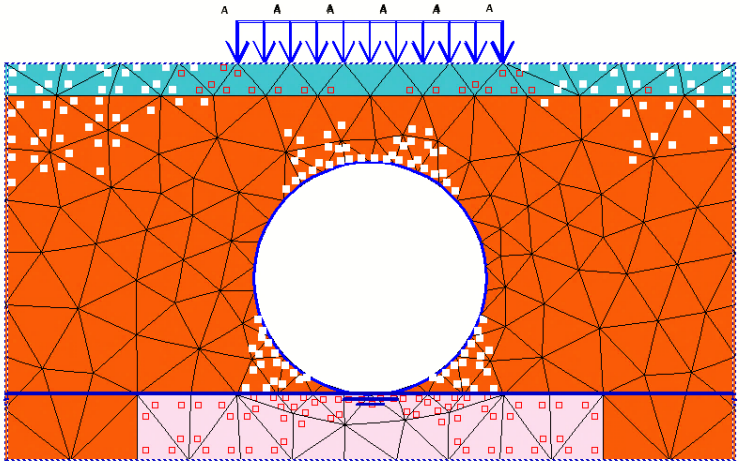

Figure 8. Distribution of plastic points in the compacted soil backfill of the pipe made of prefabricated corrugated metal constructions at a foundation soil modulus of 150 MPa

The results of multiple simulations of the stress-strain state of the pipe's compacted soil backfill, depending on the foundation soil modulus ranging from 30 MPa to 150 MPa with a calculation step of 10 MPa, are presented in Table 3.

Table 3. Stress-strain state of the compacted soil backfill depending on the modulus of elasticity of the foundation soil for the pipe made of prefabricated corrugated metal constructions

No.	Soil base modulus of elasticity, MPa	Maximum vertical deformations, mm	Maximum horizontal deformations, mm	Maximum stresses, kPa
1	30	8.87	3.35	46.62
2	40	8.72	3.37	46.45
3	50	8.63	3.38	46.41
4	60	8.57	3.38	46.31
5	70	8.52	3.39	46.32
6	80	8.48	3.39	46.29
7	90	8.46	3.39	46.27
8	100	8.43	3.4	46.12
9	110	8.41	3.4	46.12
10	120	8.39	3.4	46.08
11	130	8.38	3.4	46.13
12	140	8.37	3.4	46.09
13	150	8.36	3.4	46.07

Based on the stress-strain state analysis of the soil compaction backfill around the pipe made of prefabricated corrugated metal structures, it was determined that the maximum vertical deformations depend on the modulus of elasticity of the pipe's

https://doi.org/10.55343/CogSust.20522

foundation soil. With a soil modulus of elasticity of E = 30 MPa, the maximum vertical deformation is 8.87 mm, while at *E* = 150 MPa it is 8.36 mm. Accordingly, the maximum horizontal deformation is 3.35 mm and 3.4 mm, respectively. At the same time, the maximum stress in the soil compaction backfill reaches 46.62 kPa at *E* = 30 MPa, and 46.07 kPa at *E* = 150 MPa.

Significant vertical deformations of the soil backfill above the crown of the corrugated metal pipe structures are observed (Fig. 5).

As shown in Table 3, with an increase in the modulus of elasticity of the pipe's foundation soil, the magnitude of vertical deformations in the soil compaction backfill decreases, while horizontal deformations increase. When the soil deformation modulus reaches 90 MPa or more, horizontal deformations in the soil backfill stabilise. At the same time, an increase in the modulus of elasticity of the foundation leads to a reduction in stress levels within the soil backfill.

The distribution of vertical and horizontal deformations in the soil compaction backfill of the pipe and the stresses is nonlinear. The decrease in vertical deformations becomes less significant when the foundation modulus exceeds 90 MPa, compared to the change in stresses observed in the modulus range from 30 MPa to 90 MPa.

Therefore, the modulus of elasticity of the foundation significantly affects the stress-strain state of the soil compaction backfill around pipes made of prefabricated corrugated metal structures.

3.2. Assessment of the stress-strain state of corrugated metal pipe structures depending on the modulus of elasticity of the foundation soil

To assess the stress-strain state of the corrugated metal pipe structures, it is necessary to determine the values of axial longitudinal force and bending moment. For this purpose, the Plaxis software suite obtains the total deformations, axial force, and bending moment diagrams. The distribution diagrams of deformations, axial force, and bending moment for a foundation soil modulus of elasticity of 150 MPa are shown in Fig. 9.

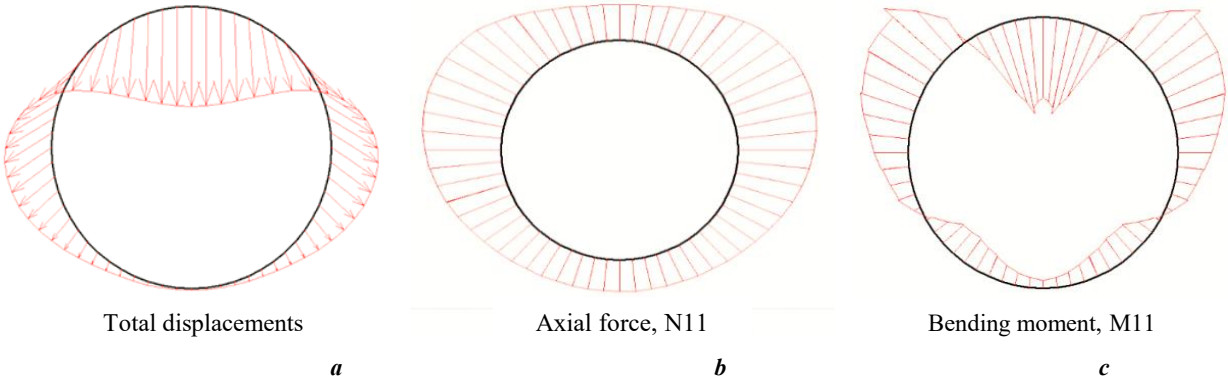

Figure 9. Diagrams for a foundation soil modulus of elasticity of 150 MPa:
a – total deformations of the corrugated metal shell of the pipe; b – axial force in the pipe walls; c – bending moment

From the diagram of vertical deformations of the metal pipe structures (Fig. 9a), it can be seen that the maximum deformations occur at the crown of the pipe and the minimum at the base. The maximum axial force arises on the lateral sides of the metal structures, at points offset by 35 degrees from the vertical diameter (Fig. 9b). These points also exhibit the maximum positive bending moment (the metal structures are under tension). However, at the pipe crown, the bending moment is negative, indicating that the metal structures are under compression (Fig. 9c).

From the graphical dependencies of vertical and horizontal deformations of the corrugated metal pipe structures (Figs. 10–11), it is evident that the distribution is nonlinear.

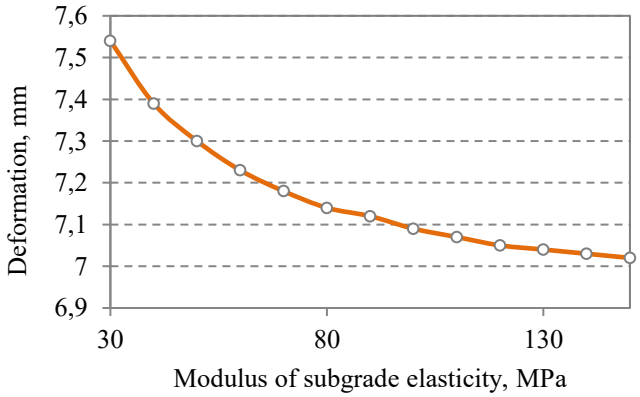

https://doi.org/10.55343/CogSust.20522

Figure 10. Vertical deformations of corrugated metal pipe structures

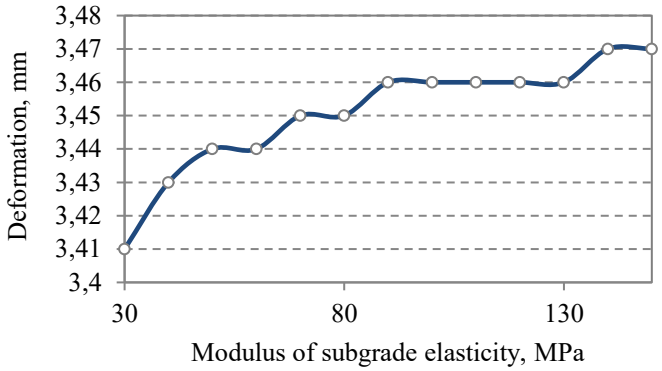

Figure 11. Horizontal deformations of corrugated metal pipe structures

The magnitude of vertical deformations of the metal pipe structures decreases with an increase in the modulus of elasticity of the pipe foundation soil, while the horizontal deformations of the metal pipe structures increase. However, the increase in horizontal deformations is marginal, and when the modulus of elasticity of the foundation soil exceeds 90 MPa, the deformations stabilise.

To determine the stresses in the prefabricated corrugated metal pipe structures, the results of the calculations of axial force and bending moment in the walls of the metal structures are presented.

The graphical dependencies of these forces are shown in Fig. 12 and Fig. 13, respectively.

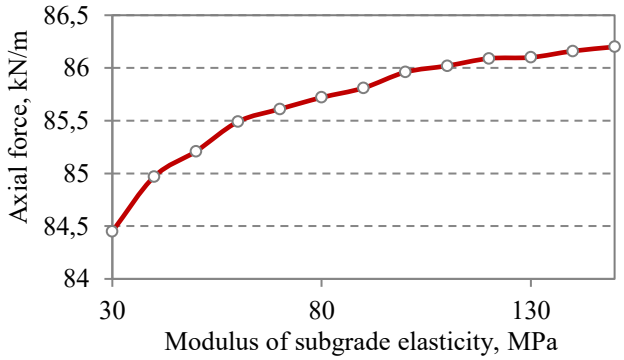

Figure 12. Dependence of axial forces in metal structures on the modulus of elasticity of the pipe foundation soil

The values of axial forces arising in the corrugated metal pipe structures increase with the growth of the modulus of elasticity of the pipe foundation soil.

The research results showed that with an increase in the modulus of elasticity of the pipe foundation soil, the vertical deformations of the metal structures decrease, while the axial forces in the metal pipe structures increase.

The maximum vertical deformation of the metal pipe structures is 7.54 mm at a foundation soil modulus of 30 MPa, and 7.02 mm at 150 MPa, while the corresponding axial force values are 84.45 kN/m and 86.20 kN/m, respectively.

A similar trend is observed in calculating bending moments in the metal pipe structures (Fig. 13).

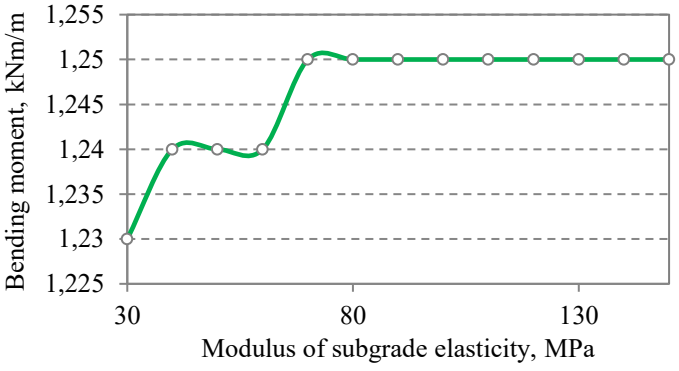

Figure 13. Dependence of bending moments in metal structures on the modulus of elasticity of the foundation soil

https://doi.org/10.55343/CogSust.20522

It should be noted that the magnitude of the bending moments does not have a significant impact on the stress-strain state of the corrugated metal pipe structures, as the bending moment values vary only from 1.23 to 1.25 kNm/m with changes in the modulus of elasticity of the pipe foundation soil from 30 MPa to 150 MPa.

The calculation results showed that the stress values in the prefabricated corrugated metal pipe structures are 9.55 MPa at a foundation soil modulus of 30 MPa, and 9.75 MPa at a foundation soil modulus of 150 MPa.

For all values of the foundation soil modulus, the strength of the corrugated metal pipe structures is ensured, as the stresses remain within safe limits and are significantly lower than the allowable limit of 235 MPa.

Based on the results of the comprehensive study, new relationships were obtained between the modulus of elasticity of the soil foundation and the vertical deformations, axial forces, and horizontal deformations of the metal shell. These relationships make it possible to predict the behaviour of the structures at the early design stages. It was found that when the modulus of elasticity of the soil foundation exceeds 90 MPa, the horizontal deformations of the structures become stabilised, which represents a new engineering criterion for optimising foundation parameters during the design of transport facilities with prefabricated corrugated metal structures.

The continuation of further scientific research will focus on accounting for dynamic loads from moving transport units. This will make it possible to determine the deformation patterns of metal structures under dynamic loading and assess additional axial forces and stresses in the metal structures, considering the modulus of elasticity of the foundation soils.

4. Conclusion

Based on the numerical calculations of the stress-strain state of prefabricated corrugated metal structures of transport facilities, the following conclusions were obtained:

1. The finite element method can assess the stress-strain state of prefabricated corrugated metal structures of large cross-section transport facilities by conducting multivariable studies. The proposed numerical modelling of prefabricated corrugated metal structures of transport facilities aligns with modern principles of cognitive sustainability, which involve a shift from local assessment of individual elements to a system-level approach in infrastructure management.

2. The distribution of vertical and horizontal deformations in the pipe's compacted soil backfill and the stress distribution is nonlinear. For a foundation soil modulus of 30 MPa, the maximum vertical deformation of the soil backfill was 8.87 mm, and for a modulus of 150 MPa, 8.36 mm. The horizontal deformations were 3.35 mm and 3.41 mm, respectively. The maximum stresses that occur at the crown of the pipe for a foundation soil modulus of 30 MPa amounted to 46.62 kPa, and for a modulus of 150 MPa, 46.07 kPa. At the same time, the decrease in vertical deformations with an increase in the modulus of elasticity of the foundation soil from 90 MPa and higher shows a smaller difference in stress values compared to the range of moduli from 30 MPa to 90 MPa.

3. With the increase of the modulus of elasticity of the pipe foundation soil, the vertical deformations of the metal structures decrease, while the axial forces and horizontal deformations of the metal structures increase. However, the increase in horizontal deformations is marginal, and when the modulus of elasticity of the foundation soil exceeds 90 MPa, the deformations stabilise.

4. The maximum vertical deformations of the metal pipe structures at a foundation soil modulus of 30 MPa are 7.54 mm, and at a modulus of 150 MPa, 7.02 mm. At the same time, the corresponding axial forces are 84.45 kN/m and 86.20 kN/m, respectively. As a result, the stresses in the corrugated metal pipe structures are 9.55 MPa and 9.75 MPa, respectively.

5. Based on the results of the comprehensive study, new relationships were obtained between the modulus of elasticity of the soil foundation and the vertical deformations, axial forces, and horizontal deformations of the metal shell. These relationships make it possible to predict the behaviour of the structures at the early design stages. It was found that when the modulus of elasticity of the soil foundation exceeds 90 MPa, the horizontal deformations of the structures become stabilised, which represents a new engineering criterion for optimising foundation parameters during the design of transport facilities with prefabricated corrugated metal structures.

The obtained results make it possible to predict the behaviour of prefabricated corrugated metal structures under varying foundation stiffness and can be integrated into decision support systems. This will contribute to the creation of adaptive infrastructure and enhance the resilience of transport facilities in accordance with the principles of cognitive sustainability.

Acknowledgement

The authors did not involve any sponsors in conducting this research.

References

Babyak, M., Neduzha, L. (2022). Transportation Optimisation of Homogeneous Freight in the Transport Systems. *Transport Means – Proceedings of the International Conference*, October 2022. 755–760. URL: https://www.researchgate.net/publication/366190920_Transportation_Optimization_of_Homogeneous_Freight_in_the_Transport_Systems

https://doi.org/10.55343/CogSust.20522

Bayoglu Flener, E. (2009). Response of long-span box type soil-steel composite structures during ultimate loading tests. *Journal of Bridge Engineering*. 14(6). DOI: 10.1061/(ASCE)BE.1943-5592.0000031

Beben, D. (2009). Numerical analysis of a soil-steel bridge structure. *The Baltic Journal of Road and Bridge Engineering*. (1), 13–21. DOI: 10.3846/1822-427X.2009.4.13-21

Beben, D. (2012). Numerical study of performance of soil-steel bridge during soil backfilling. *Structural Engineering and Mechanics*. 42(4), 571–587. DOI: 10.12989/sem.2012.42.4.571

Beben, D. (2018). Experimental testing of soil-steel railway bridge under normal train loads. In: Conte, J., Astroza, R., Benzoni, G., Feltrin, G., Loh, K., Moaveni, B. (eds): *Experimental Vibration Analysis for Civil Structures.* EVACES 2017. Lecture Notes in Civil Engineering. 5. Springer, Cham. 805–815. DOI: 10.1007/978-3-319-67443-8_71

El-Sawy, K. M. (2003). Three-dimensional modeling of soil-steel culverts under the effect of truckloads. *Thin-Walled Structures*.41(8), 747–768.

Elshimi, T. M. (2011). Three-dimensional nonlinear analysis of deep-corrugated steel culverts. *Queen's University* Publ, 738 p..

Esmaeili, M., Zakeri, Ali, Abdulrazagh, P. H. (2013). Minimum depth of soil cover above long-span soil-steel railway bridges. *International Journal of Advanced Structural Engineering*. 5, Art. 7. 1–7. DOI: 10.1186/2008-6695-5-7

Fischer, S., Kurhan, M., Kurhan, D. (2025). Innovative technologies and cognitive factors for enhancing safety of train and car movement at level crossings. In: Zöldy, M. (ed.): *Proceedings of the 3rd Cognitive Mobility Conference. COGMOB 2024*. Lecture Notes in Networks and Systems, 1258. Springer, Cham. DOI: 10.1007/978-3-031-81799-1_1

Gera, B., Kovalchuk, V. (2019). A study of the effects of climatic temperature changes on the corrugated structure of a culvert of a transportation facility. *Eastern-European Journal of Enterprise Technologies*. 3(7) (99), 26–35. DOI: 10.15587/1729-4061.2019.168260

Gera, B., Kovalchuk, V., Dmytruk V. (2022). Temperature field of metal structures of transport facilities with a thin protective coating. *Mathematical Modelling and Computing*. 9(4), 950–958. DOI: 10.23939/mmc2022.04.950

Korusiewicz, L., Kunecki, B., (2011). Behaviour of the steel box-type culvert during backfilling. *Archives of Civil and Mechanical Engineering*. 11(3), 638–650. DOI: 10.1016/S1644-9665(12)60106-X

Kovalchuk, V., Luchko, J., Bondarenko, I., Markul, R., Parneta, B. (2016). Research and analysis of the stressed-strained state of metal corrugated structures of railroad tracks. *Eastern-European Journal of Enterprise Technologies*. 6(7) (84), 4–10. DOI: 10.15587/1729-4061.2016.84236

Kovalchuk, V., Markul, R., Pentsak, A., Parneta, B., Gajda, O., Braichenko, S. (2017). Study of the stress-strain state in defective railway reinforced-concrete pipes restored with corrugated metal structures. *Eastern-European Journal of Enterprise Technologies*. 5(1) (89), 37–44. DOI: 10.15587/1729-4061.2017.109611

Kovalchuk, V., Kovalchuk, Y., Sysyn, M., Stankevych, V., Petrenko, O. (2018). Estimation of carrying capacity of metallic corrugated structures of the type multiplate MP 150 during interaction with backfill soil. *Eastern-European Journal of Enterprise Technologies.* 1(1) (91), 18–26. DOI: 10.15587/1729-4061.2018.123002

Krizsik, N., Sipos, T. (2025). The Role of Cognitive Skills in Human–Vehicle Interactions at Designated Pedestrian Crossings. In: Zöldy, M. (ed.): *Proceedings of the 3rd Cognitive Mobility Conference. COGMOB 2024.* Lecture Notes in Networks and Systems, 1258. Springer, Cham. DOI: 10.1007/978-3-031-81799-1_10

Kunecki, B., Korusiewicz, L. (2013). Field tests of large-span metal arch culvert during backfilling. *Roads and Bridges – Drogi i Mosty*. 12(3), 283–295. DOI: 10.7409/rabdim.013.020

Luchko, Y. Y. (2013) – Лучко Й. Й. (2013). Ґрунтознавство, механіка ґрунтів, основи та фундаменти [Soil Science, Soil Mechanics, Foundations and Substructures]. Каменяр, Львів.

Machelski, C. (2013). Shear forces in the connection of structural elements under bending. *Studia Geotechnica et Mechanica*. 35(3), 69–83. DOI: 10.2478/sgem-2013-0031.

Mak, A. C., Brachman, R. W. I., Moore, I. D. (2009). Measured response of a deeply corrugated box culvert to three dimensional surface loads. *Transportation Research Board Annual Conference*, Washington D. C., Paper No. 09-3016. 14 p.

Maleska, T., Beben, D. (2018). Behaviour of corrugated steel plate bridge with high soil cover under seismic excitation. *MATEC Web of Conferences*. 174, 04003,–11. DOI: 10.1051/matecconf/201817404003.

Maleska, T., Beben, D. (2019). Numerical analysis of a soil-steel bridge during backfilling using various shell models. *Engineering Structures*. 196(3), 1–12. DOI: 10.1016/j.engstruct.2019.109358

Mistewicz, M. (2019). Risk assessment of the use of corrugated metal sheets for construction of road soil-shell structures. *Roads and Bridges – Drogi i Mosty*. 18(2), 89–107. DOI: 10.7409/rabdim.019.006

Nabochenko, O., Sysyn, M., Kovalchuk, V., Kovalchuk, Yu., Pentsak, A., Braichenko, S. (2019). Studying the railroad track geometry deterioration as a result of an uneven subsidence of the ballast layer. *Eastern-European Journal of Enterprise Technologies*. 1(7) (97), 50–59. DOI: 10.15587/1729-4061.2019.154864

Pettersson, L., & Sundquist, H. (2014). Design of soil steel composite bridges. KTH Royal Institute of Technology. URL: http:// www.diva-portal.org/smash/get/diva2:761594/fulltext01.pdf

Santos, R. R. V., Kang, J., Park, J-S. (2020). Effects of embedded trench installations using expanded polystyrene geofoam applied to buried corrugated steel arch structures. *Tunnelling and Underground Space Technology*. 98(4), 103323. DOI: 10.1016/j.tust.2020.103323

Wysokowski, A., Howis J. (2011). Obliczenia przepustów Metodą Elementów Skończonych [Culvert Calculations Using the Finite Element Method]. *MES*. 3(36), 54–57.

https://doi.org/10.55343/CogSust.20522

Yagoda, D., Babyak, M., Keršys, R., Neduzha, L. (2024). Research on the Resource in the Wheel-Rail Pair during the Life Cycle of Traction Rolling Stock. *Transport Means – Proceedings of the International Conference*. 821–825. DOI: 10.5755/e01.2351-7034.2024.P821-825

DOI: 10.55343/CogSust.20523

The analytic hierarchy process as a cognitive tool for evaluating switch components

Mykola KURHAN
https://orcid.org/0000-0002-8182-7709
Department Transport Infrastructure, Ukrainian State University of Science and Technologies
Dnipro, Ukraine
m.b.kurhan@ust.edu.ua

Dmytro KURHAN
https://orcid.org/0000-0002-9448-5269
Department Transport Infrastructure, Ukrainian State University of Science and Technologies
Dnipro, Ukraine
d.m.kurhan@ust.edu.ua

Serhii BAIDAK
https://orcid.org/0000-0002-7909-8527
Department Transport Infrastructure, Ukrainian State University of Science and Technologies
Dnipro, Ukraine
s.y.baidak@ust.edu.ua

Vladyslav KHMELEVSKYI
https://orcid.org/0009-0000-3221-6955
Department Transport Infrastructure, Ukrainian State University of Science and Technologies
Dnipro, Ukraine
Junkpff@gmail.com

Abstract

The purpose of this study is to improve the approach to the comprehensive evaluation of switch elements by applying the Analytic Hierarchy Process (AHP). This method makes it possible to determine their priority according to safety and efficiency criteria, as well as to justify optimal strategies for modernization and reconstruction under conditions of increasing train speeds. The scientific approach involves the use of AHP with consideration of the specific operational features of switches on high-speed railways. In particular, the study accounts for higher safety and speed requirements, decreasing maintenance costs, and the reduced service life of structural components. A hierarchy of criteria was developed, along with pairwise comparisons, the calculation of weighting coefficients, and an integrated assessment of alternatives. The application of AHP enabled the determination of the priority of each switch type based on the criteria of traffic safety, speed, operational costs, and service life. According to the analysis, the priorities of the main switch elements were established as follows: frog – 0.395; closure curve – 0.234; switch blade – 0.190; switch curve – 0.181. These results confirm that the frog is the most critical element in terms of its overall impact on safety, speed, and maintenance costs, which is primarily due to its structural complexity and high wear rate (especially under dynamic loads). The findings provide a basis for informed decision-making regarding the prioritization of repair or replacement of individual structural elements, considering the operating conditions of high-speed lines.

Keywords
railway switch, traffic safety, service life, Analytic Hierarchy Process (AHP), cognitive processes

DOI: 10.55343/CogSust.20523

1. Introduction

Transport is one of the strategic sectors of the economy, and railway transport plays a key role within it. The modern development of railways is inseparably linked with innovative technologies. However, in addition to technological solutions, there is a growing recognition of the importance of the human factor in ensuring safety and efficiency (Endsley, 1995; Reason, 1990). This is particularly relevant to railway switches, which are among the most critical and complex elements of railway infrastructure.

The problem and relevance of this research arise from the premise that switches are not merely technical objects; they demand a high degree of perceptual accuracy and decision-making from personnel (train drivers, dispatchers, maintenance crews). The human eye and brain must rapidly process visual signals, engineering elements, and information from control systems. The extent to which the design of a switch is intuitive and "cognitively compatible" determines the speed of reaction, the minimization of errors, and, consequently, traffic safety.

In this context, traditional approaches to the evaluation of switch elements, which focus exclusively on engineering criteria (strength, wear resistance), are insufficient. It is essential to consider how design features influence the cognitive processes of operators, which ultimately affect the overall safety of train operations.

The aim of this study is to improve the approach to the comprehensive evaluation of switch elements by integrating cognitive analysis. The Analytic Hierarchy Process (AHP) (Taha, 2017) is applied, which makes it possible to determine the priority of switch elements not only according to classical technical and economic criteria (traffic safety, speed, operational costs, service life), but also with consideration of cognitive complexity and the human factor (Zöldy et al., 2024).

2. Data and methods

Considering the railway switch as a system consisting of the switch blades, switch curve, frog, and closure curve (Table 1), the authors evaluated each element on a scale from 1 to 10. Particular attention is given to how design features influence personnel perception and decision-making. It is essential that the chosen solutions comply not only with general standards but also consider the unique operating conditions and the human factor on railways. Thus, the results of this study contribute to the development of a more "intelligent" and safer railway infrastructure.

Table 1. Key parameters and characteristics influencing the choice of switch types

Characteristic	Purpose / Application features
Frog number	– For conventional railways (speed up to 120–140 km/h), frog numbers from 1/9 to 1/14 are used, sometimes 1/18. – For high-speed railways (160 km/h and above), larger frog numbers are applied: 1/18, 1/26, 1/30, 1/38, etc. The higher the frog number (i.e., the smaller the crossing angle), the larger the radius of the diverging curve, which allows higher speeds.
Switch blade design	– Flexible blades: applied on high-speed lines; ensure smoother entry of wheelsets into the diverging track. – Conventional blades: used on general-purpose lines.
Frog type	– With cast manganese insert: a traditional solution used on conventional-speed lines. – With movable-point frog (swingnose crossing): mandatory for high-speed switches; provides continuity of the running surface, reduces impact loads and wear.
Rail type	UIC 60 (or others in the case of mixed or transition sections). The choice depends on integration with the existing track.
Fastening method	Preference is given to fastening on prestressed concrete sleepers, which provide increased stability and durability of the structure.
Manufacturer	– Vossloh Cogifer (France, Germany). – voestalpine Railway Systems (Austria). – Weichenwerk Wörth (Germany). – Dnipro Switch Plant (Ukraine).

Design features of railway switches. Railway switches are key elements of railway infrastructure that provide train routing and direction changes. The main types of switches (cast, movable-point frogs, and crossings with different numbers – 1/9, 1/11, 1/18, etc.) are described in detail in Wang et al. (2024) and Boghani et al. (2021). The authors emphasize that the choice of design largely determines traffic safety, permissible speed, and maintenance costs. For example, Wang et al. (2024) proposes a comprehensive approach to the evaluation and maintenance of switches, incorporating data on wear, speed, loads, and geometric characteristics. Critical components of the design are identified using analytical modelling and monitoring systems. This study is valuable as an example of a multi-criteria analysis compatible with AHP methods. In Boghani et al. (2021), a multi-criteria analysis of switch types is presented, considering speed, comfort, cost, and reliability. The authors apply AHP and sensitivity analysis, presenting it as a practical decision-support tool for switch modernization.

Evaluation criteria for switch elements. Studies (Krmac and Djordjević, 2017; Nyström and Söderholm, 2008) examine the key criteria for evaluating switches: traffic safety, permissible speed, durability of elements, and operational costs. It is noted that in the design and modernization of switches it is necessary to consider not only technical characteristics but also the economic feasibility of using a particular type of switch, depending on the function of the track (mainline, station, etc.).

Methods of modelling and selecting optimal designs. Publications (Polishchuk, 2021; Barkhordari et al., 2019) discuss modern methods of analysis for selecting the optimal switch design. In particular, the application of the Analytic Hierarchy Process (AHP) makes it possible to systematize expert assessment and account for a set of interrelated factors. The studies demonstrate that the use of AHP in combination with pairwise comparison of criteria provides well-grounded decisions at the stage of switch design or replacement.

Experience of different railways. Research (Barkhordari et al., 2021; Saaty and Kułakowski, 2016) analyses the experience of German, Polish, Czech, Hungarian, Ukrainian and other railways in operating switches on high-speed lines. It

DOI: 10.55343/CogSust.20523

is noted that modern switches must be adapted to dynamic loads at speeds above 160 km/h, which places new demands on the design of frogs, switch blades, and control mechanisms.

Regulatory framework and recommendations. Regulatory documents establish requirements for the geometry, materials, laying, and maintenance of switches. Scientific works (Fischer, 2025; Fischer et al., 2025b) provide a comparative analysis of the requirements for elements in accordance with European and national standards, enabling conclusions on the harmonization of regulations.

In Kovalchuk et al. (2018), a comprehensive method for extending the service life of switch frogs is presented, based on consideration of the longitudinal profile of the frog, the magnitude of dynamic forces, and normal stresses.

There are various methods for assessing the reliability of railway track components (e.g. Fischer, 2022; 2023), including the Analytic Hierarchy Process (AHP) (Fischer et al., 2025a). For the AHP, it is necessary to create comparison matrices for each criterion, and then among the criteria themselves. The Saaty scale (Saaty and Shang, 2007; Saaty and Tran, 2007) is used for pairwise comparisons, where: 1 – equal importance, 3 – moderate preference, 5 – strong preference, 7 – very strong preference, 9 – extreme preference; 2, 4, 6, 8 – intermediate values. Reciprocal values (1/3, 1/5, etc.) are applied accordingly. For example, if *A* is three times more important than *B*, then *B* is 1/3 as important as *A*.

3. Results and discussion

After conducting expert analysis, the following justification of the evaluations was obtained.

Switch points (Fig. 1)

- Traffic safety (10): This is the most critical element, where the actual transfer of a train from one track to another takes place. Any defect, wear, improper contact of the switch blade, or malfunction of the actuator may lead to derailment. It is the most vulnerable part of the switch.
- Operating speed (9): The quality of blade-to-stock rail contact and the geometry of the switch points directly affect the smoothness and permissible speed of train passage, especially on the diverging route. Modern flexible switch points allow higher speeds.
- Maintenance costs (9): Switch points are subject to significant dynamic impact and wear. Maintenance costs (adjustment, repair, replacement) are among the highest.
- Service life (8): Due to intensive wear and dynamic loads, the service life of switch points is generally shorter than that of sleepers or the main rail sections.

Figure 1. Switch points of a R65 turnout with a 1/11 crossing, track gauge 1 435 mm (Ukraine)

Switch curve

- Traffic safety (8): The correct radius and absence of defects in the switch curve are important for safe train passage. However, it is not as “active” a switching element as the switch points or the frog.
- Operating speed (10): The radius of the switch curve is the decisive factor for the permissible speed on the diverging route. The gentler the curve (larger radius), the higher the achievable speed.

DOI: 10.55343/CogSust.20523

- Maintenance costs (7): Costs are mainly associated with rail and sleeper wear along the curve, but they are generally lower than for switch points or the frog.
- Service life (7): Rails in the curve are prone to lateral wear, which may somewhat reduce their service life compared to straight track.

Frog (Fig. 2)

- Traffic safety (9): The frog is the point where the wheel flange crosses the rail. Any defect or excessive wear in the frog can cause a derailment. Modern movable-point frogs significantly improve safety.
- Operating speed (8): The type and condition of the frog (particularly the presence of a movable point) strongly influence the permissible train speed. The impact effect when passing over a fixed frog limits speed.
- Maintenance costs (10): The frog is one of the most heavily loaded and most worn elements. Repair, welding, and replacement costs are among the highest in the switch.
- Service life (9): Although the frog is highly susceptible to wear, modern technologies and materials (e.g., high-manganese steel, movable-point designs) can significantly extend its service life.

Figure 2. Frog with guard rail of a R65 switch, 1/11 crossing, track gauge 1 435 mm (Ukraine)

Closure curve

- Traffic safety (7): Similarly to the switch curve, it is important for safe exit from the turnout but is less critical than the active elements.
- Operating speed (7): Its geometry also affects the smoothness of train movement, but it is generally not a decisive factor for the maximum permissible turnout speed.
- Maintenance costs (6): Maintenance costs are comparatively lower than for other elements.
- Service life (6): The service life may be somewhat shorter than that of straight track due to curvature, but longer than that of active elements.

The above evaluations were used as input data for the AHP, where they were compared pairwise to further determine the weighting coefficients of each turnout element according to each criterion (Tables 2-4).

Table 2. Evaluation of turnout elements by criteria (10-point scale)

Turnout element	Traffic safety	Operating speed	Maintenance costs	Service life
Switch points	10	9	9	8
Switch curve	8	10	7	7
Frog (crossing nose)	9	8	10	9
Closure curve	7	7	6	6

Table 3. Pairwise comparison of turnout elements by criteria

Turnout element	Switch points	Switch curve	Frog	Closure curve
		Criterion: Traffic safety		
Switch points (10)	**1**	2	1/3	1/3
Switch curve (8)	1/2	**1**	1/3	1/3
Frog (9)	3	3	**1**	2
Closure curve (7)	3	3	1/2	**1**
		Criterion: Operating speed		
Switch points (9)	**1**	1/2	2	3
Switch curve (10)	2	**1**	3	4
Frog (8)	1/2	1/3	**1**	2
Closure curve (7)	1/3	1/4	1/2	**1**
		Criterion: Maintenance costs		

DOI: 10.55343/CogSust.20523

Turnout element	Switch points	Switch curve	Frog	Closure curve
Switch points (9)	**1**	2	1/2	3
Switch curve (7)	1/2	**1**	1/3	2
Frog (10)	2	3	**1**	4
Closure curve (6)	1/3	1/2	1/4	**1**
		Criterion: Service life		
Switch points (8)	**1**	2	1/2	3
Switch curve (7)	1/2	**1**	1/3	2
Frog (9)	2	3	**1**	4
Closure curve (6)	1/3	1/2	1/4	**1**

Table 4. Pairwise comparison of criteria by importance

Turnout element	Traffic safety	Traffic speed	Operating costs	Service life
Traffic safety	1	5	7	7
Traffic speed	1/5	1	3	3
Operating costs	1/7	1/3	1	2
Service life	1/7	1/3	1/2	1

Traffic safety has an overwhelmingly strong advantage over all other criteria, since it is a fundamental requirement of railway transport. Traffic speed has a moderate advantage over operating costs and service life, as it is a key indicator of the efficiency of modern railway operations. Operating costs have a moderate advantage over service life, because direct expenses for regular maintenance and track repairs are often more tangible and immediate than full replacement of elements due to the end of their service life.

After constructing the matrices (Tables 2–4), the next steps in the Analytic Hierarchy Process (AHP) include: normalization of matrices (calculating the sum of each column and dividing each element by the column sum); calculation of weight coefficients (priority vectors) by averaging the values across rows of the normalized matrices. This provides the weight coefficients for each turnout element under each criterion, as well as the weight coefficients of the criteria themselves. Then, the consistency index *(CI)* and consistency ratio *(CR)* are computed for each matrix (a solution is considered acceptable if $CR < 0.1$).

Based on the obtained evaluations and calculations, the turnout elements are ranked by priority as follows (Fig. 3):

1. Frog (core): 0.395 (highest priority, explained by its critical importance for safety, operating costs, and service life)
2. Closure curve: 0.234 (indicating that even a “less significant” element has a substantial influence within the overall system)
3. Switch (point blades): 0.190
4. Switch curve: 0.181

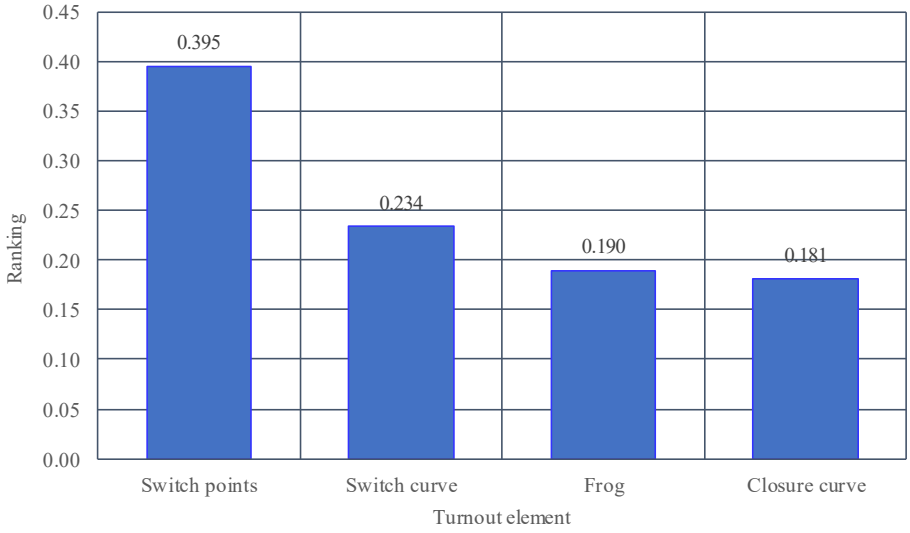

Figure 3. Ranking of turnout elements

This result indicates that the frog is the most critical element in terms of its overall impact on all considered criteria, particularly given the weight of safety. This is entirely logical, as the frog is the most heavily worn and complex section, influencing safety (impact loads), speed (especially with a movable point), and maintenance costs.

The Analytic Hierarchy Process (AHP) allows for the detailed analysis of complex elements such as the frog, breaking them down into sub-elements and conducting alternative design evaluations. For example, frogs may vary in type and design: with a solid nose or a movable nose (Table 1). Railway operating conditions affect the performance indicators of frogs (Table 5).

DOI: 10.55343/CogSust.20523

Table 5. Operational performance depending on frog type and grade

Performance indicator	Movable nose vs. Solid	Frog grade
1. Traffic safety	Frogs with a movable nose provide a significantly higher level of safety at high speeds, as they eliminate the impact section. Therefore, in pairwise safety comparisons, they have a much higher priority than solid frogs, especially for grades intended for high-speed traffic.	For the same design, a 1/18 frog is safer for high-speed passage than a 1/9 frog due to the gentler angle, although 1/9 may be sufficiently safe at lower speeds.
2. Operating speed	Frogs with a movable nose allow much higher speeds on the diverging track compared to solid frogs of the same grade. This is their key advantage.	This is a decisive factor. A 1/18 frog (especially with a movable nose) will allow significantly higher speeds than a 1/9 or 1/11 frog.
3. Maintenance costs	Movable-nose frogs are significantly more expensive to manufacture and install, and their maintenance is more complex (though less frequent under proper operation) than that of solid frogs. However, solid frogs for high-speed lines experience greater wear, requiring frequent welding and repairs, which are also costly. Overall, movable noses may have higher initial costs but lower operating costs per tonnage at high speeds.	Frogs with gentler grades (1/18) are physically larger and more expensive, but they distribute loads better, which may reduce wear.
4. Service life	Movable-nose frogs, due to smoother wheel passage, provide a longer service life for the frog and adjacent rails compared to solid frogs at high speeds. Impacts on solid frogs cause micro-deformations and accelerate wear.	For high speeds, gentler frogs (1/18) generally have a longer service life than steeper ones (1/9) under the same loads, as dynamic impacts are lower.

The generalized ranking of turnout frogs is presented in Table 6 and Fig. 4.

Table 6. Generalized ranking of turnout frogs

Frog type	Speed	Cost	Wear	Service life	Generalized rating
1/18 movable	0.482	0.096	0.482	0.444	0.376
1/11 movable	0.272	0.161	0.272	0.222	0.232
1/9 cast	0.088	0.466	0.088	0.222	0.216
1/11 cast	0.158	0.277	0.158	0.111	0.176

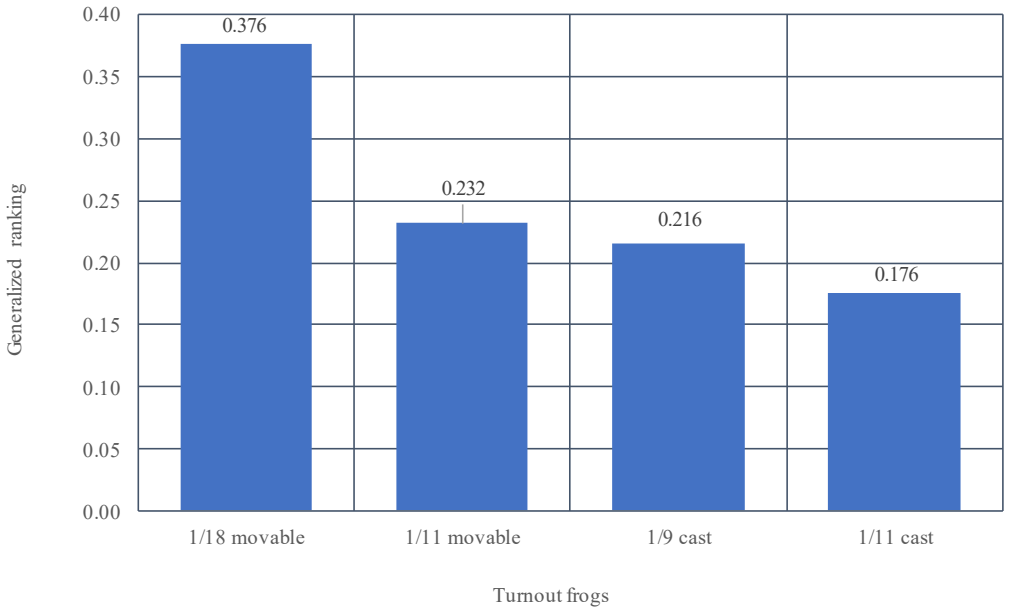

Figure 4. Ranking of frog designs

Figure 4 shows that the 1/9 frog has a higher overall rating than the 1/11 frog. In the pairwise comparison matrix for the "Speed" criterion, the 1/9 frog has poorer characteristics and received a lower score than the 1/11 frog for this criterion. However, for other criteria (such as cost, wear, and service life), the 1/9 frog received higher values, meaning it is cheaper, experiences less wear, and has a simpler design (see Tables 6 and 7).

Table 7. Advantages and disadvantages of frog nose designs

Frog type	Advantages	Disadvantages
Solid nose	Lower maintenance, simpler design	Limited speed, higher wear
Movable nose	Higher speed, reduced rail wear	More complex design, higher cost

Thus, the highest overall priority was assigned to the 1/18 movable-nose frog, indicating the best balance among the evaluated criteria. The lowest priority was assigned to the 1/11 solid-nose frog. These results can be used to make informed decisions when selecting frog designs during the design or modernization of turnouts.

In this study, a comprehensive approach was applied to the evaluation of turnout elements, integrating classical technical and economic indicators with cognitive analysis. This methodology shows how engineering decisions affect the perception and decision-making speed of personnel, which is critically important for ensuring safety at high speeds.

DOI: 10.55343/CogSust.20523

Using the Analytic Hierarchy Process (AHP), the priority of criteria for high-speed operations was justified. It was shown that traffic safety has an overwhelmingly strong advantage, highlighting its key role in the context of cognitive safety. It was also established that traffic speed moderately outweighs operating costs, which in turn have a greater impact than service life, reflecting the operational significance of each factor for railway infrastructure efficiency.

Based on the calculations, the priority of turnout elements was determined as follows: frog (0.395), closure curve (0.234), switch (point blades) (0.190), and switch curve (0.181). This result is supported by both technical and cognitive concentration.

4. Conclusion

The authors have refined the methodology for comprehensive evaluation of turnout elements by integrating cognitive analysis with the Analytic Hierarchy Process (AHP). This approach extends traditional engineering criteria (safety, speed, costs, service life) to incorporate the specifics of human factors and cognitive perception in high-speed railway operations. The main findings of the study are as follows:

- Based on expert analysis and AHP calculations, traffic safety was identified as the highest-priority factor for high-speed operations. Importantly, this safety depends not only on the technical excellence of the design but also on how intuitive and predictable the behavior of turnout elements is for both drivers and maintenance personnel.
- The calculated weight coefficients for the main turnout components showed that the frog (0.395) is the most critical element. This high priority is due not only to its complex design and high wear but also to its direct impact on visual perception and train dynamics, requiring increased attention and rapid decision-making from the driver.
- The study considered cognitive risks associated with specific turnout elements. For example, higher operating speeds can shift priority to the switch (point blades) as the element demanding the greatest concentration and cognitive processing from the driver at the moment of route setting. This confirms the hypothesis that priorities depend on operational conditions.
- The proposed methodology allows not only the evaluation but also the design of turnouts considering their "cognitive compatibility. " The results of the study can be applied for:
    1. Developing optimal maintenance strategies that account for potential human-factor-related risks.
    2. Making informed choices of frog types, particularly considering their influence on visual perception and driver reaction time.
    3. Determining priorities for major repairs on high-speed lines, where cognitive safety is a decisive factor.

Acknowledgement

The research results presented in this article were obtained as part of the scientific work carried out by the staff of the Ukrainian State University of Science and Technologies, entitled "Study of the Condition and Prospects for the Development of Railway Track Facilities". The paper was supported by the SZE-RAIL Research Team. The research has not received any financing for the article process charge.

References

Barkhordari, P., Galeazzi, R., Tejada, A., Santos, I. (2019). Identification of behavioural models for railway turnouts monitoring. *arXiv*. 1910.06582. DOI: 10.48550/arXiv.1910.06582

Barkhordari, P., Galeazzi, R., Blanke, M. (2021). Monitoring of Railpad Long-term Condition in Turnouts Using Extreme Value Distributions. *arXiv*. DOI: 10.48550/arXiv.2101.02567

Boghani, H. C., Ambur, R., Blumenfeld, M., Saade, L., Goodall, R. M., Ward, C. P., Plášek, O., Gofton, N., Morata, M., Roberts, C., Dixon, R. (2021). Sensitivity enriched multi-criterion decision making process for novel railway switches and crossings − a case study. *European Transport Research Review*, 13, 6. DOI: 10.1186/s12544-020-00467-x

Endsley, M. R. (1995). Toward a Theory of Situation Awareness in Dynamic Systems. *Human Factors*. 37(1), 32–64. DOI: 10.1518/001872095779049543

Fischer, S. (2022). Geogrid reinforcement of ballasted railway superstructure for stabilization of the railway track geometry–A case study. *Geotextiles and Geomembranes*. 50(5), 1036–1051. DOI: 10.1016/j.geotexmem.2022.05.005

Fischer, S. (2023). Evaluation of inner shear resistance of layers from mineral granular materials. *Facta Universitatis, Series: Mechanical Engineering*. Online first. DOI: 10.22190/FUME230914041F

Fischer, S. (2025). Investigation of the Settlement Behavior of Ballasted Railway Tracks Due to Dynamic Loading. *Spectrum of Mechanical Engineering and Operational Research*. 2(1), 24–46. DOI: 10.31181/smeor21202528

Fischer, S., Kurhan, M., Kurhan, D. (2025a). Innovative Technologies and Cognitive Factors for Enhancing Safety of Train and Car Movement at Level Crossings. In Zöldy, M. (ed.), *Proceedings of the 3rd Cognitive Mobility Conference. COGMOB 2024. Lecture Notes in Networks and Systems*. 1258. Springer, Cham. 1–13. DOI: 10.1007/978-3-031-81799-1_1

Fischer, S., Hermán, B., Sysyn, M., Kurhan, D., Szürke, S. K. (2025b). Quantitative analysis and optimization of energy efficiency in electric multiple units. *Facta Universitatis, Series: Mechanical Engineering*, 23(2), 351–375. DOI: 10.22190/FUME241103001F

DOI: 10.55343/CogSust.20523

Krmac, E., Djordjević, B. (2017). An evaluation of train control information systems for sustainable railway using the analytic hierarchy process (AHP) model. *European Transport Research Review*. 9, 35. DOI: 10.1007/s12544-017-0253-9

Kovalchuk, V., Sysyn, M., Sobolevska, J., Nabochenko, O., Parneta, B., Pentsak, A. (2018). Theoretical study into efficiency of the improved longitudinal profile of frogs at railroad switches. *Eastern-European Journal of Enterprise Technologies*. 4(1) (94), 27–36. DOI: 10.15587/1729-4061.2018.139502

Nyström, B., Söderholm, P. (2008). Selection of maintenance actions using the analytic hierarchy process (AHP): decision-making in railway infrastructure. *Structure and Infrastructure Engineering*. 6(4), 467–479. DOI: 10.1080/15732470801990209

Polishchuk, O. (2021). Models and methods of complex evaluation of complex network and hierarchically network systems. Dissertation abstract for Technical Sciences Doctor Degree, specialty 01.05.04 – System analysis and theory of optimal decisions. Taras Shevchenko National University of Kyiv, Ministry of Education and Sciences of Ukraine. *arXiv*. DOI: 10.48550/arXiv.2104.13852

Reason, J. (1990). *Human Error*. Cambridge University Press, Cambridge. DOI: 10.1017/CBO9781139062367

Saaty, T. L., Kułakowski, K. (2016). Axioms of the analytic hierarchy process (AHP) and its generalization to dependence and feedback: The analytic network process (ANP). *arXiv preprint*, 1605.05777. DOI: 10.48550/arXiv.1605.05777

Saaty, T. L., Shang, J. S. (2007). Group decision-making: Head-count versus intensity of preference. *Socio-Economic Planning Sciences*, 41(1), 22–37. DOI: 10.1016/j.seps.2005.10.001

Saaty, T. L., Tran, L. T. (2007). On the invalidity of fuzzifying numerical judgments in the Analytic Hierarchy Process. *Mathematical and Computer Modelling*, 46(7–8), 918–925. DOI: 10.1016/j.mcm.2007.03.022

Taha, H. A. (2017). *Operations research: An introduction*. 10th edition. Pearson Education Limited, Harlow..

Wang, P., Yang, L., Wang, S., Zhang, H., Han, L., Jing, G. (2024). Evaluation and maintenance method for general speed railway turnouts based on multi-source data. *Construction and Building Materials*. 451, 138896. DOI: 10.1016/j.conbuildmat.2024.138896

Zöldy, M., Baranyi, P., Török, Á. (2024). Trends in Cognitive Mobility in 2022. *Acta Polytechnica Hungarica*. 21(7), 189–202. DOI: 10.12700/APH.21.7.2024.7.11

https://doi.org/10.55343/CogSust.20526

Deployment of Industrial Robotic Turbocharger Manipulator into the Production Process – Construction of a Crate Feeder Workstation

Miroslav Blatnický
0000-0003-3936-7507
Department of Transport and Handling Machines, University of Žilina
Žilina, Slovak Republic
miroslav.blatnicky@fstroj.uniza.sk

Ján Dižo
0000-0001-9433-392X
Department of Transport and Handling Machines, University of Žilina
Žilina, Slovak Republic
jan.dizo@fstroj.uniza.sk

Alyona Lovska
0000-0002-8604-1764
Department of Transport and Handling Machines, University of Žilina
Žilina, Slovak Republic
alyona.lovska@fstroj.uniza.sk

Ivana Domaniková
0000-0000-0000-0000
Department of Transport and Handling Machines, University of Žilina
Žilina, Slovak Republic
ivana.domanikova@fstroj.uniza.sk

Patrik Slušňák
0009-0007-2463-3370
Department of Transport and Handling Machines, University of Žilina
Žilina, Slovak Republic
patrik.slusnak@fstroj.uniza.sk

Abstract

An industrial enterprise can remain competitive only if its production process is continually made more efficient. An analysis of operators' workload in a real-world operation involving balancing turbochargers for internal combustion engines has shown that cyclically repetitive and strenuous human work can be optimised through automated processes. For this reason, there is room for applied research, resulting in the machine's ability to reproduce only the necessary manipulation activities required in the turbocharger balancing process. Therefore, the proposed automatic line includes balancing machines to determine the amount and location of unbalanced masses on the turbocharger rotor. Following the overall resolution of the issue, a significant increase in the efficiency of a technologically feasible workplace, adapted to the needs of modern industry, is expected.

Keywords

motion, turbocharger, automation, robotic workplace, structural design

https://doi.org/10.55343/CogSust.20526

1. Introduction

The present era is marked by numerous innovations that continually bring new demands for production and development. Therefore, industrial robotic manipulators have become integral to most production processes. Their main advantage is the possibility of continuous operation and a high level of accuracy, force and speed that a person cannot achieve. This method of operation allows manufacturers to increase production and reduce the costs of manufacturing their products. Reliability and a minimal failure rate are key factors when designing equipment intended for automated processes. It is essential to understand the current state of equipping industrial robotised workplaces for the successful deployment of automated processes in production (Eller et al., 2022). Therefore, a brief description of the types of industrial robots, sensors, and their use, as well as optical machine vision systems and effectors coming into physical contact with the transmitted component (in this case, a turbocharger), is an essential part of this work.

An industrial robot can be defined using the PN-EN ISO 8373:2011 standard (ISO 8373:2021, 2021), which states: "... a handling industrial robot is an automatically controlled, programmed, multi-purpose machine with many degrees of freedom that can manipulate and transport workpieces, can be stationary or mobile, for important industrial applications". The standard also specifies the basic parameters of industrial robots:

- The number of controlled axes, typically depending on the robot, ranges from 2 to 7; this parameter determines the degrees of freedom, which are reflected in the degree of complexity of the robot's actions. Each axis has a specific range of angular movements.
- Payload, i.e., the maximum weight the industrial robot can lift or move to another location.
- Reach is defined as the radius of the robot's work area.
- Movement speed determines the maximum speed at which the robot can move in each axis. This parameter is defined in rad/s for rotary axes or mm/s for linear axes.
- Accuracy and repeatability determine the accuracy of the robot's movement. Industrial robots consist of 3 basic elements:

a) A manipulator – the power part of the industrial robot;
b) A control unit – the controller of the industrial robot (electronic systems for drive, safety, logic);
c) A robot control panel is a remote control for the industrial robot (Engineering, 2025).

Industrial robots are utilised in various industries. However, it is essential to consider the robot's movement capabilities, safety, economic feasibility, load capacity, and other relevant factors when selecting a robot for a specific application. When making this choice, there are several options:

- Articulated robotic arms (provide the most flexible movement) (Machine Design, 2025),
- Cartesian robots (used mainly for cutting, drilling, welding and other technological operations) (Siciliano et al., 2010),
- Delta robots (for high-speed and precise assembly work) (Daily Automation, 2025),
- SCARA robot (used mainly for material transfer) (Mitsubishi Electric, 2025).

The analysis of the current state of industrial robots reveals that they are suitable for use wherever it is possible to replace human labour with a robot, i.e., in monotonous, physically demanding activities, and where necessary to achieve a given quality and repeatable accuracy. As seen from the operations for which robots are used, they are primarily employed in processes that can reduce operating time, enhance accuracy, and replace workers in hazardous working conditions (e.g., paint shops, welding shops, and radiation environments).

This article aims to present the results obtained during the design, development and production of a system for automating a production cell consisting of several turbocharger balancers (3 pieces) and the integration of an automatic crate feeder with a CHRA – Centre Housing Rotating Assembly (centre rotating assembly of the turbocharger). The aim is to design an automated cell in cooperation with two or three robots. The design's motion capabilities should reproduce all manipulation activities a human operator performs, as when the balancer is in manual operation. The analysis of manual operation revealed that input crates containing unbalanced CHRAs are inserted into the line on trolleys by the operator, where the crate feeder receives them. Subsequently, individual CHRAs are removed from the crate using an industrial robot. This component is oriented by the robot and inserted into the balancing device in a precisely defined position and orientation. After balancing,

https://doi.org/10.55343/CogSust.20526

the CHRA is automatically removed from the balancer and placed on the output conveyor. Then, the conveyor ensures the transport of the balanced CHRA to the output zone, where the component is manually removed by a worker and placed in the output crate. In the case of a defective CHRA, it must be placed in a designated location. The entire process was implemented with an emphasis on precision handling, repeatability of operations and minimisation of human intervention in production.

The basic factor occurring in any material handling is movement. Movement during handling occurs due to the drive of the handling unit (robot). For applications on single-purpose machines, three types of drives are offered: electric, hydraulic, and pneumatic. However, hydraulic drives are not commonly used in automation. This means they are not considered in the design options. The choice of an individual drive method depends on the tasks assigned to the machine. The electric drive of industrial robots offers several advantages, making it the preferred choice in modern industrial applications. First, it is characterised by high accuracy and repeatability of movements, which is crucial for tasks requiring fine manipulations or precise assembly operations. Electric drives also offer high energy efficiency, because their performance can be precisely regulated according to current needs, thus minimising energy consumption.

Additionally, they offer quiet operation and low maintenance requirements, as they do not contain complex hydraulic or pneumatic components. Another advantage is the easy integration with control systems, which allows precise and flexible programming of movements. In addition, electric drives offer a more environmentally friendly solution, as they do not produce waste media or emissions, contributing to industrial processes. Electric motors implement electric drives. One of the most widely used types is the AC asynchronous motor, called an induction motor. Induction motors are perhaps the most widely used type of electric motor. They are generally simple in design and robust, offering reasonable asynchronous performance: a controllable torque and speed curve, stable operation under load, and generally satisfactory efficiency (Hussen et al., 2013; Kirtley, 2005; Šavrnoch et al., 2024; Zaharia, 2019).

Pneumatic drives for industrial robots offer several advantages that make them ideal for use in specific applications where high speed and low cost are key. Due to their simple design and ease of maintenance, they are commonly used in assembly lines, e.g. when assembling small parts in the automotive industry. Pneumatic systems are ideal for driving pneumatic grippers as robot end effectors. Compressed air supplied to the line can also be used to blow off parts where possible dirt needs to be removed. Their high speed and instant start-stop capability allow them to perform repetitive tasks like sorting products or packaging goods efficiently. Additionally, the absence of electrical components that can spark when started makes them safe for use in environments with an explosion risk, such as chemical plants or refineries, where pneumatic robots are used for simple processes like opening and closing valves. Although they have lower accuracy and limited power than electric or hydraulic actuators, their flexibility and reliability make them suitable for applications where high accuracy is not required, but speed and low cost are a priority (Festo, 2018).

2. Materials and methods

The design of any product, including automation lines, begins with compiling specific requirements. These requirements are selected based on specific needs (e.g., dimensional, performance, economics, etc.). The requirements are listed in a document that guides the prototype's design, research, and development. All the requirements that guided the production line's design are listed in Table 1.

A manipulated turbocharger is a compressor that uses the energy of exhaust gases to drive it. It is used for additional supercharging of internal combustion engines, regardless of whether they are spark-ignition or compression-ignition units. Its main advantage is to improve the performance parameters and increase the engine torque. The turbine blades rotate due to the thermal energy of the exhaust gases. The turbocharger rotor rotates at a high speed, depending on the size, purpose, and type of turbocharger. The compressor is connected to the turbine via a shaft and sucks in fresh air, which it then compresses. After compression, the air is fed into the engine cylinders. During compression, the air is heated up to 180 °C. This heated air can be cooled in a compressed air intercooler, where its temperature is reduced and the density for filling the cylinders is increased. The compressed air temperature at the outlet of the intercooler should be approximately the same as the intake air temperature. The pressures without charge air cooling range from 0.02 to 0.18 MPa, while those with cooling range from 0.05 to 0.22 MPa.

https://doi.org/10.55343/CogSust.20526

The manipulated structural unit (Figure 1) consists of three main components: the compressor housing, the turbine housing and the bearing housing. The compressor and the turbine impeller are interconnected. They are mounted on a common shaft. The bearings are lubricated with engine oil and are very sensitive to the quality of the oil. Due to the high speeds and significant temperature differences between the compressor and the turbine, high manufacturing precision and durable materials are required.

Table 1. List of demands defining the structural design of a production line cell.

Demand	Importance	Note
Line plan	Required	Up to 6 m × 6.3 m, height up to 3.5 m
Weight transferred by the robotic arm.	Required	At least 5 kg
Fully automated operation	Required	
Various and several settings of applications and parameters	Required	
Universal system for attaching a gripper	Required	
Not damaging the transferred parts of turbochargers	Required	
Continuous operation	Required	
Primarily use electric drivetrains.	Optional	In case of pneumatic drivetrain, max. pressure of 6 bar (treated air)
Brands of robotisation (KUKA	Required	KUKA KR6/10/12
A lifetime of at least 10 years	Required	
Operation in climate conditions from 10°C to 45°C, relative humidity 90%	Required	

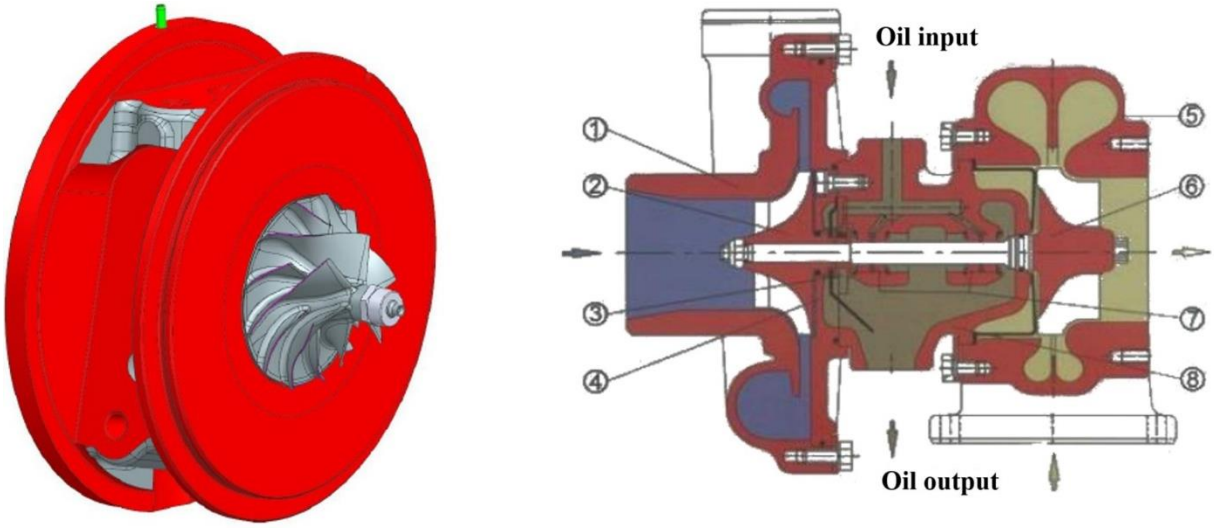

(a) (b)

Figure 1. The center of the manipulated turbocharger with a view of the compressor impeller (a) and a section through the turbocharger (bt), where the individual positions are marked: 1 – compressor housing, 2 – compressor wheel, 3 – axial oil bearing, 4 – rear wall of the compressor housing, 5 – turbine housing, 6 – turbine wheel, 7 – radial oil bearings, 8 – bearing housing.

Therefore, the proposed production line handles the turbocharger to the balancing station. Balancing must be performed on the rotating parts of the turbocharger, specifically on the compressor wheel, which is made of aluminium and mounted on a shaft within a bearing housing. This part is called the turbocharger's centre, specifically the Central Housing Rotating Assembly (CHRA). The specific dimensions of the CHRA required for the design of the gripping device are shown in Figure 2. The weight of the manipulated structural unit does not exceed 2.5 kg.

Static or dynamic balancing balances rotating parts, not just turbocharger rotors. Static balancing is a relatively simple method whose principle consists of inserting a precision shaft into a hole in the centre of the rotating part. Then, the precision

https://doi.org/10.55343/CogSust.20526

shaft is placed in carefully aligned bearing supports. If the rotating part is unbalanced, it rotates while the heaviest part is oriented downwards. When it remains in any position due to the balancing and reduction of the heavier parts, it is said to be in static equilibrium (Al Rashid et al., 2024; Lifetime Reliability Solutions, 2025; Kumar et al., 2024). However, a rotating part can be in perfect static equilibrium, but not necessarily in a balanced state, which is especially evident when rotating at high speed. If the part has the shape of a thin disk, static balancing, if carefully carried out, can be accurate at high speeds. However, if the rotating part is long in relation to its diameter, the unbalanced part may be at opposite ends or in different planes. Therefore, such parts must be balanced while rotating to reveal the imbalances using centrifugal force. This process is known as in-service balancing or dynamic balancing.

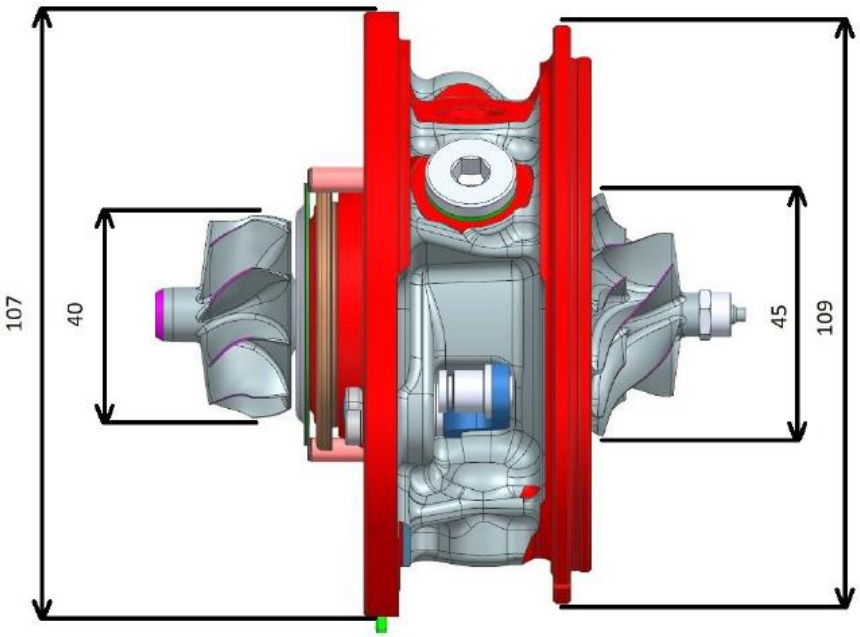

Figure 2. The main dimensions of the gripped structural unit are CHRA.

Therefore, the proposed automated line includes a balancing machine, which determines the amount and location of unbalanced masses on the turbocharger rotor. It is a device that rotates the rotor on a set of spring bearings. Thanks to the floating bearings, any imbalance causes the rotor to move off-axis as it rotates. The device measures the phase angle and amplitude of the movement and calculates the imbalance that must be present to cause the movement. The operator can then make the appropriate corrections (Norfield, 2006; ISO 21940-2:2017, 2017).

3. Results and discussion

This section presents the results of the design, research, and development process for a robotic line cell that handles turbochargers, automating their balancing on a balancing machine. The line layout is roughly determined in Table 1 based on dimensional requirements. The line consists of two robotic arms of different model series from the manufacturer KUKA, three dynamic CHRA balancers, an input section, an output section, a positioning section and a section for storing defective pieces. It also includes ancillary systems, such as fencing and suction units for operating fluids used in CHRA balancing.

The operator loads the turbocharger crates into the feeder on the trolley. The trolley is automatically locked and centred in the feeder. Sensors check the presence of the trolley. The start button starts the automatic palletising of the crates. The crates are stored on the trolley in a maximum of 10 pieces, arranged in 2 rows of 5 pieces each (Figure 4a). One row of crates is lifted by the loading mechanism (Figure 4b) and moved along the chain conveyor (Figure 4a, Figure 5b). In the final position, the individual crates can be lifted separately to the removal position for the elevator (Figure 5b). The loading mechanism transfers the crates from the trolley to the removal chain conveyor. The loading mechanism moves one row of crates at a time onto this conveyor. The mechanism consists of a frame made of welded parts, a pair of pneumatic cylinders, a separating mechanism driven by an electric motor and a chain conveyor that removes the crates from the trolley. The chain

https://doi.org/10.55343/CogSust.20526

conveyor moves the crates from the loading mechanism to the removal position and the stacked empty crates to the removal mechanism.

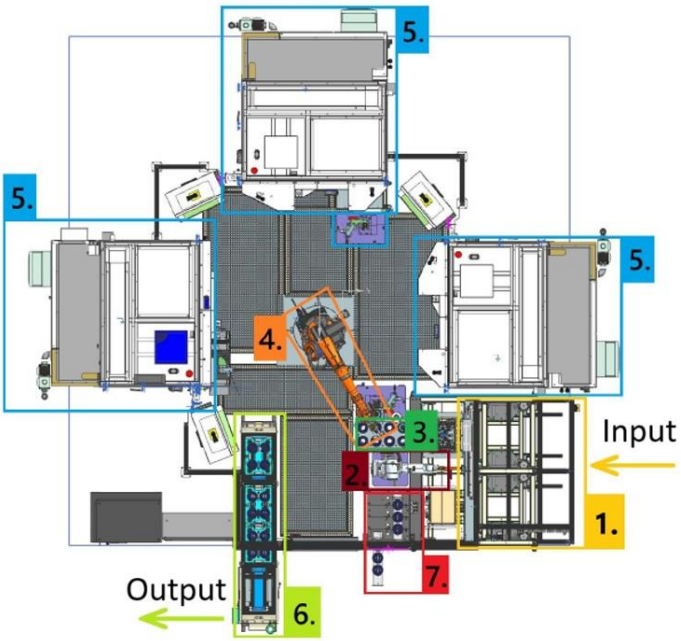

Figure 3. A floor plan of the structural design of the automation line for balancing turbochargers, individual positions are marked: 1 – crate feeder, 2 – robot no. 1, 3 – positioning beds, 4 – robot no. 2, 5 – balancers, 6 – conveyor, 7 – NOK socket.

The handling lifting unit (an elevator) is used to grip and lift the crate to the picking position for robot No. 1 (Figure 6a). After the robot empties the crate, the crate is moved to the position where the crates are stacked.

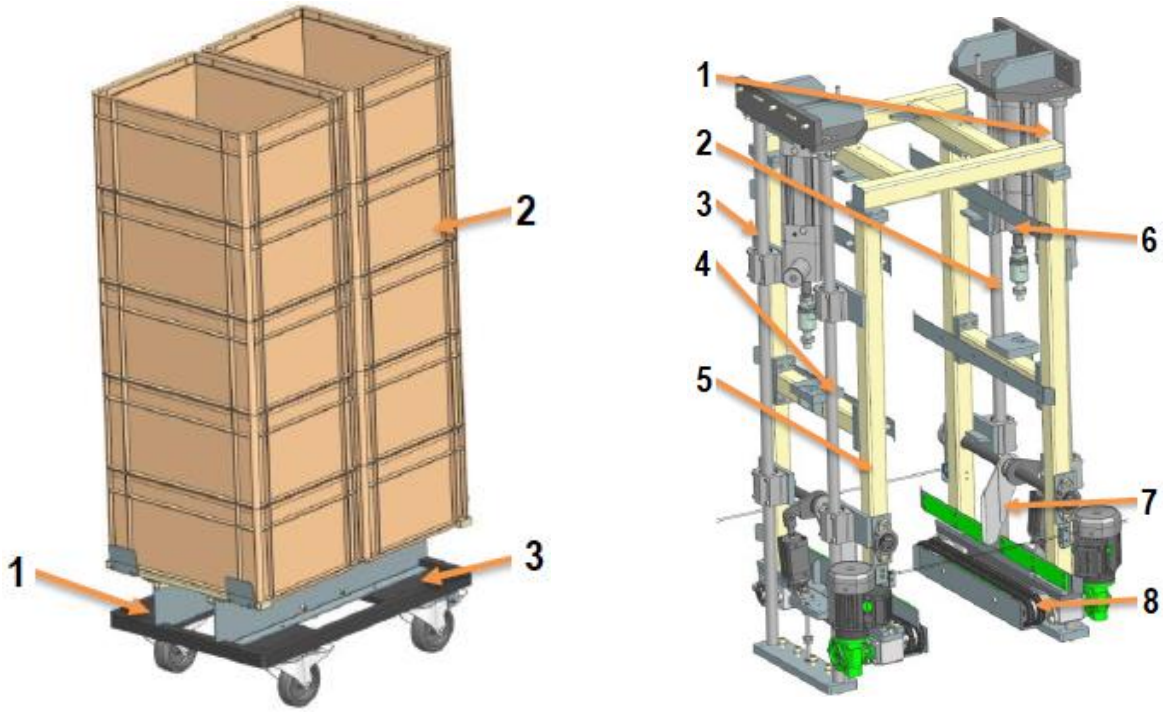

(a) (b)

Figure 4. Turbocharged crate trolley: (a) 1 – Dolly Type II 600 × 400 mm, 2 – crates, 3 – trolley superstructure; and the loading mechanism (b) 1, 2, 3, 4 – linear guides, 5 – frame, 6 – pneumatic cylinder, 7 – separation mechanism, 8 – chain conveyor.

https://doi.org/10.55343/CogSust.20526

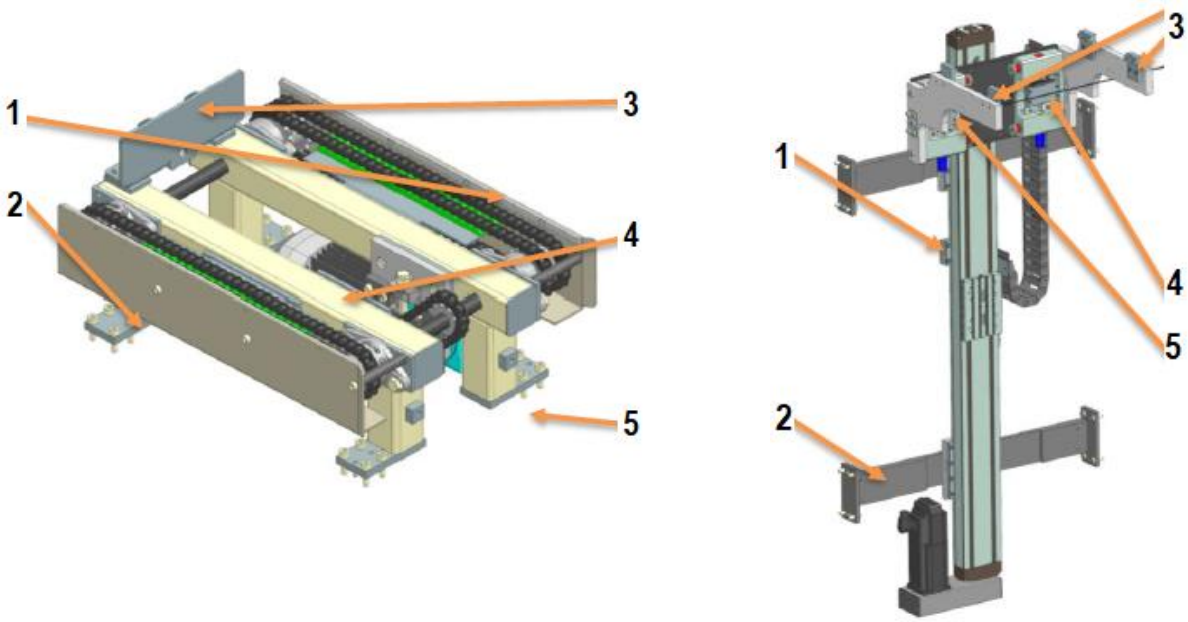

(a) (b)

Figure 5. Outfeed chain conveyor (a) 1, 2 – guide rails, 3 – stop, 4 – drive, 5 – frame; and handling lifting unit (b) 1 – Bosch Rexroth linear servo axis, 2 – frame, 3 – gripping arms, 4, 5 – pneumatic cylinders.

The frame of the device (Figure 6b) consists of welded parts assembled. The subframe is made of Bosch Rexroth profiles, and it serves as a mounting point for the safety optical gate. The handling unit for transfer (Figure 7a) is used to grip and move the empty crate from the removal position to the unloading position.

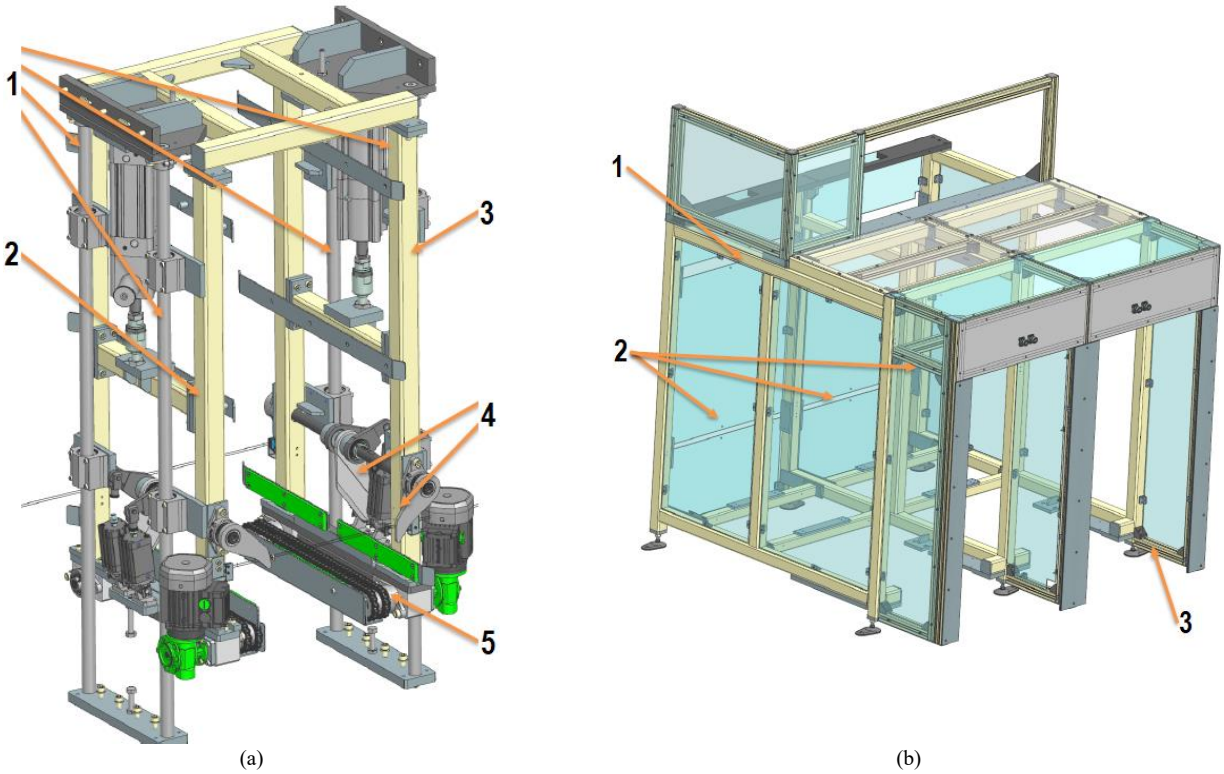

(a) (b)

https://doi.org/10.55343/CogSust.20526

Figure 6. The removal mechanism (a): 1 – linear guides, 2 – frame, 3 – pneumatic cylinder, 4 – separation mechanism, 5 – chain conveyor; and the frame structure of the designed feeder (b): 1 – frame, 2 – mechanical covers, 3 – front frame.

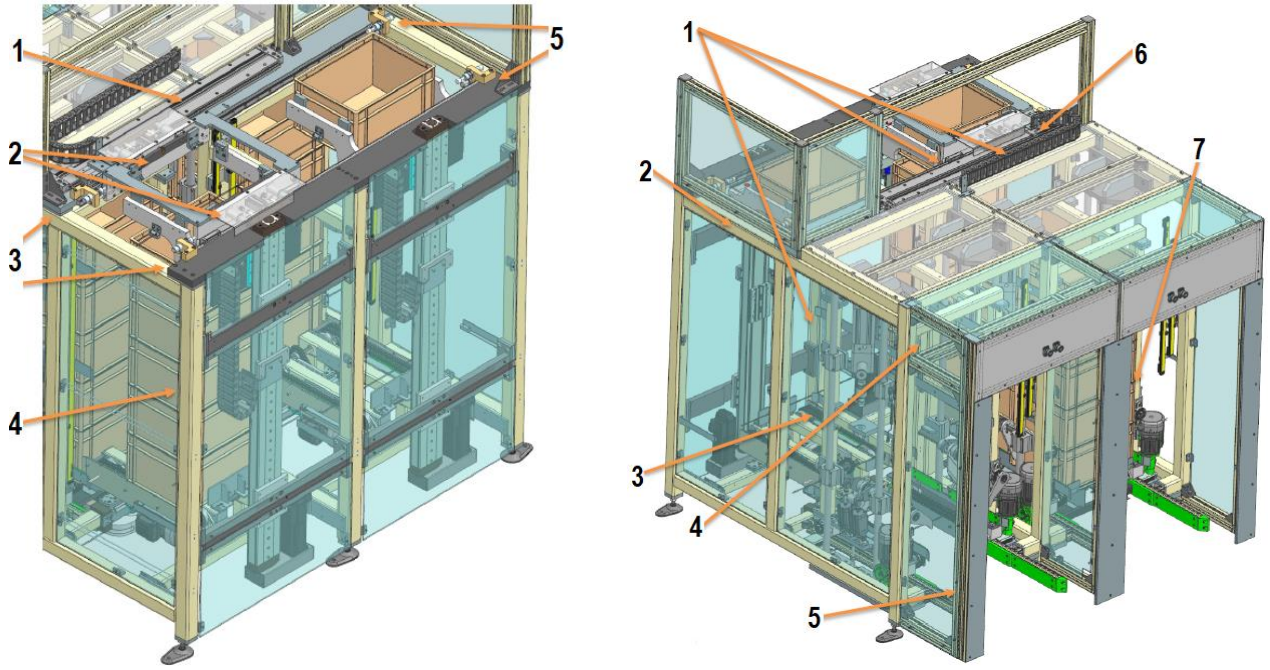

(a) (b)

Figure 7. Handling unit for transfer (a) 1 – pneumatic rodless cylinder, 2 – gripping arms, 3 – end stops, 4 – frame, 5 – end stop with damping; and crate feeder assembly (b) 1 – handling units, 2 – frame, 3 – chain conveyor, 4 – unloading mechanism, 5 – front frame, 6 – removal mechanism, 7 – loading mechanism.

The entire device (Figure 7b) consists of a steel welded and assembled frame, a subframe made of Bosch Rexroth profiles, a chain conveyor, handling units, a removal and loading mechanism, and includes safety features such as mechanical covers and optical gates.

The scientific contribution lies in creating a knowledge base for safe, reliable and efficient operation of the proposed device to maintain low energy requirements and maintenance costs. In addition, the proposed device operates with high precision, which is very important for the reliable assembly and operation of assembled components into a single unit.

4. Conclusions

The primary objective of this research is to design a robotic handling workplace for balancing turbochargers in the automotive industry. The solution analysed the technical, structural, and technological aspects crucial in designing an efficient and reliable robotic system. Requirements and technical specifications were processed, based on which the floor plan of the line was designed. The design corresponded to the rationalisation of the workspace, providing a smooth flow of materials. Given the specific requirements of turbochargers operating at extremely high speeds, implementing a dynamic balancing system was proposed to ensure the required accuracy and balance of components.

Since the conditions for safe operation of the device must be created, it is necessary to design safety elements (such as light barriers, emergency buttons, protective covers and sensors capable of detecting the presence of objects or people in risk zones). In addition, it is necessary to refine the design of the robot assembly No. 1 and No. 2, by designing additional elements: (i) the geometry of the positioning beds for storing the CHRA, (ii) the suction head for residual oil from the CHRA component, (iii) the conveyor for balanced CHRAs from inside the line to the output section, (iv) the NOK station (in case of impossibility of balancing the CHRA), (v) the end effectors (grippers together with adapters and gripping units and fingers) of individual robots supported by calculations. Last but not least, it is necessary to review the manual of the operations procedure for the robotic workplace and perform an analysis of safety requirements for the robotic workplace before installing the prototype.

Acknowledgement

https://doi.org/10.55343/CogSust.20526

This research was supported by the Slovak Research and Development Agency of the Ministry of Education, Science, Research and Sport of the Slovak Republic VEGA 1/0037/25 "Research of the Properties of the Structural Design of a New Type of Unconventional Mechanism Implementable in Light Road Vehicles with a Self-locking Effect when the Torque Differential of the Driving Axle Wheels is Required". This publication was also supported by the Cultural and Educational Grant Agency of the Ministry of Education of the Slovak Republic under project KEGA 031ŽU-4/2023: "Development of key competencies of the graduate of the study program Vehicles and Engines".

Funded by the EU NextGenerationEU through the Recovery and Resilience Plan for Slovakia under the project No. 09I03-03-V01-00131.

References

Al Rashid, J., Koohestani, M., Saintis, L., Barreau, M. (2024). Lifetime reliability modeling on EMC performance of digital ICs influenced by the environmental and aging constraints: A case study. *Microelectronics Reliability*. 159, 115447. DOI: https://doi.org/10.1016/j.microrel.2024.115447

Daily Automation (2025). Delta Robot Workplace. URL: https://www.dailyautomation.sk/wp-content/uploads/2016/05/Delta-robot_Workspace.png (Downloaded 20 August 2025 14:05)

Eller, B., Majid, M. R., Fischer, S. (2022). Laboratory tests and FE modeling of the Concrete Canvas, for infrastructure applications. *Acta Polytechnica Hungarica*. 19(3), 9–20. DOI: https://doi.org/10.12700/APH.19.3.2022.3.2

Engineering (2025). 5 základných vecí, ktoré by mal inžinier robotiky vedieť o priemyselných robotoch [5 essential things a robotics engineer should know about industrial robots]. *Engineering.* URL: https://www.engineering.sk/clanky2/automatizacia-robotizacia/30455-5-zakladnych-veci-ktore-by-mal-inzinier-robotiky-vediet-o-priemyselnych-robotoch (Downloaded 27 August 2025 09:18)

Festo (2018). Všechno elektricky! [Everything electric]. *ElektroPrůmysl*. URL: http://www.elektroprumysl.cz/automatizace/vsechno-elektricky (Downloaded: 27 August 2025 18:48)

Hussen, A. M. (2013). *Principles of Environmental Economics and Sustainability*. 3rd ed. Routledge, New York, NY.

ISO 21940-2:2017 (2017). *Mechanical vibration – Rotor balancing*. Part 2: Vocabulary. International Organization for Standardization. Geneva, Switzerland. URL: https://www.iso.org/standard/68131.html

ISO 8373:2021 (2021). *Robotics – Vocabulary*. International Organization for Standardization. Geneva, Switzerland. URL: https://www.iso.org/obp/ui/#iso:std:iso:8373:ed-3:v1:en

Kirtley, J. L. (2005). Analytic Design Evaluation of Induction Machines. In: Kirtley, J. L. (ed.). *Introduction to Power Systems*, 1st ed. Massachusetts Institute of Technology, Massachusetts, USA. 1–42. URL: https://web.mit.edu/6.685/www/chapter8.pdf

Kumar, S., Raj, K. K., Cirrincione, M., Cirrincione, G., Franzitta, V., Rahul, R. K. (2024). A comprehensive review of remaining useful life estimation approaches for rotating machinery. *Energies*. 17(22), 5538. DOI: https://doi.org/10.3390/en17225538

Lifetime Reliability Solutions (2025). *Rotating Machinery Rotor Balancing*. URL: https://rotorlab.tamu.edu/me459/Rotor%20Balancing/Rotating_Machinery_Rotor_Balancing.pdf (Downloaded 28 July 2025 08:15)

Machine Design (2025). *Differences Between Robots and Cobots*. URL: https://base.imgix.net/files/base/ebm/machinedesign/image/2016/12/machinedesign_com_sites_machinedesign.com_files_uploads_2016_10_12_1216_MD_DiffBetw_Robots_F6.png (Downloaded 28 August 2025 19:32)

Mitsubishi Electric (2025). *Mitsubishi Electric Industrial Robot Melfa FR Series*. URL: https://us.mitsubishielectric.com/fa/en/support/technical-support/knowledge-base/getdocument/?docid=3E26SJWH3ZZR-610492034-15485 (Downloaded 13 August 2025 14:32)

Norfield, D. (2006). *Practical Balancing of Rotating Machinery*. Elsevier, Amsterdam. URL: https://archive.org/details/PracticalBalancingOfRotatingMachineryDerekNorfield

Šavrnoch, Z., Sapieta, M., Dekýš, M., Ferfecki, P., Zapoměl, J., Sapietová, A., Molčan, M., Fusek, M. (2024). Probabilistic analysis of critical speed values of a rotating machine as a function of the change of dynamic parameters. *Sensors*. 24(13), 4349. DOI: https://doi.org/10.3390/s24134349

Siciliano, B., Sciavicco, L., Villani, L., Oriolo, G. (2010). *Robotics: Modelling, Planning and Control*, 1st ed. Springer-Verlag, London, UK. URL: https://nibmehub.com/opac-service/pdf/read/Robotics%20Modelling-%20Planning%20and%20Control%20by%20Bruno%20Siciliano-.pdf

Zaharia, S. M. (2019). The methodology of fatigue lifetime prediction and validation based on accelerated reliability testing of the rotor pitch links. *Eksploatacja i Niezawodnosc – Maintenance and Reliability*.21(4), 638–644. DOI: https://doi.org/10.17531/ein.2019.4.13

https://doi.org/10.55343/CogSust.20527

Study of loading of a universal container during sea transport

Alyona Lovska
0000-0002-8604-1764
Department of Transport and Handling Machines, University of Žilina
Žilina, Slovak Republic
alyona.lovska@fstroj.uniza.sk

Ján Dižo
0000-0001-9433-392X
Department of Transport and Handling Machines, University of Žilina
Žilina, Slovak Republic
jan.dizo@fstroj.uniza.sk

Miroslav Blatnický
0000-0003-3936-7507
Department of Transport and Handling Machines, University of Žilina
Žilina, Slovak Republic
miroslav.blatnicky@fstroj.uniza.sk

Abstract

Intermodal and combined container transportation is an inseparable part of a sustainable transportation system. Railway transport, in combination with railway ferry services, plays a crucial role within this system. The research presented in this contribution highlights the features of studies on the loading of a universal container when transported by a railway ferry. This research consisted of two stages: a study of the strength of a universal container when transported by a railway ferry, and a study of the container's stability relative to the frame of a flat wagon. The calculation of the container's strength was carried out using the finite element method, which is implemented in SolidWorks Simulation. It was established that the stresses in the container structure in the case of its placement on the track farthest from the bulwark exceed the permissible ones by 23%. When the container is placed on the track second from the bulwark, as well as on the middle track, the stresses are within the permissible limits. Studies of the stability against overturning of the container relative to the flat wagon frame showed that in the case of its placement on the track farthest from the bulwark, the container does not maintain equilibrium stability. Therefore, it is recommended to place flat wagons with containers on the track second from the bulwark or the middle tracks. The results of the research will contribute to the creation of recommendations for the safe transportation of containers in combined transport trains by sea, as well as the sustainable development of international freight transportation.

Keywords

container, container strength, container equilibrium stability, rail-ferry transportation, combined transportation

1. Introduction

The development of a competitive environment in the railway services market, increasing the efficiency of railway transport together with demands on sustainable transport solutions, as well as meeting the needs of the national economy and the population in transportation, leads to the development of combined transport systems (Russo et al., 2024; Čižiūnienė et al., 2024; Soloviova et al., 2020; Berki and Bede, 2025; Jóvér et al., 2025; Zalacko et al., 2020). Positive experience with operating such systems is evident from the example of rail–ferry transportation.

The increase in the efficiency of container operations along international transport corridors predicts the transportation of containers by flat wagons through the railway ferry routes of Ukraine to Georgia and Turkey (Figure 1).

https://doi.org/10.55343/CogSust.20527

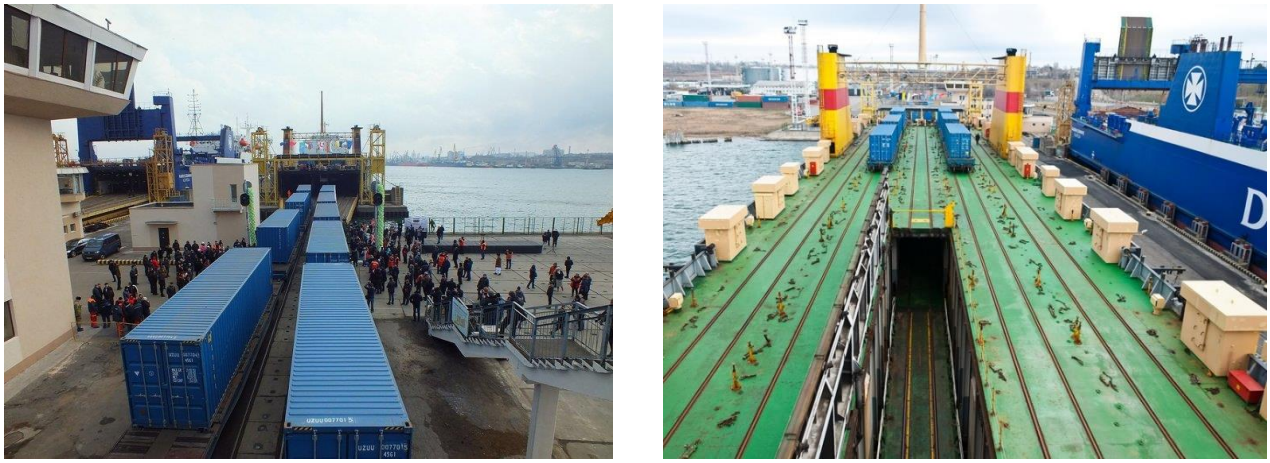

(a) (b)

Figure 1. Transportation of flat wagons loaded with containers on railway ferries: (a) rolling of flat wagons onto the railway ferry (Makeev, 2025); (b) placing of flat wagons on the railway ferry (European Pravda, 2025).

However, there are currently few developments in ensuring the technical adaptation of flat wagons for the transportation of containers by railway ferries at sea, as well as the strength of the supporting structures of containers when they are fixed to flat wagons. These objective of this research is to address these necessities.

2. Literature review

Generally, containers and flat wagons are exposed to forces due to both static loads and dynamic loads. The static load is caused by the wagon's own weight and the payload. The dynamic loads arise during wagon movement on a railway track. Excitation of a wagon together with a transported container leads to cumulation of dynamic forces, which are the result of track irregularities, such as rail joints, weld imperfections, changes of geometrical parameters and others (Fischer, 2025; Fischer et al., 2024; Jóvér et al., 2022; Ézsiás et al., 2024a; 2024b). To identify the state of the issue of studying the loading of a universal container during railway ferry transportation, an analysis of existing publications in this area was conducted. Thus, in works (Miamlyn et al., 2012; Lisowski and Czyżycki, 2011), the results of optimizing container structures are presented. The feasibility of designing and implementing containers as vehicles is substantiated. Improved container structures are developed. However, the authors did not conduct a study of the loading of containers during transportation by rail ferries.

A study of dynamic loads acting on a container during rail transportation is presented in work by Fomin (2019). The authors formed a mathematical model that describes the dynamic loading of a container placed on a platform wagon during a shunting collision. However, the authors limited themselves only to this mode of loading the container and did not study its loading during transportation by rail ferry.

A study on the dynamics of the wagon body during cargo transportation is presented in the research by Lovska et al. (2024). To determine the accelerations acting on the wagon bodies during their transportation by sea, a mathematical model of the wagon bodies' movements was developed.

The assessment of external forces acting on the wagons during transportation by rail ferry is given in Shan (2026). At the same time, the accelerations acting on the wagon bodies in conditions of sea turbulence are determined based on the calculation of the swaying of the railway ferry, which occurs with six degrees of freedom in conditions of irregular three-dimensional turbulence when moving at a speed of 6.5 knots. However, the authors Lovska et al. (2020) of the work did not study the dynamic loading of containers during sea transportation.

The analysis of publications reveals that the research on the loading of containers during railway ferry transportation requires further investigation. Therefore, the purpose of the article is to highlight the results of research conducted by the authors on the loading of containers during railway ferry transportation.

https://doi.org/10.55343/CogSust.20527

The aim of the research is to determine the loading of a universal container during transportation by a railway ferry. This aim was achieved by solving the following tasks:

- To determine the strength of a container placed on a flat wagon during transportation by rail ferry by sea;
- To investigate the stability of the equilibrium of a container placed on a flat wagon.

3. Materials and methods of research

To ensure the safety of moving flat wagons loaded with containers by sea, the supporting structure of the universal flat wagon has been improved to be reliably transported by the railway ferry, as described by Lovska et al. (2024). Since, in this case, the container is a component of the combined system "railway ferry – flat wagon – container", it is necessary to assess its strength and stability of equilibrium under the condition of placement on the flat wagon and transportation on the railway ferry.

To study the strength of the container, as a removable body unit, when placing it on the flat wagon modernization project (Lovska, 2013; NVC Wagons, 2025), which is located on the upper deck of the railway ferry, where maximum inertial loads occur under sea wave conditions of, a spatial model was developed. In general, the structural frame of the container, for example, size 1CC (Fig. 2), consists of upper and lower frames and racks. On the outside, the frame is sheathed with 1.5 mm thick corrugated steel, featuring a 150 mm corrugation pitch and a height of 12 mm. The lower frame of the container has a welded structure, assembled from two longitudinal and transverse beams made of channel No. 6.5. The upper frame is also welded and consists of two longitudinal and transverse beams, which are made of a 50×50×5 mm angle. The joints of the longitudinal and transverse beams are technologically reinforced with gusset plates. On the top, this frame is covered with a 1.5 mm thick sheet of steel. The metal sheet that forms the roof of the container is welded to the longitudinal and transverse members of the upper frame. The floor of the container is made of 25 to 27 mm thick boards (Conatainex, 2013).

When building a spatial model (3D), the main attention was paid to the elements of the real container structure, which rigidly interact with each other. The end door was replaced by a wall of equivalent rigidity, since it does not have a significant impact on the strength in conditions of angular displacements of the container around the longitudinal axis (Figure 3). Additionally, when building the model, the wooden floor was not taken into consideration.

Figure 2. An illustration of a container, size 1CC.

When drawing up the calculation scheme of the container under these conditions, the case of angular displacements of the railway ferry around the longitudinal axis (roll) was considered. This displacement has the greatest impact on the stress state and stability of the flat wagon with containers placed on it. In this case, the following loads will act on the container:

1) Vertical-static load, which is due to the mass of the container's tare and its carrying capacity;
2) Inertial load, which arises as a result of angular displacements of the flat wagon relative to the initial position;
3) Wind load.

https://doi.org/10.55343/CogSust.20527

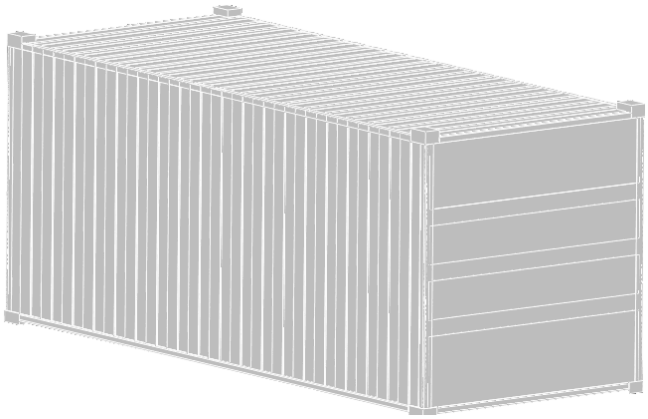

Figure 3. A spatial model of the container, size 1CC.

The limitations of this strength model are the absence of container movements relative to the supporting structure of the flat wagon, as well as longitudinal forces from the auto-coupling device.

The design function of the model is to obtain container strength indicators when placing it on the flat wagon, which is located on the upper deck of the railway ferry in rough sea conditions.

The design diagram of the container is shown in Figure 4.

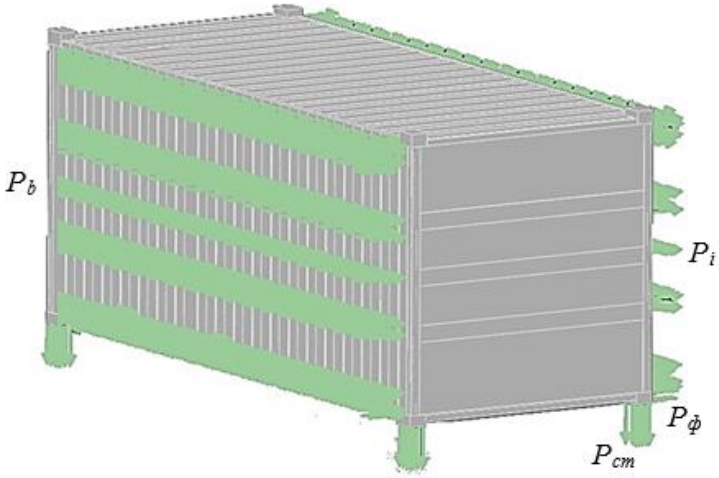

Figure 4. A calculation scheme of the container.

The loads marked in Figure 4 are as follows: P_{cm} – vertical static load; P_b – wind force acting on the container; P_i – inertial force; P_Φ – force acting on the container through the fittings during angular movements of the flat wagon around the transverse axis.

The scheme for applying loads to the container through the fitting is shown in Figure 5. It is taken into account that the vertical static load will be transmitted to the flat wagon through four points of support of the container on the flat wagon (corner fittings of the container). During angular movements of the container relative to the longitudinal axis, an additional force will arise in the zones of its interaction with the fitting stops of the flat wagon, due to the resulting horizontal load (the inertial load and the wind load). Therefore, in Figure 5, the vertical static load on the fittings is designated as P_{cm} and is applied to their horizontal surfaces. The horizontal forces on the fittings are designated as P_f.

To determine the relationships in the zones of support of the container on the fitting stops of the flat wagon, it is necessary to study its possible movements in the horizontal plane.

https://doi.org/10.55343/CogSust.20527

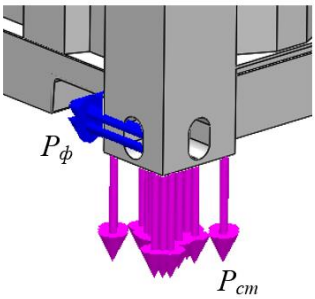

Figure 5. A diagram of the application of the loads acting on the container through the fitting (a detail).

The fixing of the container from horizontal (transverse) movements will be ensured if the following condition is met:

$$F_{mp} > P_z \tag{1}$$

where,

F_{mp} is the friction force that occurs between the horizontal plane of the container fitting [kN],

P_z is the resulting horizontal load, which includes the inertia force acting on the container in conditions of angular movements around the longitudinal axis and the wind load acting on the side wall of the container [kN].

The friction force will be determined as follows:

$$F_{mp} > P_{cm} \cdot \mu \tag{2}$$

where,

P_{cm} is the vertical-static load acting on the container [kN],

μ is the friction coefficient that occurs between the horizontal plane of the container fitting and the fitting stop plate (for the friction pair "steel - steel" $\mu = 0.03 \div 0.09$).

This load will be concentrated between the zones of support of the container on the flat wagon.
The resulting horizontal load will be:

$$P_z = P_i + P_b \tag{3}$$

where,

P_i is the inertia force acting on the container under conditions of angular displacements around the longitudinal axis [kN],

P_b is the wind load acting on the side wall of the container [kN].

This force will act on the container through the internal fittings on the slope side (Antala et al., 2021, Liguori et al, 2021).
The numerical values obtained are listed in Table 1.

Table 1. Loads acting on the container in the areas of support on the flat wagon fitting stops.

The total friction force that occurs between the horizontal plane of the container fitting and the fitting stop plate placed on the flat wagon [kN]	Friction force that occurs between the horizontal plane of the container fitting and the fitting stop plate placed on the flat wagon [kN]	Total value of the resulting horizontal load acting on the container [kN]	The magnitude of the resulting horizontal load acting on the container through the fitting stop [kN]
13.7	3.4	82.1	41.0

That is, fixing the container from movements in the horizontal plane will not be ensured.

https://doi.org/10.55343/CogSust.20527

Therefore, in the zones of support of the container on the flat wagon, additional connections were installed, which were simulated by rigid clamping, since the gross mass compared to the plane of support on the fittings has a much larger value. That is, the case was considered when the inner surface of the container fitting will interact with the vertical part of the flat wagon fitting stop. When compiling the container strength model, the assumption was made that it is loaded to the full load capacity with a conditional load. The calculated values of the forces acting on the container are given in Table. 2. The strength calculation was carried out using the finite element method (Wang et al., 2023; Yildiz, 2019). The number of nodal points in the grid was determined using the graph-analytical method. Ten-node isoparametric tetrahedra were used as grid elements (Oterkus, 2022).

Table 2. Forces acting on a container, size 1SS, gross weight 24 tons, when placed on a flat wagon located on the upper deck of the railway ferry in rough sea conditions.

Vertical static load through fitting [kN]	Inertia forces acting on the container [kN]	Wind load acting on the container [kN]	Force acting on the container through the fitting [kN]
57.3	50.2	22.8	36.4

4. Results of research

Based on the calculations, it was concluded that the stresses in the container structure exceed the permissible limits in the case of placing it on a flat wagon, located on the outermost track of the railway ferry from the bulwark, and amount to 403.2 MPa (Figure 6). The permissible stresses are taken to be 310.5 MPa (Lovska et al., 2024):.

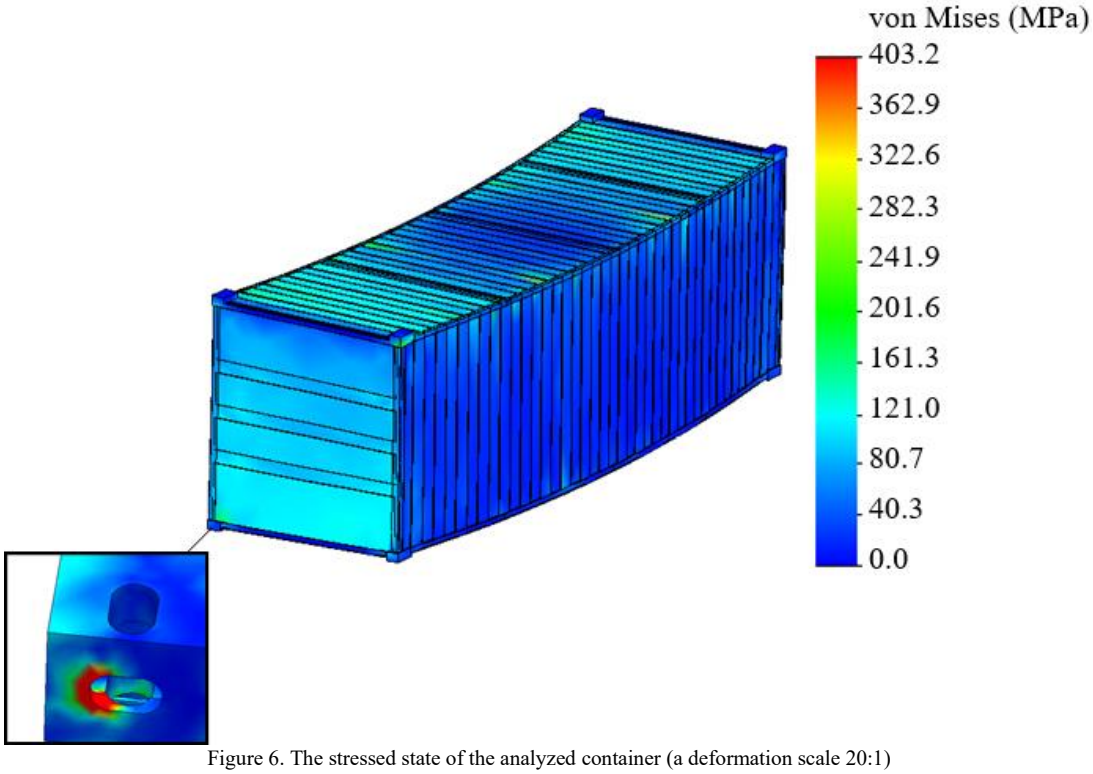

Figure 6. The stressed state of the analyzed container (a deformation scale 20:1)

The maximum equivalent deformations in the container structure are 3.24×10^{-6}, and the displacements in the nodes are 3.5 mm. There is no structural safety margin. In the case of placing the container on the flat wagon, which is located on the second and third tracks from the bulwark, its strength is ensured.

Future development of this research involves conducting an experimental study of container strength during transportation on a railway ferry. Improved container fastenings on flat wagons also require performing the research. This is crucial, as the existing container-to-flat wagon interaction system is unreliable under elevated rail ferry tilt angles (greater than 10°). This situation poses a significant risk to container tipping and the overall environmental impact of transportation. Therefore, the authors plan to devote special attention to this issue.

https://doi.org/10.55343/CogSust.20527

The conducted research will not only contribute to improved container shipping safety by sea, but also to the sustainable development of rail and ferry transportation as a segment of the transport industry. The research will also allow for the development of recommendations for the design of modern container structures with improved technical and economic characteristics.

6. Conclusions

The conducted studies on the strength of the supporting structure of a universal container when it is fixed to a flat wagon of an improved design showed that the maximum equivalent stresses do not exceed the permissible ones in the case of its location on the second track from the bulwark and the middle track of the railway ferry. In the case of placing the flat wagon with a container on the outermost track from the bulwark track, the stresses in its structure exceed the permissible ones by 23%.

Studies of the stability of the container relative to the flat wagon frame showed that, under the existing conditions of fixing the container to the flat wagon on the track farthest from the bulwark, the container's resistance against overturning is not ensured. This may compromise the stability of the whole mechanical system "flat wagon – railway – ferry". Therefore, it is proposed that, on a railway ferry navigating in conditions of large heel angles of, flat wagons loaded with containers should not be placed on the tracks farthest from the bulwark.

Acknowledgement

This research was also supported by the Slovak Research and Development Agency of the Ministry of Education, Science, Research and Sport of the Slovak Republic VEGA 1/0308/24 "Research of dynamic properties of rail vehicles mechanical systems with flexible components when running on a track". This publication was also supported by the Cultural and Educational Grant Agency of the Ministry of Education of the Slovak Republic under project KEGA 031ŽU-4/2023: "Development of key competencies of the graduate of the study program Vehicles and Engines".

Funded by the EU NextGenerationEU through the Recovery and Resilience Plan for Slovakia under the project No. 09I03-03-V01-00131.

References

Antala, D. K., Satasiya, R. M., Chauhan, P. M. (2021). Design, development and performance evaluation of transportation container for sapota fruit. *Journal of Food Sciences and Technology.* 58(10), 4024–4033. DOI: https://doi.org/10.1007/s13197-020-04865-w

Berki, Z., Bede, Á. (2025). Rail Freight Route Choice and Costing Model for Transport Modelling. In: Zöldy, M. (ed.): Proceedings of the 3rd Cognitive Mobility Conference. COGMOB 2024. *Lecture Notes in Networks and Systems*. 1258. Springer, Cham. 230–237. DOI: https://doi.org/10.1007/978-3-031-81799-1_21

Čižiūnienė, K., Matijošius, J., Sokolovskij, E., Balevičiūte. J. (2024). Assessment of implementing green logistics principles in railway transport: The case of Lithuania. *Sustainability*. 16(7), 2716. DOI: https://doi.org/10.3390/su16072716

Containex (2013). Technical specifications for steel dry cargo container. Specification NO. CTX 20 DVDR – Domestic Spec. HH. 27 pages. URL: https://www.containi.de/pdf/Technische-Beschreibung-Seecontainer.pdf

European Pravda (2025). – Європейська правда (2025). Рік транзитної війни. Що зробила та що мусить зробити Україна [The year of the transit war. What Ukraine has done and what it must do]. URL: https://www.eurointegration.com.ua/experts/2017/01/11/7059942/ (Downloaded 28 August 2025 10:15)

Ézsiás, L., Kozma, K., Tompa, R., Fischer, S. (2024a). Crushed stone supply challenges for infrastructure development in Hungary. *Naukovyi Visnyk Natsionalnoho Hirnychoho Universytetu*, 2024(6), 28–37. DOI: https://doi.org/10.33271/nvngu/2024-6/028

Ézsiás, L., Tompa, R., Fischer, S. (2024b). Investigation of the possible correlations between specific characteristics of crushed stone aggregates. *Spectrum of Mechanical Engineering and Operational Research*. 1(1), 10-26. DOI: https://doi.org/10.31181/smeor1120242

Fischer, S. (2025). Investigation of the settlement behavior of ballasted railway tracks due to dynamic loading. *Spectrum of Mechanical Engineering and Operational Research*. 2(1), 24–46. DOI: https://doi.org/10.31181/smeor21202528.

Fischer, S., Harangozó, D., Németh, D., Kocsis, B., Sysyn, M., Kurhan, D., Brautigam, A. (2024). Investigation of heat-affected zones of thermite rail welding. *Facta Universitatis, Series: Mechanical Engineering*. 22(4), 689–710. DOI: https://doi.org/10.22190/FUME221217008F

Fomin, O., Lovska, A., Píštěk, V., Kučera, P. (2019). Dynamic load computational modelling of containers placed on a flat wagon at railroad ferry transportation. *Vibroengineering Procedia*. 29, 118–123. DOI: https://doi.org/10.21595/vp.2019.21132

https://doi.org/10.55343/CogSust.20527

Jóvér, V., Kocsis Szürke, S., Hermán, B., Böröcz, P., Kuczmann, M., Fischer, S. (2025). Vehicle dynamics measurements with a unique measuring system for trams. In: Zöldy, M. (ed.) *Proceedings of the 3rd Cognitive Mobility Conference. COGMOB 2024. Lecture Notes in Networks and Systems*. 1258. Springer, Cham. 24–33. DOI: https://doi.org/10.1007/978-3-031-81799-1_3

Liguori, A., Formato, A., Pellegrino, A., Villecco, F. (2021). Study of tank containers for foodstuffs. *Machines.* 9(2), 44. DOI: https://doi.org/10.3390/machines9020044

Lisowski, E., Czyżycki, W. (2011). Transport and storage of LNG in container tanks. *Journal of KONES Powertrain and Transport.* 18(3), 193–201. URL: https://bibliotekanauki.pl/articles/245524

Lovska, A. (2013) –Ловська, (2013). Теоретичне оцінювання міцності та стійкості універсальних контейнерів за умови розміщення на вагонах-платформах при їх перевезенні на залізничних поромах [Theoretical estimation of versatile container strength under the condition of their allocation on flat cars while transporting them on railway ferries]. *Збірник наукових праць [Bulletin of Scientific Works]*. 139, 197–204. URL: https://share.google/BV02TdOUFpDKBsFqz

Lovska, A., Fomin, O., Píštěk, V., Kučera, P. (2020). Dynamic load and strength determination of carrying structure of wagons transported by ferries. *Journal of Marine Science and Engineering.* 8(11), 902. DOI: https://doi.org/10.3390/jmse8110902

Lovska, A., Gerlici, J., Dižo, J., & Rukavishnykov, P. (2024). Investigation of container strength when fixed in an open wagon equipped with pneumatic bags. *Acta Technica Jaurinensis*, 17(4), 177–182. DOI: https://doi.org/10.14513/actatechjaur.00753

Lovska, A., Gerlici, J., Dizo, J., Ishchuk, V. (2024). The strength of rail vehicles transported by a ferry considering the influence of sea waves on its hull. *Sensors.* 24(1), 183. DOI: https://doi.org/10.3390/s24010183

Makeev, V. (2025). – Макеєв, В. (2025). Шовковий шлях стане на 30% дешевше [The Silk Road will become 30% cheaper]. *NV – The New Voice of Ukraine*. URL: https://biz.nv.ua/ukr/economics/shovkovij-shljah-stane-na-30-deshevshe-125652.html (Downloaded 28 August 2025 11:25)

Miamlyn, S. V., Kebal, Yu. V., Kondratiuk, S. M. (2012). –Мямлин, С. В., Кебал, Ю. В., Кондратюк, С. М. (2012). Перспективные конструкции контейнеров-цистерн для перевозки светлых нефтепродуктов, аммиака и углеводородных газов [Prospective designs of tank containers for transportation of light petroleum products, ammonia and hydrocarbon gases]. *Залізничний транспорт України [Railway Transport of Ukraine]*. 2, 44–46.

NVC Wagons (2025) – НВЦ «ВАГОНЫ» (2025). От идеи до внедрения [From idea to implementation]. URL: nvc-vagon.ru (Downloaded 20 August 2025 09:15)

Oterkus, S., Wang, B., Oterkus, E., Kasimu Galadima, Y., Cocard, M., Mokas, S., Buckley, J., McCullough, C., Boruah, D., Gilchrist, B. (2022). Structural integrity analysis of containers lost at sea using finite element method. *Sustainable Marine Structures.* 4(2), 11–17. DOI: http://dx.doi.org/10.36956/sms.v4i2.505

Russo, F., Comi, A., Chilà, G. (2024). Dynamic approach to update utility and choice by emerging technologies to reduce risk in urban road transportation systems. *Future Transportation*. 4(3), 1078–1099. DOI: https://doi.org/10.3390/futuretransp4030052

Shan, J., & Schönberger, J. (2025). Planning container flows through the Eurasian rail network: Managing ad-hoc demand under limited capacity. Omega, 103395. DOI: https://doi.org/10.1016/j.omega.2025.103395

Soloviova, L., Strelko, O., Isaienko, S., Soloviova, O., Berdnychenko, Yu. (2020). Container transport system as a means of saving resources. *IOP Conf. Series: Earth and Environmental Science.* 459, 052070. DOI: https://doi.org/10.1088/1755-1315/459/5/052070

Wang, Z., Qian, C., Wu, Z. (2023). Stress analysis and structural improvement of LNG tank container frames under impact from railway transport vehicles. *Applied Sciences.* 13(24), 13335. DOI: https://doi.org/10.3390/app132413335

Yildiz, T. (2019). Design and analysis of a lightweight composite shipping container made of carbon fiber laminates. *logistics.* 3(3), 18. DOI: https://doi.org/10.3390/logistics3030018

Zalacko, R., Zöldy, M., Simongáti, G. (2020). Comparative study of two simple marine engine BSFC estimation methods. *Brodogradnja*. 71(3), 13–25. DOI: https://doi.org/10.21278/BROD71302

https://doi.org/10.55343/CogSust.20525

Microturbine design for sustainable fuels

Peter Kondor
John von Neumann University
Kecskemet, Hungary
kondor.peter@nje.hu

Abstract
The global shift toward sustainability and the urgent need to reduce reliance on fossil fuels have intensified research into alternative energy carriers across transportation and power generation sectors. Gas turbines and microturbines, known for their high efficiency and operational flexibility, offer a promising platform for integrating low-carbon fuels into electricity production. This study presents the design of an experimental microturbine developed to examine the combustion characteristics of sustainable gaseous fuels – specifically hydrogen and biogas – under controlled laboratory conditions. The investigation focuses on fuel applicability, combustion stability, and emission profiles, contributing to developing cleaner and more sustainable energy conversion systems. The microturbine is constructed using a commercially available automotive turbocharger, featuring a centrifugal compressor and a centripetal turbine, paired with a custom-designed counterflow combustion chamber. Component selection and chamber design are guided by engineering calculations and a thorough literature review, ensuring mechanical compatibility and experimental reliability. The setup provides a scalable and accessible platform for advancing sustainable combustion technologies.

Keywords
microturbine, sustainable fuel, emission, energetics

1. Introduction

Thanks to their unique blend of efficiency, flexibility, and environmental benefits, microturbines play a crucial role in modern energy production. Microturbines are ideal for decentralised power systems, allowing energy to be produced close to where it is consumed. This reduces transmission losses and enhances grid resilience. They efficiently generate both electricity and usable heat from a single fuel source. This dual output makes them perfect for industrial facilities, commercial buildings, and residential complexes. Microturbines can run on various fuels, including natural gas, biogas, and hydrogen. This adaptability supports the transition to cleaner energy sources.

These systems produce significantly lower nitrogen oxides (NOx) and carbon monoxide (CO) levels than traditional combustion engines, helping meet strict environmental regulations. Microturbines can reach full capacity in under two minutes and adjust quickly to changing energy demands, making them excellent for backup power and peak load support. Their small footprint and low noise make them suitable for urban environments and space-constrained installations. Multiple units can be combined to meet larger energy needs, offering scalability without sacrificing efficiency.

Microturbines are increasingly important as we shift toward a carbon-free energy grid. They complement intermittent renewable sources like solar and wind by providing reliable backup and grid stability. Their ability to hybridise with renewables and operate off-grid makes them a cornerstone of sustainable energy systems.

2. Background: Thermodynamics of the operating principle of gas turbines

The air-standard Brayton cycle is ideal for the simple gas turbine (GT). The simple open-cycle GT utilises an internal-combustion process, and the simple closed-cycle gas turbine utilises heat transfer (Mikielewitz et al, 2019a). Both cycles are schematically shown in Figure 1.

https://doi.org/10.55343/CogSust.20525

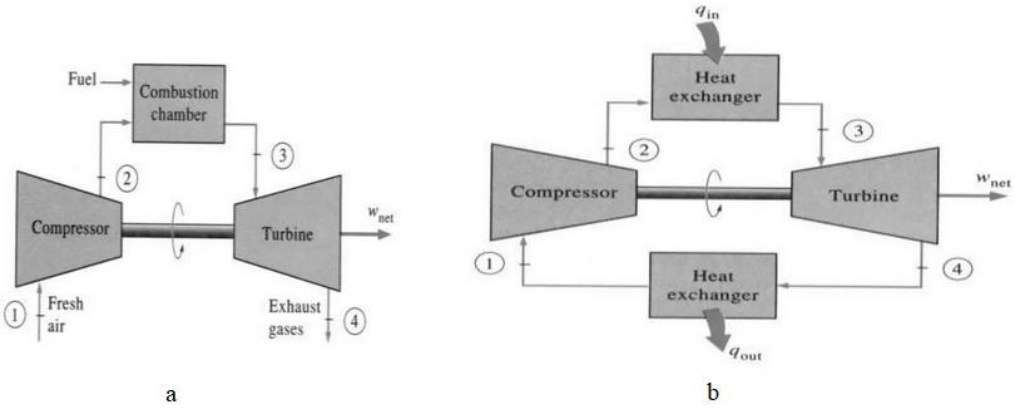

Figure 1. Gas turbine cycles (a) Open-cycle, (b) Closed-cycle

The thermal efficiency (η_t) of a simple Brayton-cycle can be determined based on the following Equation (1), based on (Korakianitis, Wilson, 1994):

$$\eta_t = 1 - \frac{T_4 - T_1}{T_3 - T_2} = 1 - \frac{1}{\left(\frac{p_2}{p_1}\right)^{\frac{K-1}{K}}} = 1 - \frac{1}{(\pi_k)^{\frac{K-1}{K}}} \quad (1)$$

It depends on the pressure ratio (π) of the compressor and the specific heat ratio of the working fluid *(K)*.

The total output work *(W)* is derived from the difference between turbine work *(W_t)* and compressor work *(W_c)*, equation (2).

$$W = W_t - W_c \quad (2)$$

The efficiency increase with pressure ratio is evident from the entropy diagram of the simple Brayton cycle, as shown in Figure 2.

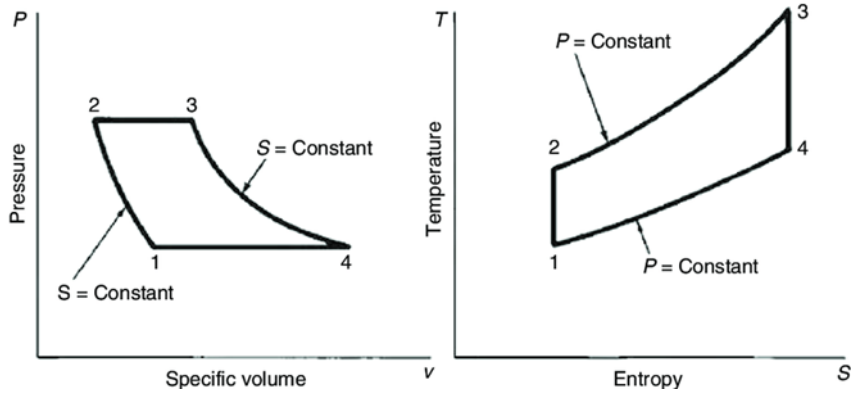

Figure 2. P-V and T-S diagrams of a standard air Brayton-cycle

The fuel required to raise the temperature from 2 to 3 is:

$$\dot{m}_f = \frac{h_3 - h_2}{LHV\eta}\,[\text{kg}] \quad (3)$$

where h_2 and h_3 are the enthalpies, the *LHV* is the lower heating value, and η is the thermal efficiency. Many fuels can be used in gas turbines (Mikielewicz et al., 2019b) because, due to their operating principle, they are

https://doi.org/10.55343/CogSust.20525

less sensitive to calorific value than piston engines. Table 1 shows the classification of applicable fuels according to their calorific value (Hunicz et al., 2020; Annamalai et al., 2016; Emőd et al., 2005; Zöldy and Kondor, 2021).

Table 1. Classification of fuels

Classification of fuel	Typical composition	LHV [MJ/kg]	Typical specific fuels
Ultra Low LHV gaseous fuels	H_2 < 10% CH_4 < 10% N_2 + CO > 40%	< 11.200 (< 300)	Blast furnace gas Inert gas Biogases
High hydrogen gaseous fuels	H_2 > 50% C_xH_y = 0–40%	5.500–11.200 (150–300)	Refinery gas Petrochemical gas Hydrogen power
Medium LHV gaseous fuels	CH_4 < 60% N_2 + CO_2 = 30–50% H_2 = 10–50%	11.200–30.000	Weak natural gas Landfill gas, Coke oven gas, Corex gas
Natural gas	CH_4 = 90% C_xH_y = 5% Inert = 5%	30.000–45.000	Natural gas Liquefied natural gas
High LHV gaseous fuels	CH_4 and higher hydrocarbons C_xH_y > 10%	32.000–45.000	Liquid petroleum gas (butane, propane) Refinery off-gas
Liquid fuels	C_xH_y, with x > 6	32.000–45.000	Kerosene, Diesel oil, Naptha, Crude oils, Residual oils, Bio-liquids

Source: own compilation based on (Canakci, Sanli, 2008), (Suchockiet al., 2023).

3. Combustion chamber selection for experimental application

A counterflow combustion chamber is a special design commonly used in gas turbines and microturbines, where the hot combustion gases flow opposite to the incoming compressed air. This reversed, U-shaped flow path makes the chamber more compact and reduces the overall engine length compared to straight-through combustors. Compressed air enters at the rear section and flows forward around the combustion liner, with part of the air being directed through swirlers and holes into the liner for fuel–air mixing. Fuel is injected into the liner and stabilised by vortex generators or swirl vanes, creating a stable flame and efficient combustion. Meanwhile, cooling air flows along the outer liner walls to protect them from excessive heat, while dilution holes near the downstream section introduce additional air to reduce the exit temperature before the gases turn back toward the turbine inlet. This counterflow arrangement not only helps with compactness but also improves thermal management of the casing, as the reversed gas flow distributes heat more evenly. Efficient mixing of fuel and air is critical to avoid hot spots and to maintain low emissions, often supported by staged fuel injection. At the same time, the design reduces pressure losses compared to long straight combustors, which increases efficiency (Casey, Schlegel, 2010). Despite these advantages, the counterflow combustor must be carefully engineered to ensure uniform temperature distribution at the turbine inlet and to withstand high thermal gradients and cyclic loads. This configuration combines compact size, effective cooling, and stable performance, making it a reliable choice in many modern turbine applications. Based on literature research, the planned combustion chamber construction is shown in Figure 3.

https://doi.org/10.55343/CogSust.20525

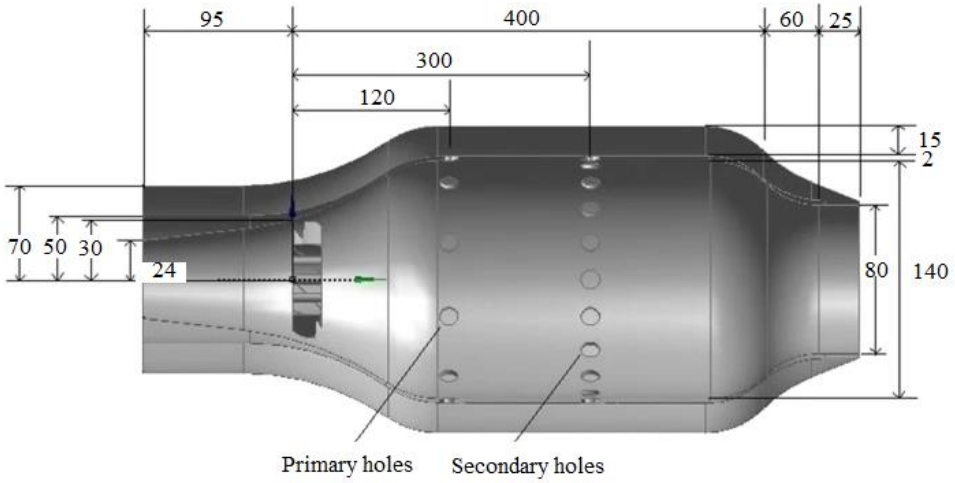

Figure 3. Designed counterflow combustion chamber dimensions

The combustion chamber is made of a 2 mm thick stainless KO36Ti plate. When designing the combustion chamber, flow simulations were performed based on the mass flow of the centrifugal compressor, during which the development of the velocity conditions in the primary and secondary zones and the temperature distribution in the combustion chamber segments had to be examined. The velocity vectors and temperature distribution based on simulations are shown in Figure 4.

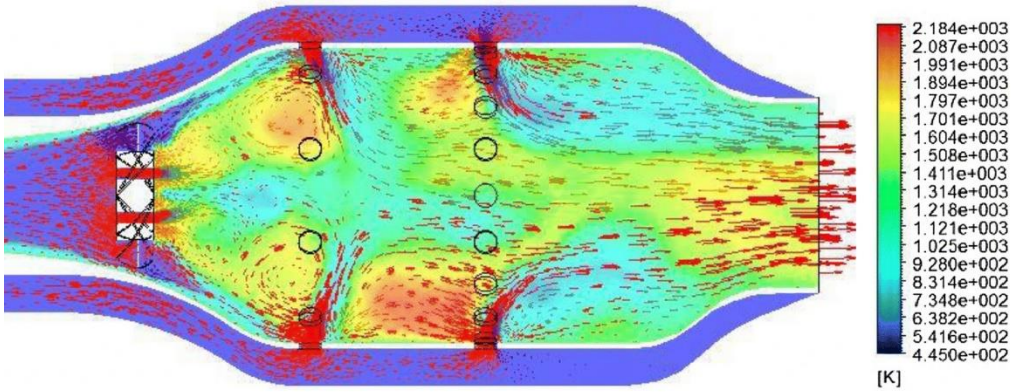

Figure 4. Velocity vectors and temperature distribution based on simulations

4. Compressor and turbine selection

A Garrett G40-1150 turbocharger powers the microturbine compressor and turbine unit. The data required for sizing is provided by the measured characteristic of the centrifugal compressor, which is shown in Figure 5.

https://doi.org/10.55343/CogSust.20525

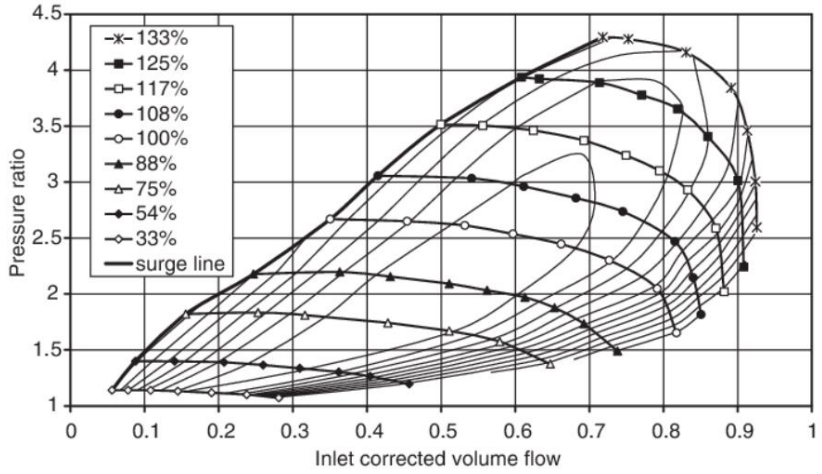

Figure 5. Compressor characteristic for the turbocharger centrifugal compressor

The pressure ratio can be determined based on the best efficiency curve as a value close to 3. The corresponding mass flow rate is 0.6 cubic meters per hour. The density at the inlet can be determined using Equation (3).

$$Q_0 = \frac{p_0}{R \cdot T_0} \tag{3}$$

The pressure is reduced to half the cross-section, based on simulation measurements between approximately 97000 Pa. From the pressure ratio, the combustion chamber pressure can be determined using Equation (4).

$$\pi = \frac{p_2}{p_1} \rightarrow p_2 = p_1 \cdot \pi \tag{4}$$

From the magnitude of the inlet and outlet pressures and the inlet density, the outlet density can be derived from the Bernoulli equation, which gives the density of the air entering the compressor. By writing and rearranging the Poisson equation (5), the outlet temperature of the confuser can be calculated.

$$\frac{T_1}{T_0} = \left(\frac{p_1}{p_0}\right)^{\frac{K-1}{K}} \rightarrow T_1 = T_0 \frac{p_1}{p_0}^{\frac{K-1}{K}} \tag{5}$$

The compression and expansion processes show an increase in entropy of Δs due to the flow and friction losses, which were still negligible in the inlet confuser. Here, the air filter that may be placed in front of the compressor must consider the gap and friction losses on the shaft. In practice, the compressor efficiency is determined based on these losses. This loss can be ignored since there is no air filter in front of the compressor. In order to achieve a constant pressure ratio in the compressor, a greater enthalpy change is required due to the losses, which means introducing a higher compressor power, which is why more heat is generated. The compressor power requirement can be calculated based on Equation (6).

$$P_k = \dot{m} \cdot c_p \cdot (T_2 - T_1) \tag{6}$$

When designing the combustion chamber, a conventional propane-butane gas was selected. Propane (C_3H_8) and butane (C_4H_{10}) are available in different proportions, but the most commonly used mixture is 60% propane and 40% butane. The heat output can be calculated using the following Equation (7):

$$\dot{Q} = \dot{m} \cdot c_p \cdot (T_3 - T_2) \tag{7}$$

Based on this, the calculated heat output during propane-butane combustion is 350 kW. When calculating the turbine power, it must be taken into account that the turbine can process a smaller enthalpy change with an

https://doi.org/10.55343/CogSust.20525

unchanged expansion pressure ratio, which results in a smaller extractable P_t turbine power. The ideal temperature, actual temperature and actual power of the turbine can be derived from the Poisson equation. The system's total power is the difference between the power of the turbine and the compressor, since part of the energy produced by the turbine is used to work in the compressor. The efficiency can be calculated by considering the losses occurring in the compressor, the combustion chamber and the turbine. The effective power of the designed microturbine is 60 kW with propane-butane fuel.

5. Conclusion

The study presents the design of an experimental microturbine, which aims to research and test sustainable fuels, mainly based on aspects of emission and applicability. The microturbine consists of a conventional automotive turbocharger and a unique counterflow combustion chamber designed based on literature research. After the construction of the microturbine, it will be possible to test gaseous and liquid components such as hydrogen, biogas, plant-based and recycled fuels and their mixtures in laboratory conditions.

References

Annamalai, M., Dhinesh, B., Nanthagopal, K., SivaramaKrishnan, P., Lalvani, J. I. J., Parthasarathy, M., Annamalai, K. (2016). An assessment on performance, combustion and emission behavior of a diesel engine powered by ceria nanoparticle blended emulsified biofuel. *Energy Conversion and Management.* 123, 372–380. DOI: https://doi.org/10.1016/j.enconman.2016.06.062

Canakci, M., Sanli, H. (2008). Biodiesel production from various feedstocks and their effects on the fuel properties. *Journal of Industrial Microbiology and Biotechnology*. 35(5), 431–441, https://doi.org/10.1007/s10295-008-0337-6

Casey, M. V., Schlegel, M. (2010). Estimation of the performance of turbocharger compressors at extremely low pressure ratios. *Proceedings of the Institution of Mechanical Engineers, Part A: Journal of Power and Energy*. 224(2), 239–250. DOI:https://doi.org/10.1243/09576509JPE810

Emőd, I., Füle, M., Tánczos, K., Zöldy, M. (2005). A bioetanol magyarországi bevezetésének műszaki, gazdasági és környezetvédelmi feltételei. *Magyar Tudomány*. 50, 278–286. URL: https://epa.oszk.hu/00600/00691/00015/03.html

Hunicz, J., Matijošius, J., Rimkus, A., Kilikevičius, A., Kordos, P., Mikulski, M. (2020). Efficient hydrotreated vegetable oil combustion under partially premixed conditions with heavy exhaust gas recirculation. *Fuel*. 268, 117350. DOI: https://doi.org/10.1016/j.fuel.2020.117350

Korakianitis, T., Wilson, D. G. (1994). Models for predicting the performance of Brayton-cycle engines. ASME. *Journal of Engineering for Gas Turbines and Power*. 116(2), 381–388. https://doi.org/10.1115/1.2906831

Mikielewicz, D., Kosowski, K., Tucki, K., Piwowarski, M., Stępień, R., Orynycz, O., Włodarski, W. (2019a). Gas turbine cycle with external combustion chamber for prosumer and distributed energy systems. *Energies*. 12(18), 3501. DOI: https://doi.org/10.3390/en12183501

Mikielewicz, D., Kosowski, K., Tucki, K., Piwowarski, M., Stępień, R., Orynycz, O., Włodarski, W. (2019b). Influence of different biofuels on the efficiency of gas turbine cycles for prosumer and distributed energy power plants. *Energies*. 12(16), 3173. DOI: https://doi.org/10.3390/en12163173

Suchocki, T. Kazimierski, P. Lampart, P., Januszewicz, K., Białecki, T., Gawron, B., Janicka, A. (2023). A comparative study of pentanol (C5 alcohol) and kerosene blends in terms of gas turbine engine performance and exhaust gas emission. *Fuel*. 334(2), 126741. DOI: https://doi.org/10.1016/j.fuel.2022.126741

Zöldy, M., Kondor, I. P. (2021). Simulation and injector bench test validation of different nozzle hole effect on pyrolysis oil-diesel oil mixtures. *Energies*. 14(9), 2396. DOI: https://doi.org/10.3390/en14092396

https://doi.org/10.55343/CogSust.20674

Optimal photo overlap for road accident documentation and reconstruction applying UAV imagery

Gábor Vida
https://orcid.org/0000-0002-2682-808X
Department of Automotive Technologies, Faculty of Transportation Engineering and Vehicle Engineering,
Budapest University of Technology and Economics
Budapest, Hungary
vida.gabor@kjk.bme.hu

Nóra Wenszky
https://orcid.org/0000-0002-6490-2391
Centre of Modern Languages, Faculty of Economic and Social Sciences,
Budapest University of Technology and Economics
Budapest, Hungary
wenszky.nora@gtk.bme.hu

Gábor Melegh
Department of Automotive Technologies, Faculty of Transportation Engineering and Vehicle Engineering,
Budapest University of Technology and Economics
Budapest, Hungary
melegh.gabor@kjk.bme.hu

Árpád Török*
https://orcid.org/0000-0002-8573-6345
Department of Automotive Technologies, Faculty of Transportation Engineering and Vehicle Engineering,
Budapest University of Technology and Economics
Budapest, Hungary
torok.arpad@kjk.bme.hu

Abstract

This study investigates the optimal photo overlap for documenting and reconstructing road accident sites using drone imagery. While a general recommendation for drone imagery overlap stands at 60–80%, this research aims to determine the minimum acceptable overlap required to generate a precise 3D point cloud suitable for forensic road accident simulation. A DJI Mavic Air 2 drone captured images at 2-meter intervals over a junction and a connecting road segment from varying altitudes, following the same flight path. The experiment systematically excluded images from the original dataset, processing photo sets taken at 2, 4, 6, 8, and 10-meter intervals. The corresponding point clouds were evaluated for accuracy and fragmentation. Comparisons were made regarding the number of images, the size of image sets and processing times. Additionally, 3D mesh surfaces were generated in the Virtual Crash software, and their quality was assessed. Results revealed that a 50% overlap was adequate for generating satisfactory

https://doi.org/10.55343/CogSust.20674

3D simulation environments, thereby reducing size of the raw data, the point cloud and processing time considerably. This finding is significant for forensic experts seeking efficient methods of road accident scene reconstruction, emphasizing the practicality of lower photo overlap in such scenarios.

Keywords

image overlap, mesh surface, drone, accident documentation, terrain

1. Introduction

In contemporary contexts, unmanned aerial vehicles (UAVs), i.e. drones are applied for diverse tasks across varied environments. The use of drones in surveying and monitoring reduces the need for large teams and heavy machinery, lowering fuel consumption and greenhouse gas emissions, thus contributing to sustainability. Drones enable precise data collection for a number of purposes, ranging from maritime applications (Nomikos et al., 2023), through topographic modelling (Török et al., 2020) and road traffic monitoring (Bisio et al., 2022), to agricultural land monitoring (El Hoummaidi, 2021) and checking on photovoltaic plants (Michail, 2024). In order to ensure that the processed images yield a satisfactory 3D point cloud and a 2D orthomosaic, the acquired images should overlap both along the drone's trajectory (forward overlap) and laterally (side overlap). This overlap facilitates the image processing software in creating a cohesive image through the identification of tie points, i.e., features automatically recognized on two or more adjacent images.

Singh and Fazier (2018) in their meta-analysis of 108 publications on unmanned aircraft system (UAS) imagery warn that there are no standardized practices for image collection and processing. Based on their extensive literature review, they concluded that the observed studies adopted a broad spectrum of overlap values. Specifically, the forward overlap ranged from 60% to 95%, while side overlap spanned from 40% to 90%. Out of the 108 studies analyzed by them, they found none that explicitly stated how terrain characteristics and optimal image overlap are related. Nonetheless, they hypothesize that for flat terrains (i.e. areas with little variation in altitude) higher overlaps are required to ensure that enough tie points are found for 3D point cloud generation.

As Wang et al. (2022) remark, the number of studies with the objective of determining the optimal overlap for missions with UAVs is considerably low. Nevertheless, when confronted with constraints such as limited image processing time or the storage capacity of the computing systems responsible for handling UAV-captured images, an optimal trade-off point must be identified between the quality of the point cloud and the number of images captured in a mission (and hence, the degree of overlap). This means, the minimum overlap of images that yield a satisfactory 3D point cloud and orthomosaic should be determined (cf. Dandoiset al., 2015). The definition of what qualifies as satisfactory highly depends on the type of terrain (Singh & Frazier, 2018), and the objectives of the UAV mission.

One of the applications of UAVs for data collection is road accident scene documentation (Desai et al., 2022), which is in the focus of this research. UAV images at accident sites are typically captured with high overlaps (80–90%) (Pádua et al, 2020; Mat Amin et al., 2020; Zulkifli and Tahar, 2023; Pérez et al., 2024). A road accident site is generally diverse, including vehicles, debris, objects along the road and surrounding buildings or vegetation. Meanwhile, variations in elevation are generally low. Consequently, it is hypothesized that lower forward overlaps between UAV-captured images may produce a satisfactory point cloud (cf. Section 3.1 for a more detailed analysis).

https://doi.org/10.55343/CogSust.20674

This study explores the minimum forward overlap of UAV captured images required to generate point clouds that are still sufficient for the purpose of accident site documentation and reconstruction. In a field test, images were captured with a DJI Mavic Air2 commercial-grade non-RTK UAV in three flights at three altitudes over a public road junction, without the application of ground control points (GCP) (Stott et al., 2020). The images were processed with Agisoft Metashape software in multiple rounds, systematically reducing the the number of images in each round. The resulting point clouds were evaluated for horizontal accuracy and gaps. Additionally, a triangular mesh surface was created for each point cloud using Virtual Crash accident simulation software. The quality of this mesh, which may be applied as a simulation environment, was also checked.

2. Materials and methods

For the test flights, a commercial-grade non-RTK UAV was applied. The DJI Mavic Air 2 drone's major specifications are given in Table 1. The model was chosen due to the simplicity of operation and low cost.

Table 1. Specifications of the DJI Mavic Air 2 drone (DJI, n.d.).

Camera Model	CMOS Sensor [inch]	Resolution	Pixel size [µm]	Focal length [mm]
DJI FC3170	1/2	4000 × 2250	1.77 × 1.77	4.5

The experiments were conducted at the intersection of the lower ranking Road 5207, running on an embankment, and an unpaved roadway in Hungary (47.23518881,19.11902875). The road segments that were recorded are fully paved on both roads (Figure 1). The specific site was selected due to the relatively low traffic, the absence of arboreal obstructions, and the presence of clearly demarcated road delineations. It is also imperative to note that Road 5207 is delineated by lower terrain on both sides.

Figure 1. The site of the experiment

https://doi.org/10.55343/CogSust.20674

In order to be able to check horizontal accuracy of the point clouds, chartreuse markers were placed next to the road, at 2.00 m from each other (Figure 2). The distance between the markers was measured with a laser measure.

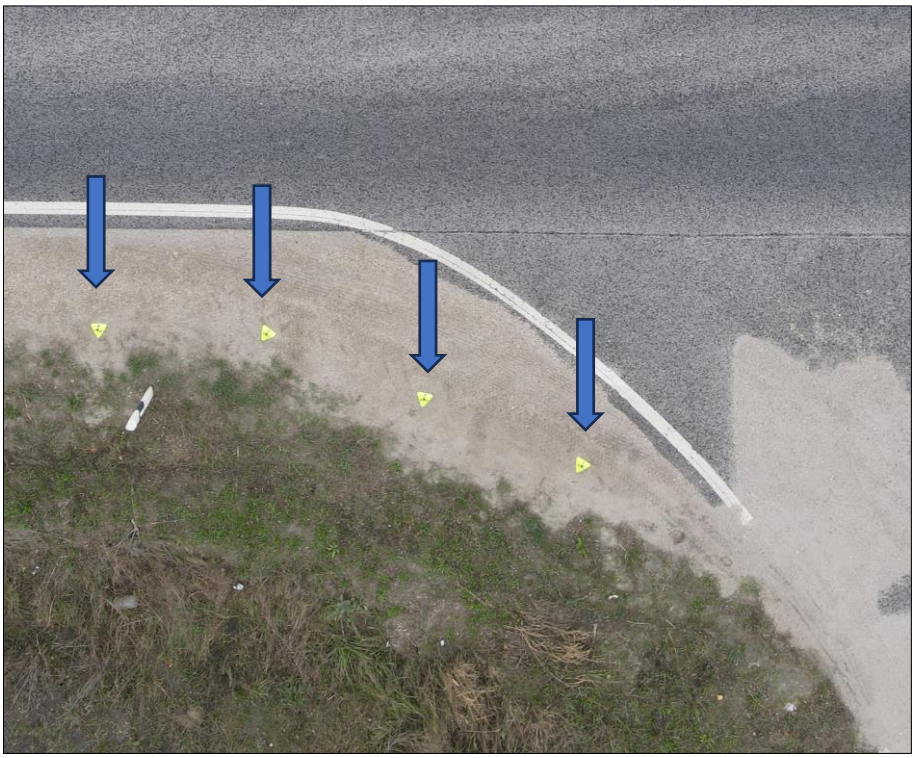

Figure 2. Chartreuse markers along the road section

Three flights were administered, at distinct altitudes: 7.5, 10, and 13 meters, respectively. Apart from the variations in altitude, the routes in the three flights were identical (Figure 3). These missions were pre-programmed with the Litchi software (Litchi, 2023) to ensure that the photographs were taken at identical geographical locations across all altitudes.

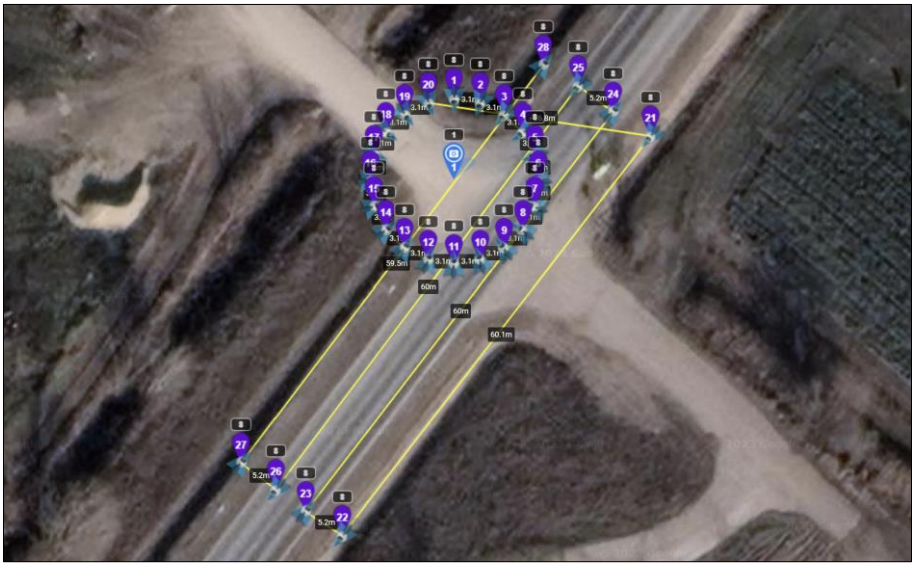

Figure 3. The route of the UAV in the test runs. Yellow lines show the route, and purple circles depict the points where the UAV changed direction. In the circular route, photos were taken at the places marked by purple circles

https://doi.org/10.55343/CogSust.20674

In the initial phase of each mission (Block 1), the UAV followed a circular trajectory centered around an imaginary point of interest (POI) situated at 1 m above ground level at the intersection. The camera was oriented towards this POI, at altitudes of 7.5, 10, and 13 meters, with oblique camera angles (-36°, -49° and -57°, respectively). When the circular path was completed, the UAV proceeded to the second part of the mission. In the second phase (Block 2), the UAV traversed a linear stretch of 60 meters along the paved road, encompassing the junction itself, through four parallel flight lines. While following this grid route, the camera was directed toward the ground with a vertical axis. As a result, oblique images were captured along the circular path over the junction, while nadir images were taken while the drone flew over the extended road segment, following a single grid pattern. The UAV captured images at every 2 meters in all missions (Table 3).

The grid path (Block 2) was combined with a circular path (Block 1) in order to avoid systematic point cloud deformations, such as doming and bowling (Nesbit and Hugenholtz, 2019; Sanz-Ablanedo et al., 2020; James et al., 2020). However, for the purposes of the present study, namely overlap investigations, only images captured during Block 2 were utilized.

Table 2. Main data of the missions

Diameter of circular path [m]	Length of gird paths [m]	Total length of a mission [m]	Image no. Blocks 1+2	Image no. Block 2	Flying time [min:sec]
20	60	341	153	132	8:00

The various sets of images for each mission were processed applying the Python module (Agisoft, 2022) integrated into the Agisoft Metashape 2.0.1. program (Agisoft, 2023) with identical settings. For each mission, an orthomosaic and a 3D point cloud were generated. In the first step, the images captured during Block 2 of each mission were processed. In the next steps, images from each mission were systematically omitted, in a similar manner to Sadeq (2019 and Bupathy et al. (2021). Thus image sets were created that contained all the photos that would have been taken in Block 2 if the UAV had taken photos only at every 4, 6, 8 or 10 meters. For each image set, forward overlap values were calculated (Table 3).

Table 3. Forward overlap for each image set

Distance betw. photos [m]		2	4	6	8	10
		Overlap [%]				
Altitude [m]	7.5	69%	40%	13%	–	–
	10.0	77%	55%	32%	13%	–
	12.0	83%	65%	49%	31%	14%

In the investigation, numerous parameters have been assessed in order to be able to compare the quality of the resulting point clouds. Horizontal accuracy was checked by measuring the distances between the chartreuse markers on each point cloud, and comparing the values to the real-life measurements.

https://doi.org/10.55343/CogSust.20674

Also, the road surface in the point cloud was checked for gaps, i.e. regions devoid of generated points. If a gap with a diameter more than 10 cm on the road surface was identified in the point cloud, the point cloud was regarded as unsatisfactory. Conversely, if occasional gaps below this specified diameter were observed, the point cloud was deemed satisfactory (Figure 4). The limit of 10 cm was determined based on the fact that for accident scene documentation, occasional gaps of such small size are not disturbing. Notably, skid marks and other evidentiary features highlighted by the police typically exceed the aforementioned 10 cm threshold.

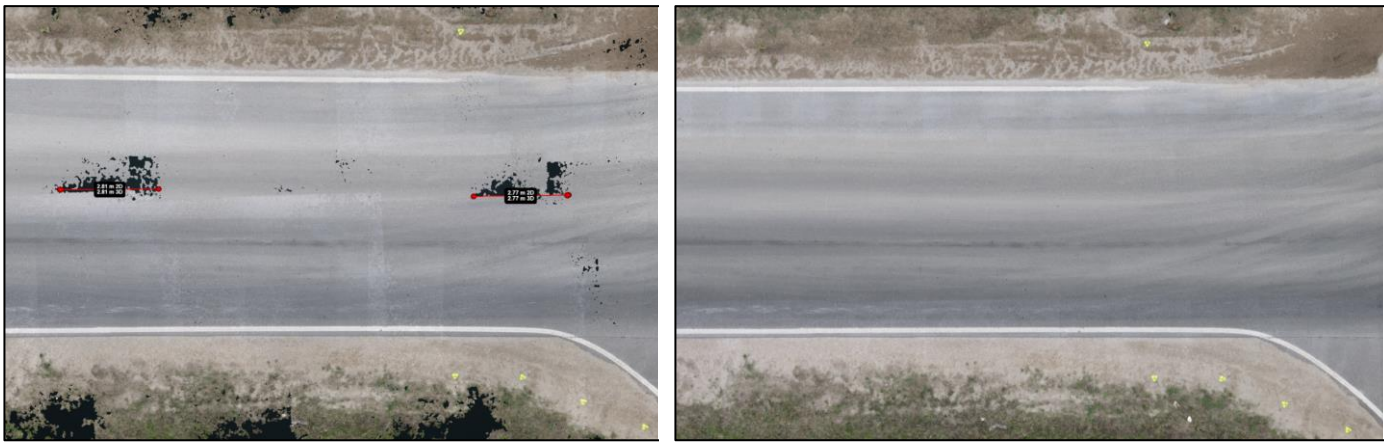

(**a**) (**b**)

Figure 4. Gap detection in a point cloud. **a)** Gaps larger than 10 cm – unsatisfactory. **b)** no gaps – satisfactory

In addition to evaluating point cloud quality, the metadata associated with each mission were analyzed. The parameters considered in this scrutiny included the number of images, the overall size of the image set, processing time, and the resultant size of the point cloud. The data were extracted from the processing report provided by the processing software for each mission.

In order to assess the viability of utilizing the 3D point clouds deemed satisfactory by the above methods for accident simulation purposes, the point clouds were exported to the Virtual Crash 5 simulation software (Virtual Crash, n.d.). Subsequently, a 3D mesh surface was generated for each point cloud, thereby establishing a simulation environment. It was checked whether the arising 3D mesh surface is geometrically correct compared to the actual site. The aim was to test whether the quality of the 3D mesh surface is satisfactory for the reconstruction of a hypothetical accident at the junction recorded. This is why the accident reconstruction software Virtual Crash was applied, although several other software programs may be used to generate such 3D mesh surfaces (such as Maya (Autodesk, n.d.b), 3DS Max (Autodesk, n.d.a), Blender (n.d.). Figure 5 summarizes the steps of the experiment.

https://doi.org/10.55343/CogSust.20674

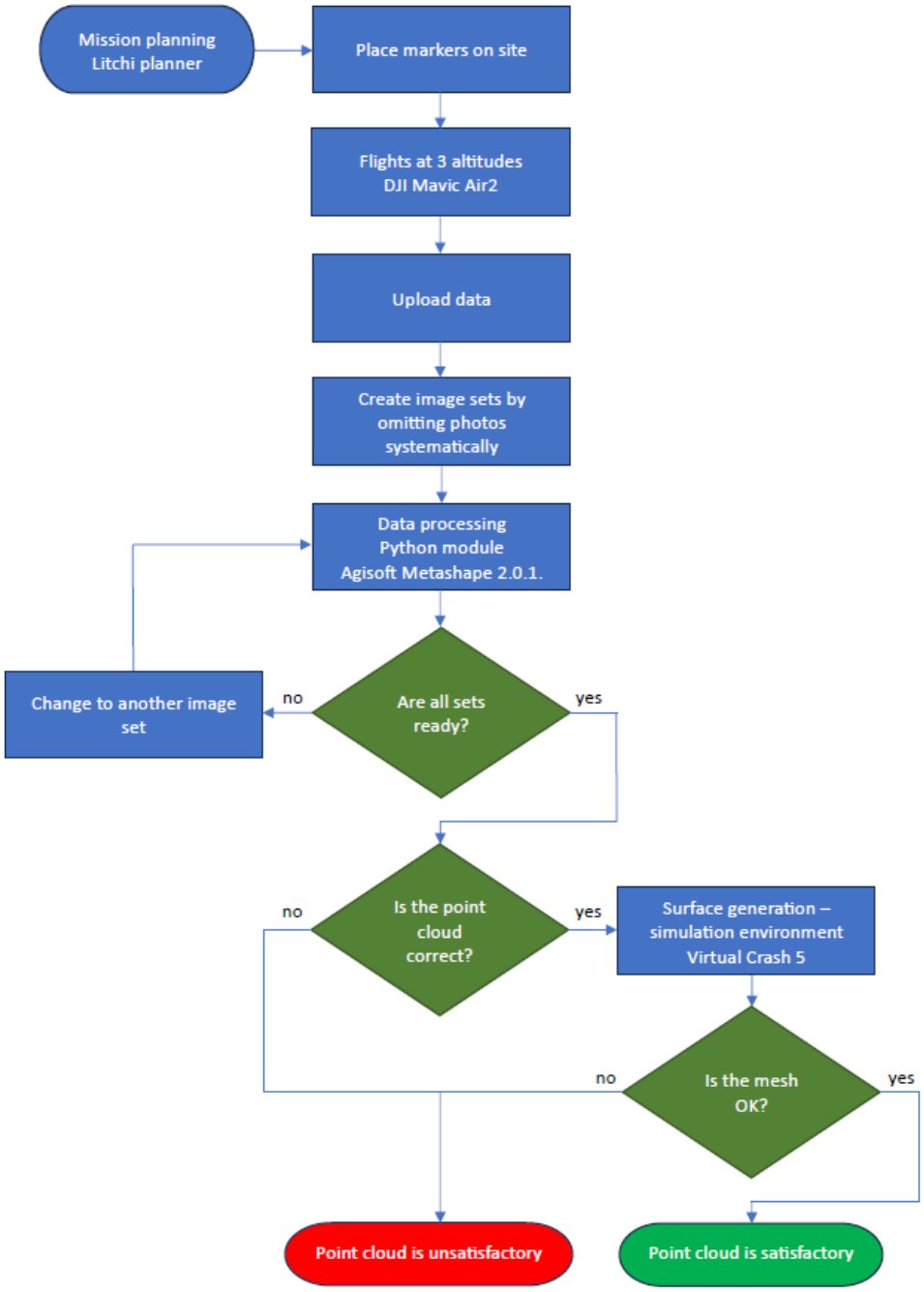

Figure 5. Experimental design.

3. Results

In this section, the results of a comprehensive analysis of the literature are followed by the results of the field tests.

3.1 Analysis of the literature

In the preliminary phase of the present research, several publications using UAV imagery with different purposes have been reviewed, looking for optimal overlap values. Table 4 shows the different forward overlap values reported for varied terrains and mission objectives.

https://doi.org/10.55343/CogSust.20674

Table 4. Overlap values reported in the literature for missions on different types of terrains.[1]

type of area	altitude [m]	forward overlap %	Source
forest	20, 40, 60, 80	60–96, every 4%	Dandois et al. 2015
pine forest	90, 120	**90**, 95	Young et al. 2022
tropical woodland	286, 487	90	Domingo et al. 2019
olive orchard	50, **100**	**95**, 97 58, 64, 69	Torres-Sánchez et al. 2017
desert	140, 160, 180, 200	60–70–**80**	Elhadary et al. 2022
rosemary scrub	60	85	Charton et al. 2021
university campus	60	80–>65 vertical 91–>76 oblique	Sadeq 2019
aubergine field	13, 15	90	Bupathy et al. 2021
wetlands	60, 80, 100, **120**	40, 50, **60**, 70, 80, 90	Flores-de-Santiago et al. 2020
snow depth	**50**, 100	70, **80**, 90	Lee et al. 2021
vertical quarry wall	horizontal: 20	80	Grohmann et al. 2023
sloping cliff face	horizontal: 40–60	70 85	Goncalves et al. 2021
bridges		66.7	Wang et al 2022
archeological site	**15**, 45, 75	60, 70, **80**	Luis-Ruiz et al 2021
road accident	20 25	80	Pádua et al. 2021
	15	–90	Mat Amin et al 2020
	15	80–90	Zulkifli and Tahar 2023

[1] Bold figures show the values that were regarded as the optimal ones in the referenced article.

Based on the values published in the above articles, Figure 6 was generated to show what forward overlap percentages were tested and what optimal overlap values were reported.

https://doi.org/10.55343/CogSust.20674

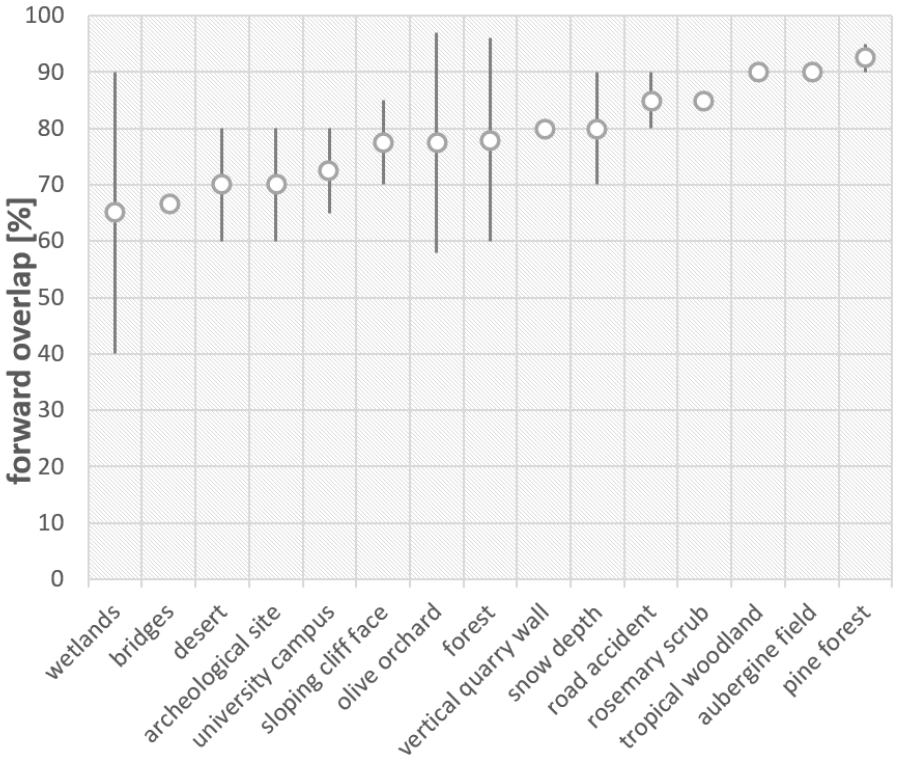

Figure 6. Forward overlap ranges in percentage according to terrain as reported in the literature, based on Table 1. Circles indicate optimal or in the lack of that, average overlap percentage

The question arises whether it is possible to identify characteristics of the terrain that dictate the optimal forward overlap for UAV missions conducted over diverse landscapes. Based on the above data and insight from relevant literature (Singh and Frazier, 2018; Seifert et al., 2019), two factors were taken into consideration. The first factor is diversity, denoting the inhomogeneity of the surface. The second factor is relief, which shows how varied elevations are on a given surface. An examination of the data in Table 4 suggests that both low diversity and substantial differences in elevation necessitate higher overlaps, as in the case of forests, where tree heights differ considerably. However, when diversity is high and elevation differences are low, as exemplified by wetlands, a reduced UAV image overlap may still yield satisfactory results (Figure 7). It is crucial to acknowledge that values in Figure 7 are approximations and serve as indicative benchmarks.

https://doi.org/10.55343/CogSust.20674

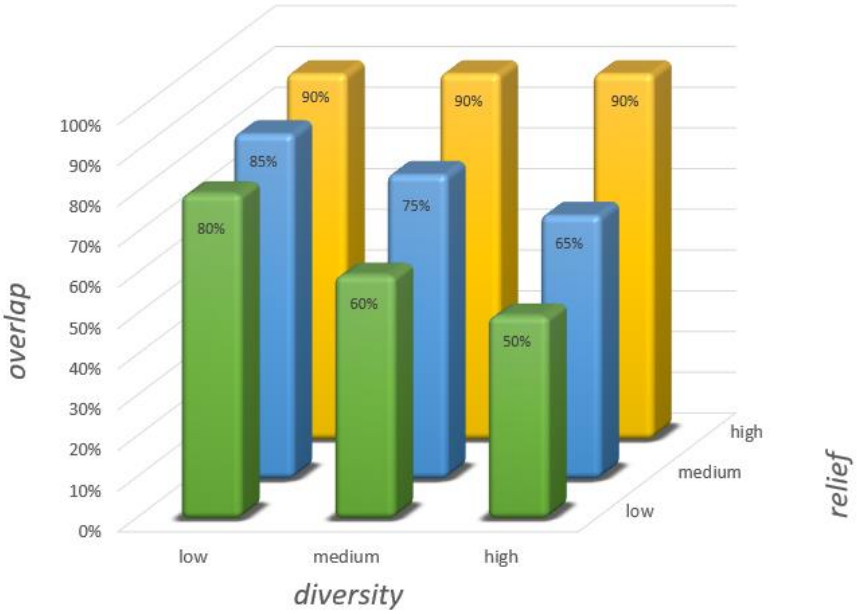

Figure 7. Forward overlap required for different terrains. The values are approximate values based on the data from Table 1

3.2 Experiment

The experiment comprised 3 missions at the altitudes of 7.5, 10 and 12 meters, with images being captured at every 2 meters. The original datasets underwent a process in which images were omitted systematically, until no forward overlap persisted between consecutive images. As a result of this procedure, a total of 12 datasets were examined: 3 sets for the 7.5 m altitude, 4 sets for the 10 m altitude, and 5 sets for the 12 m altitude (see Table 3 above). The results of the quality checks are elaborated below.

3.1. Accuracy

The accuracy of the point clouds was checked in two ways.

3.1.1. Horizontal accuracy

The horizontal accuracy of the point clouds was tested by measuring the distances on each point cloud between the chartreuse markers (Figure 8). Results are given in Table 5. The values show that the horizontal accuracy of the point clouds varies. However, from this dataset, no clear relationships can be found between overlap percentages, flight altitude and accuracy. In order to explore such relationships, further experiments must be conducted. However, as the differences between point cloud measurement results and on site measurement data are within the 0–5 cm range, the accuracy of each point cloud is satisfactory for road accident simulation purposes.

https://doi.org/10.55343/CogSust.20674

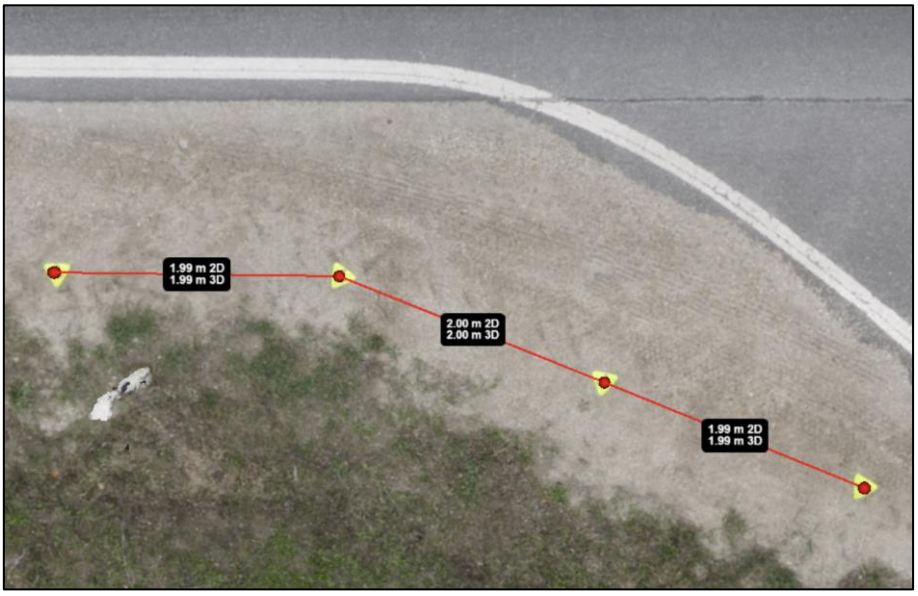

Figure 8. Measuring the distance between the chartreuse markers in the point cloud.

Table 5. Distances between the chartreuse markers measured on the point clouds. In reality, the distance between the markers was 2.00 m, measured by a laser measure.

Distance betw. photos [m]		**2**	**4**	**6**	**8**	**10**
		Measured values in point cloud [m]				
Altitude [m]	**7.5**	2.00	2.04	2.03	–	–
		2.00	2.04	2.01		
		2.01	2.04	2.01		
	10.0	2.00	1.95	2.03	2.01	–
		2.01	1.94	2.04	2.01	
		2.00	1.95	2.03	2.00	
	12.0	1.99	1.95	2.04	2.02	2.00
		2.00	1.94	2.04	2.05	2.01
		1.99	1.95	2.03	2.04	2.03

3.1.2. Gaps

Regarding gaps in the point clouds, those with gap sizes not exceeding 10 cm in diameter *(d)* were regarded as satisfactory (Table 6). In subsequent tables, those sets that were deemed satisfactory from this respect appear with a gray background colour.

Table 6. Gaps in point clouds – bold faced sets did not contain large ($d > 10$ cm) gaps.

Distance betw. photos [m]		**2**	**4**	**6**	**8**	**10**
		Overlap [%]				
Altitude [m]	**7.5**	**69%**	40%	13%	–	–
	10.0	**77%**	**55%**	32%	13%	–
	12.0	**83%**	**65%**	**49%**	31%	14%

https://doi.org/10.55343/CogSust.20674

3.2. Metadata

Each of the 12 datasets was processed with Agisoft Metashape 2.0.1 software (2023) using the same settings. Tables 7 and 8 show the sizes of the image sets and of the point clouds, respectively. This is an important metric, as storing large datasets requires large storage capacities. Additionally, the larger a data set is, the longer the processing time (Table 9).

Table 7. Number of images and size of image sets.

Distance betw. photos [m]		**2**	**4**	**6**	**8**	**10**
		No. of images – size of image set				
Altitude [m]	**7.5**	133 – 601 MB	67 – 303 MB	44 – 199 MB	–	–
	10.0	132 – 627 MB	66 – 314 MB	44 – 210 MB	33 – 156 MB	–
	12.0	93 – 487 MB	47 – 246 MB	31 – 163 MB	24 – 126 MB	19 – 100 MB

Table 8. The size of the generated point clouds.

Distance betw. photos [m]		**2**	**4**	**6**	**8**	**10**
		Size of the point cloud [px]				
Altitude [m]	**7.5**	57 814 351	37 011 874	26 898 031	–	–
	10.0	40 653 230	28 016 162	20 309 524	15 442 673	–
	12.0	24 663 121	19 154 362	15 254 324	12 851 936	10 837 981

Table 9. Processing time per image set.

Distance betw. photos [m]		**2**	**4**	**6**	**8**	**10**
		Processing time				
Altitude [m]	**7.5**	7m 39s	4m 47s	3m 39s	–	–
	10.0	6m 52s	4m 1s	2m 54s	2m 40s	–
	12.0	4m 43s	2m 41s	2m 1s	1m 40s	1m 30s

3.3. Mesh as a simulation environment

Vehicle motion simulation software generates the 3D environment from a point cloud or mesh model. In the present case, Virtual Crash 5 vehicle motion simulation software was utilized to evaluate the usability of point clouds. After importing a point cloud into the program, the program generates a 3D mesh surface from it. The arising mesh surface is then used for performing the simulation

https://doi.org/10.55343/CogSust.20674

calculations. During the mesh surface generation process, the mesh surface design can be influenced by setting a number of parameters. However, in all cases a point cloud of sufficient quality is a prerequisite for the creation of a suitable mesh model.

All the mesh surfaces generated from the point clouds that had been categorized as “satisfactory” based on their accuracy and the presence or absence of gaps (Table 6) resulted in a suitable mesh. Figure 9 shows an example for a mesh surface generated form a suitable point cloud. Vehicle movement can be accurately modeled on the mesh, including the vehicle’s descent into the ditch along the roadway.

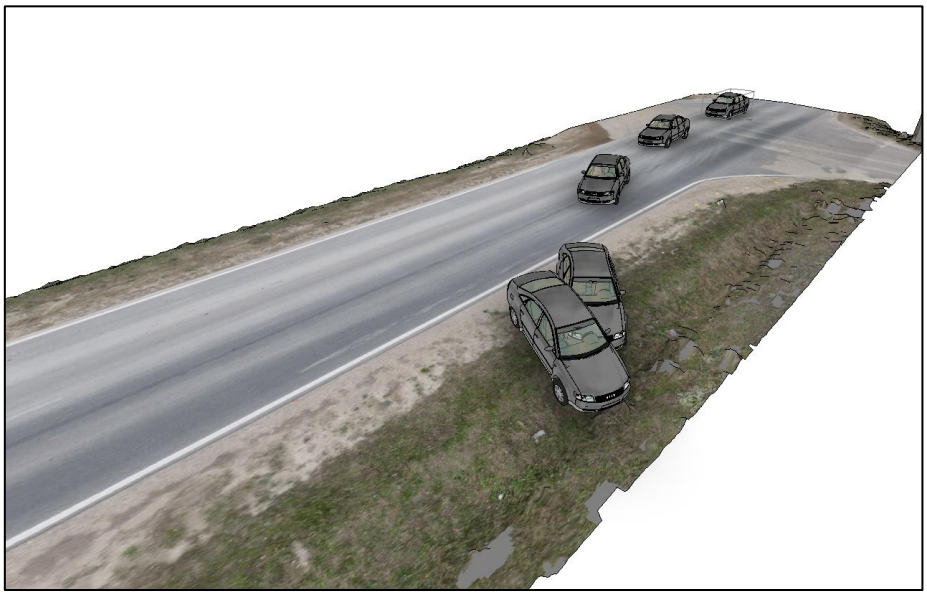

Figure 9. Mesh surface generated from the point cloud with Virtual Crash 5 software. The simulation of a roadway departure accident.

4. Discussion

The analysis of the literature confirmed Singh and Frazier (2018)’s finding that a high variability is attested in the photo overlap values used across varied UAV applications. It was proposed that the necessary overlap value may be determined by examining the vertical fragmentation (relief) and diversity of the terrain to be surveyed. Based on these characteristics of the terrain, approximate forward overlap values were suggested (Figure 9). In applications where processing time, the size of the image set and the result of the point cloud are of primary importance, the minimal overlap ratio should be used at which the quality of the resulting point cloud is still satisfactory.

Accident scene documentation is an application of UAVs where processing time and data file size should be minimized. Generally, a forward overlap ratio of 80–90% is proposed in the literature (Pádua et al., 2020; Mat Amin, 2020; Zulkifli and Tahar, 2023; Pérez, 2024) for road accident scene documentation. In contrast, our analysis has shown that for an average accident scene (straight roadway section, roadside ditch with vegetation), the point cloud resulting from processing images of at least 50% forward overlap is of sufficient quality for further processing. This also means that the number of images taken during the survey and the storage space required for archiving can be reduced by about a third. The time required to process the images can be reduced by about 50%, and the size of the resulting point cloud by about 40%. Our tests have also shown that a point cloud with about 50% overlap provides a good input for a vehicle motion simulation program to generate the 3D environment for vehicle motion calculations.

https://doi.org/10.55343/CogSust.20674

5. Conclusion

This study examined the optimal forward overlap ratio for images captured by drones during the documentation of road accident sites. Tests conducted at a road junction in Hungary suggest that a 50% forward overlap between images yields a sufficient point cloud. This relatively low overlap helps minimize the number of images captured, thereby accelerating the documentation process. A faster yet still effective accident documentation procedure shortens road closure time, resulting in reduced congestion and a more sustainable data collection process.

Author contributions: Conceptualization, GV, GM, NW; methodology, GV, GM, NW; software, GV; validation, GM, ÁT; formal analysis, GV,GM; investigation, GV, NW; resources, GV, NW; data curation, GV; writing—original draft preparation, NW; writing—review and editing, GV, ÁT; visualization, GV; supervision, GM, ÁT; project administration, GV; funding acquisition, GV. All authors have read and agreed to the published version of the manuscript.

Funding: This research was funded by NKFIH, grant number 2021-1.1.4-GYORSÍTÓSÁV-2022-00023 "Proper documentation and evaluation of an accident scene using high-performance image capture technology. Development and market introduction of an intelligent Geographic Information System (GIS) [Baleseti helyszín megfelelő dokumentálása és kiértékelése nagyteljesítményű képi adatrögzítő technológia alkalmazásával. Intelligens Térinformatikai Rendszer (ITR) kifejlesztése, piaci bevezetése]."

Conflicts of Interest: The authors declare no conflict of interest. The funders had no role in the design of the study; in the collection, analyses, or interpretation of data; in the writing of the manuscript; or in the decision to publish the results.

References

Agisoft. (2022). *Metashape Python Reference*. Release 2.0.0. URL: https://www.agisoft.com/pdf/metashape_python_api_2_0_0.pdf

Agisoft. (2023). *Agisoft Metashape 2.0.1*. URL: https://www.agisoft.com/features/professional-edition/

Autodesk. (n.d.a). *3DS Max*. URL: https://www.autodesk.com/products/3ds-max/overview?term=1-YEAR&tab=subscription

Autodesk. (n.d.b). *Autodesk Maya software*. URL: https://www.autodesk.com/products/maya/overview?term=1-YEAR&tab=subscription

Bisio, I., Garibotto, C., Haleem, H., Lavagetto, F., Sciarrone, A. (2022). A Systematic Review of Drone Based Road Traffic Monitoring System. *IEEE Access*. 10, 101537-101555. DOI: https://doi.org/10.1109/ACCESS.2022.3207282

Bupathy, P., Sivanpillai, R., Sajithvariyar, V., Sowmya, V. (2021). Optimizing low-cost UAV aerial image mosaicing for crop growth monitoring. *The International Archives of the Photogrammetry, Remote Sensing and Spatial Information Sciences*. XLIV-M-3-2021. URL: https://isprs-archives.copernicus.org/articles/XLIV-M-3-2021/7/2021/isprs-archives-XLIV-M-3-2021-7-2021.pdf

Castro, J., Morales-Rueda, F., Alcaraz-Segura, D., Tabik, S. (2023). Forest restoration is more than firing seeds from a drone. *Restoration Ecology*. 31(1), e13736. DOI: https://doi.org/10.1111/rec.13736

Charton, K., Sclater, V., Menges, E. (2021). Mapping spatially explicit vegetation gaps in Florida rosemary scrub using unmanned aerial vehicles. *Ecosphere*. 12(4). DOI: https://doi.org/10.1002/ecs2.3470

Virtual Crash (n.d.). *Virtual Crash 5 Accident Reconstruction Software*. URL: https://www.vcrashusa.com/vc5

Dandois, J., Olano, M., Ellis, E. (2015). Optimal altitude, overlap, and weather conditions for computer vision UAV estimates of forest structure. *Remote Sensing*. 7(10), 13895-13920. DOI: https://doi.org/10.3390/rs71013895

Desai, J., Mathew, J. K., Zhang, Y., Hainje, R., Horton, D., Hasheminasab, S. M., Habib, A., Bullock, D. M. (2022). Assessment of Indiana Unmanned Aerial System Crash Scene Mapping Program. *Drones*. 6(259), 1-15. DOI: https://doi.org/10.3390/drones6090259

DJI. (n.d.). *Mavic Air 2*. URL: https://www.dji.com/hu/mavic-air-2/specs

Domingo, D., Ørka, H., Næsset, E., Kachamba, D., Gobakken, T. (2019). Effects of UAV Image Resolution, Camera Type, and Image Overlap on Accuracy of Biomass Predictions in a Tropical Woodland. *Remote Sensing*. 11(8), 948. DOI: https://doi.org/10.3390/rs11080948

https://doi.org/10.55343/CogSust.20674

El Hummaidi, L. L. (2021). Using unmanned aerial systems and deep learning for agriculture mapping. *Heliyon*. 7, e08154. DOI: https://doi.org/10.1016/j.heliyon.2021.e08154

Elhadary, A., Rabah, M., Ghanim, E., Mohie, R., Taha, A. (2022). The influence of flight height and overlap on UAV imagery over featureless surfaces and constructing formulas predicting the geometrical accuracy. *NRIAG Journal of Astronomy and Geophysics*. 11(1), 210–223. DOI: https://doi.org/10.1080/20909977.2022.2057148

Flores-de-Santiago, F., Valderrama-Landeros, L., Rodríguez-Sobreyra, R. (2020). Assessing the effect of flight altitude and overlap on orthoimage generation for UAV estimates of coastal wetlands. *Journal of Coastal Conservation*. 24, 35. DOI: https://doi.org/10.1007/s11852-020-00753-9

Blender (n.d.). *Blender*. URL: https://www.blender.org/download/

Gonçalves, G., Gonçalves, D., Gómez-Gutiérrez, Á., Andriolo, U., Pérez-Alvárez, J. (2021). 3D reconstruction of coastal cliffs from fixed-wing and multi-rotor uas: impact of SfM-MVS processing parameters, image redundancy and acquisition geometry. *Remote Sensing*. 13(6), 1222. DOI: https://doi.org/10.3390/rs13061222

Grohmann, C. H., Viana, C. D., Garcia, G. P., Albuquerque, R. W. (2023). Remotely piloted aircraft-based automated vertical surface survey. *MethodsX*. 10. DOI: https://doi.org/10.1016/j.mex.2022.101982

James, M. R., Antoniazza, G., Robson, S., Lane, S. N. (2020). Mitigating systematic error in topographic models for geomorphic change detection: accuracy, precision and considerations beyond off-nadir imagery. *Earth Surface Processes and Landforms*. 45, 2251–2271. DOI: https://doi.org/10.1002/esp.4878

Lee, S., Park, J., Choi, E., Kim, D. (2021). Factors Influencing the Accuracy of Shallow Snow Depth Measured Using UAV-Based Photogrammetry. *Remote Sensing*. 13(4), 828. DOI: https://doi.org/10.3390/rs13040828

Litchi. (2023). *Litchi for DJI Drones*. URL: https://flylitchi.com/

Liu, X., Lian, X., Yang, W., Wang, F., Han, Y., Zhang, Y. (2022). Accuracy Assessment of a UAV Direct Georeferencing Method and Impact of the Configuration of Ground Control Points. *Drones*. 6(2), 30. DOI: https://doi.org/10.3390/drones6020030

Luis-Ruiz, J., Sedano-Cibrián, J., Pereda-García, R., Pérez-Álvarez, R., Malagón-Picón, B. (2021). Optimization of Photogrammetric Flights with UAVs for the Metric Virtualization of Archaeological Sites. Application to Juliobriga (Cantabria, Spain). *Applied Sciences*. 11(3), 1204. DOI: https://doi.org/10.3390/app11031204

Mat Amin, A., Abdullah, A., Abdul Mukti, S., Moht Zaidi, M., Tahar, K. (2020). Reconstruction of 3D accident scene from multirotor UAV platform. *The International Archives of the Photogrammetry Remote Sensing and Spatial Information Sciences*. XLIII-B2-2020, pp. 451–458. DOI: https://doi.org/10.5194/isprs-archives-XLIII-B2-2020-451-2020

Michail, A. L. (2024). A comprehensive review of unmanned aerial vehicle-based approaches to support photovoltaic plant diagnosis. *Heliyon*. 10, e23983. DOI: https://doi.org/10.1016/j.heliyon.2024.e23983

Nomikos, N., Gkonis, P. K, Bithas, P. S., Trakadas, P. (2023). A Survey on UAV-aided maritime communications: Deployment considerations, applications, and future challenges. *IEEE Open Journal of the Communications Society*. 4, 56–78. DOI: https://doi.org/10.1109/OJCOMS.2022.3225590

Nesbit, P. R., Hugenholtz, C. H. (2019). Enhancing UAV–SfM 3D model accuracy in high-relief landscapes by incorporating oblique images. *Remote Sensing*. 11(3), 239. DOI: https://doi.org/10.3390/rs11030239

Pádua, L., Sousa, J., Vanko, J., Hruška, J., Adão, T., Peres, E., Soua, A., Sousa, J. J. (2020). Digital reconstitution of road traffic accidents: A flexible methodology relying on UAV surveying and complementary strategies to support multiple scenarios. *International Journal of Environmental Research and Public Health*. 17(6). DOI: https://doi.org/10.3390/ijerph17061868

Pérez, J. A., Gonçalves, G. R., Morillo Barragán, J. R., Fuentes Ortega, P., Caracol Palomo, A. A. (2024). Low-cost tools for virtual reconstruction of traffic. *Heliyon*. 10, e29709. DOI: https://doi.org/10.1016/j.heliyon.2024.e29709

Sadeq, H. A. (2019). Accuracy assessment using different UAV image overlaps. *Journal of Unmanned Vehicle Systems*. 7(3), 175–193. DOI: https://doi.org/10.1139/juvs-2018-0014

Sanz-Ablanedo, E., Chandler, J. H., Ballestros-Pérez, P., Rodriguez-Pérez, J. R. (2020). Reducing systematic dome errors in digital elevation models through better UAV flight design. *Earth Surface Processes and Landforms*. 45(9), 2143-2147. DOI: https://doi.org/10.1002/ESP.4871

https://doi.org/10.55343/CogSust.20674

Seifert, E., Seifert, S., Vogt, H., Drew, D., van Aardt, J., Kunneke, A., Seifert, T. (2019). Influence of drone altitude, image overlap, and optical sensor resolution on multi-view reconstruction of forest images. *Remote Sensing*. 11(10), 1252. DOI: https://doi.org/10.3390/rs11101252

Singh, K. K., Frazier, A. E. (2018). A meta-analysis and review of unmanned aircraft system (UAS) imagery for terrestrial applications. *International Journal of Remote Sensing*. 39(15–16), 5078-5098. DOI: https://doi.org/10.1080/01431161.2017.1420941

Stott, E., Williams, R. D., Hoey, T. B. (2020). Ground control point distribution for accurate kilometre-scale topographic mapping using an RTK-GNSS unmanned aerial vehicle and SfM photogrammetry. *Drones*. 4(3), 55. DOI: https://doi.org/10.3390/drones4030055

Torres-Sánchez, J., López-Granados, F., Bprra-Serrano, I., Peña. (2018). Assessing UAV-collected image overlap influence. *Precision Agriculture*. 19, 115–133. DOI: https://doi.org/10.1007/s11119-017-9502-0

Török, Á., Bögöly, G., Somogyi, Á., Lovas, T. (2020). Application of UAV in topographic modelling and structural geological mapping of quarries and their surroundings – delineation of fault-bordered raw material reserves. *Sensors*. 20. DOI: https://doi.org/10.3390/s20020489

Wang, F., Zou, Y., Del Rey Castillo, E., Lim, J. P. (2022). Optimal UAV image overlap for photogrammetric 3D reconstruction of bridges. *IOP Conference Series: Earth and Environmental Science.* 1101, 022052. DOI: https://doi.org/10.1088/1755-1315/1101/2/022052

Young, D. J., Koontz, M., Weeks, J. (2022). Optimizing aerial imagery collection and processing parameters for drone-based individual tree mapping in structurally complex conifer forests. *Methods in Ecology and Evolution*. 13(7), 1447–1463. DOI: https://doi.org/10.1111/2041-210X.13860

Zulkifli, M. H., Tahar, K. N. (2023). The Influence of UAV Altitudes and Flight Techniques in 3D Reconstruction Mapping. *Drones*. 7(4), 227. DOI: https://doi.org/10.3390/drones7040227